

**Application of femtosecond lasers
for subcellular nanosurgery**

A thesis presented

by

Iva Maxwell

to

The Division of Engineering and Applied Sciences

in partial fulfillment of the requirements

for the degree of

Doctor of Philosophy

in the subject of

Applied Physics

Harvard University

Cambridge, Massachusetts

December 2006

©2006 by Iva Maxwell

All rights reserved.

Application of femtosecond lasers for subcellular nanosurgery

Eric Mazur

Iva Z. Maxwell

ABSTRACT

This dissertation offers a study of femtosecond laser disruption in single cells. Cells and tissues do not ordinarily absorb light in the near-IR wavelength range of femtosecond lasers. However, the peak intensity of a femtosecond laser pulse is very high and material disruption is possible through nonlinear absorption and plasma generation. Because the pulse duration is very short, it is possible to reach the intensity of optical breakdown at only nanojoules of energy per pulse. The low energy deposition and the high spatial localization of the nonlinear absorption, make femtosecond laser pulses an ideal tool for minimally disruptive subcellular nanosurgery.

We show definitively that there can be bulk ablation within a single cell by studying the disrupted region under a transmission electron microscope. The width of the ablated area can be as small as 250 nm in diameter at energies near the ablation threshold. We also studied the effect of the laser repetition rate on the subcellular disruption threshold. We compared the pulse energies for kHz and MHz pulse trains, and found that in the MHz regime heat accumulation in the focal volume needs to be accounted for. For this repetition rate the minimum pulse energy necessary for disruption depends on the laser irradiation time.

We used femtosecond laser nanosurgery to probe tension in actin stress fibers in living endothelial cells. By severing an individual stress fiber and visualizing its retraction, we showed that actin carries prestress in adherent, non-contractile cells. By plating the cells on softer, more compliant substrates, we measured the deflection of the substrate and extrapolated the force contribution of a stress filament on total amount of force exerted by the cell.

Table of Contents

<i>Abstract</i>	<i>iii</i>
<i>Table of Contents</i>	<i>iv</i>
<i>List of Figures</i>	<i>vi</i>
<i>List of Tables</i>	<i>xi</i>
<i>Acknowledgements</i>	<i>xii</i>
<i>Citations to Published Work</i>	<i>xv</i>
1 Introduction	1
2 Femtosecond laser disruption of transparent materials	5
2.1 Optical properties of tissues	6
2.2 Laser-tissue surgery mechanisms	8
2.3 Plasma-induced material disruption	11
2.3.1 Optical breakdown in transparent materials	11
2.3.2 Plasma generation and material disruption	13
2.4 Photodisruption	15
2.5 Bubble formation in water	16
2.6 Laser repetition rate dependence on photodisruption	17
2.7 Summary	19
3 Applications of femtosecond lasers in biology	20
3.1 Nonlinear imaging	20
3.1.1 Two-photon excitation spectra	23
3.1.2 Intrinsic autofluorescence excitation	24
3.1.3 Second- and third-harmonic generation imaging	25
3.1.4 Photobleaching and photodamage in MPM	28
3.1.5 Summary	30
3.2 Femtosecond laser cell and tissue disruption	30
3.2.1 Plasma-induced ablation for subcellular nanosurgery	30

3.2.2	Photodisruption of tissues	38
3.2.3	Conclusion	43
4	Experimental Setup	44
4.1	Femtosecond laser systems	44
4.2	Fluorescence microscope	46
4.3	Custom-built multiphoton microscope	53
4.4	Summary	59
5	Subcellular dissection confirmed by TEM	60
5.1	Introduction	60
5.2	Experimental methods	61
5.3	Results	63
5.4	Conclusion	67
6	Dependence of the subcellular disruption threshold on the laser repetition rate	69
6.1	kHz laser repetition rate	70
6.2	MHz laser repetition rate	71
6.3	Variable repetition rate	77
6.4	Outlook	81
6.5	Summary	82
7	Probing cell mechanics: disruption of stress fibers in live cells	85
7.1	Introduction	85
7.2	Materials and methods	89
7.2.1	Cell culture	89
7.2.2	Laser nanosurgery and photobleaching	90
7.2.3	Traction force microscopy	91
7.3	Results	92
7.3.1	Disruption of individual actin stress fibers in living cells	92
7.3.2	Mechanical properties of stress fibers in living cells	98
7.3.3	Tensional prestress in fiber bundles	100
7.3.4	Contribution of single stress fiber to cell-substrate traction	102
7.4	Discussion	107
8	Conclusion and Outlook	115
	References	120

List of Figures

2.1	Absorption spectra of the major absorbers found in tissue. There are no efficient one-photon absorbers in cells and tissues in the near-IR spectrum, making them nearly transparent in this wavelength range. [1]	6
2.2	Map of laser-tissue interactions. The circles give a rough estimate of the associated laser parameters. Modified from [2].	8
2.3	Schematic diagram of optical breakdown. First, a free electron is promoted through (MPI); then it linearly absorbs photons until its energy reaches twice that of the binding potential and it impact ionizes an bound electron. Adapted from [3].	12
2.4	Damage produced under the same focusing conditions in fused silica by a) 100 fs pulses with 2 μm spacing and b) 200 ps with 10 μm spacing [4]. . . .	14
2.5	Threshold for material disruption as function of NA and pulse energy [5]. . .	15
2.6	Threshold for material disruption as function of NA and pulse energy. . . .	16
2.7	Damage in Corning 0211 glass at a) 1 kHz [3] and b) 25 MHz laser repetition rate [6].	18
3.1	Linear (from the left) and two-photon (from the right) excitation of fluorescein [7].	21
3.2	Two photon action cross-sections (absorption cross section multiplied by the fluorescence quantum yield). a) Two-photon action spectrum of Rhodamine B (black) compared to the one-photon absorption spectrum (red). b) Two-photon action spectra of five common fluorescent proteins: eGFP (green), CFP (cyan), YFP (yellow), Discosoma Red (dsRed; red) and wild type GFP (wtGFP; black). [7]	24

3.3	Two-photon action cross sections (absorption cross section multiplied by the fluorescence quantum yield) and emission spectra from a basis set of biological molecules. (a) Action cross sections of six molecules that contribute much of the intracellular two-photon excitation intrinsic fluorescence. All compounds were measured in buffered (pH 7.2) saline solution, except retinol and cholecalciferol (vit D), which were measured in EtOH. Riboflavin, cholecalciferol, and NADH were measured at 100 μ M; retinol, folic acid, phyloquinone, pyridoxine, and nicotinamide were measured at 500 μ M. (b) Emission spectra of the compounds shown in a) (measured in the same solvents). [8]	25
3.4	SHG image from RAFT collagen at depths of 0, 50, 100, 150, 200 and 230 μ m for λ_{ex} = 800 nm (a-f) (Bar = 5 μ m). The corresponding spectra and plot of SHG signal intensity vs. depth are show in (g). [9]	27
3.5	Femtosecond laser nanodissection of human chromosomes. a) slices through a chromosome are created by scanning the laser beam in parallel lines across [1] and b) holes are drilled in the chromosome by fixing the laser on a spot [10]; c) Targeted cell transfection through laser irradiation of the cell membrane. eGFP is expressed in the irradiated cells. Scale bar, 25 μ m. [11]	32
3.6	Ablation of a single mitochondrion in a living endothelial cell. (a) Fluorescence microscope image showing multiple mitochondria before femtosecond laser irradiation. Target mitochondrion (marked by arrow) (b) before and (c) after laser ablation with 2-nJ pulses [12]	33
3.7	Ablation of a mitochondrion in a live cell without compromising cell viability. Fluorescence microscope images of a live cell containing EYFP-labeled mitochondria in a cultured medium containing ethidium bromide (a) before femtosecond laser irradiation, (b) after ablation of a single mitochondrion within its cytoplasm (target 1 in diagram at bottom left), and (c) after irradiation of the apical cell membrane (target 2). An increase in nuclear ethidium bromide staining is only observed after irradiation of the apical membrane. [12]	34
3.8	Confocal microscope image of a GFP-labeled AFD neuron a day after severing one of the dendrites [13]	36
3.9	Femtosecond laser axotomy in <i>Caenorhabditis elegans</i> worms using 100 pulses of low energy (40 nJ) and short duration (200 fs) and a repetition rate of 1 kHz. (a) Fluorescence images of axons labelled with green fluorescent protein before, immediately after, and in the hours following axotomy. Arrow indicates point of severance. Scale bar, 5 μ m. (b) Statistics of axon growth 24 h after axotomy, based on fluorescence images (n=52 axons). (c) Time-course analysis of backward motion of worms following axotomy. Seventeen worms were scored blindly at different time points (for criteria, see supplementary information). Improvement in backward motion was graded as four levels from shrinker behaviour (dark red) up to wild type behavior (yellow) in the hours following axotomy. [14]	37
3.10	Optical cutting, optical sectioning and volumetric reconstruction of labeled vasculature in mouse neortical tissue [15]	39

3.11	(b,c) Maps of fluorescein-dextran-labeled vasculature of rat parietal cortex. Inset in (b) shows latex-filled surface arteries and arterioles in rat cortex, and the white rectangle indicated the approximate location of the craniotomy. The images in (b) are maximal projections along the optical axis of near-surface vasculature. Scale bars: (b) 500 μm (inset 5 mm) (c) 100 μm . (d) schematic of the three different vascular lesions that are produced by varying the energy and number of laser pulses. At high energies, photodisruption produces hemorrhages, in which the target is ruptured, blood invades the brain tissue, and a mass of RBCs form a hemorrhagic core. At low energies the target vessel remains intact, but transiently leaks blood plasma and RBCs forming and extravasation. Multiples pulses at low energy leads to thrombosis that can completely occlude the target vessel, forming an intravascular clot. Scale bar, 50 μm . Adapted from [16]	41
3.12	Scanning electron micrograph of a corneal flap and an intrastromal lenticule cut out with femtosecond laser pulses. [17]	42
4.1	A schematic diagram of the stages of an amplified femtosecond laser system with corresponding repetition rate, pulse duration and pulse energy.	45
4.2	This is a schematic setup of the custom built inverted fluorescence microscope	47
4.3	Transmission plots for FITC, TRITC and DAPI filter sets from www.chroma.com (blue:exciter, green:dichroic, red:emitter), and a typical laser dielectric mirror from www.cvilaser.com .	49
4.4	Fluorescence images of Alexa 488 labeled actin in an endothelial cell a) before and b) after irradiation along 5 parallel lines with corresponding per pulse energies. c) shows a cell before and d) after irradiation with a 60 nJ pulses and the extent of the damage due to a cavitation bubble.	50
4.5	Fluorescence images of live endothelial cells transfected with YFP actin: a) before laser irradiation, b) after a single filament was cut, c) a second filament was cut, d) 10 minutes after laser nanosurgery.	52
4.6	Schematic of a combined multiphoton imaging and surgery setup.	54
4.7	Two-photon image taken of Alexa 488 labeled actin in a fixed endothelial cell.	55
4.8	Two-photon image taken of DAPI labeled nucleus in a fixed cell a) before and b) after laser surgery.	55
4.9	Two-photon excitation of autofluorescence in a leaf.	57
4.10	Two-photon image taken of DAPI labeled nucleus in a fixed cell.	58
5.1	(a) Cuts through fluorescently-labeled actin fibers in a fixed endothelial cell obtained by irradiation with femtosecond laser pulses of energies between 1.8 nJ and 4.4 nJ. (b) Fluorescence intensity profile along the actin bundle outlines in the image.	64
5.2	Cuts in the nucleus of a fixed endothelial cell at various laser energies, imaged by (a) fluorescence microscopy and (b) electron microscopy.	65
5.3	Pulse energy dependence of the ablation width of cuts in the nucleus of endothelial cells measured by fluorescence microscopy (filled circles) and TEM (open circles) in three different cells a-c.	66

5.4	(a) Fluorescence microscope image of GFP-labeled microtubule network in an endothelial cell. (b) time-lapse sequence showing rapid retraction of microtubule due to depolymerization. The cross hair shows the position targeted by the laser; the triangles show the retracting ends of the microtubule. . . .	68
6.1	An actin filament in an endothelial cell irradiated with 14 kHz, 0.5 nJ for 3 s is not disrupted.	70
6.2	An actin filament in an endothelial cell irradiated with 14 kHz, 1 nJ for 3 s is severed.	71
6.3	A large cavitation bubble is launched in an endothelial cell when irradiated with 76 MHz, 1 nJ for 3 s.	72
6.4	0.5 nJ at 500 ms.	73
6.5	Threshold for ablation as a function of irradiation time and pulse energies for a 76 MHz pulse train. The shaded areas indicate regions of no disruption (lower left) and excessive cell damage (upper right).	74
6.6	Heat diffusion calculation results for maximum temperature distribution after 100 (left) and 1000 (right) pulse are deposited at a 76 MHz repetition rate and varying pulse energies	75
6.7	MPM imaging and nanosurgery setup based on a single femtosecond laser with a repetition rate pulse splitter (AO modulator). The high repetition rate pulses are used for imaging and the low (variable from single pulse to 5 MHz) repetition rate pulses are used for disruption.	78
6.8	White light illumination images of fluorescein epoxy. Lines were ablated in the epoxy at different repetition rates showing the transition from the cumulative (4.5 MHz, 900 kHz) to the single shot regime. Scale bar = 50 μm	80
6.9	Two-photon image of an endothelial cell labeled with a) Mitotracker orange mitochondria, imaged at 850 nm and b) YFP actin imaged at 950 nm; c) overlay of both images	82
6.10	SHG image of collagen structures in healthy tissue.	83
7.1	Double Six, 1967 a tensegrity based sculpture by Kenneth Snelson. Reprinted with permission of the artist. [18]	86
7.2	Severing and retraction of single stress fibers in living endothelial cell expressing YFP-actin	92
7.3	A fluorescence image of live endothelial cells transfected with YFP actin. a) and b) show different scenarios where the actin filaments are in close proximity with each other and only a single filament is cut.	94
7.4	Strain relaxing in a single stress fiber after a 300-nm hole was punched in the fiber. The hole became elliptical as it distended along the original fiber tension field line. (Bar = 2 μm)	95

7.5	Actin stress fibers retract rather than dissolve. Schematic shows predicted observations in the case of stress fiber retraction versus disassembly in response to laser incision. In the case of actin depolymerization (top), both severed ends of the bundle should disassemble, including the branch point. In the case of passive elastic retraction (bottom), the branched portion of the bifurcation will remain whole after irradiation and physically retract as an intact structure. The time lapse fluorescence images confirm this prediction.	96
7.6	Stress retraction monitored by the motion of a photobleached spot. (Scale bar = 2 μm)	97
7.7	Modeling of stress fiber retraction. (a) Fiber retraction, defined as half the distance between the severed ends, (b) physical model for viscoelastic properties of the fiber, (c) dependence of τ and (d) L_o on fiber width. The data in (c) and (d) were obtained by severing a stress fiber in each of 13 cells.	99
7.8	Contributions of active contraction versus passive prestress to stress fiber mechanics. Stress fiber bundles were incised in untreated control cells (squares, N=13), cells treated with the ROCK inhibitor Y27632 (10 mM) for 1 h (triangles, N=19), and cells treated with the MLCK inhibitor ML7 (67 mM) for 30 min (circles, N=16). Error bars represent mean \pm SE; solid lines are only visual guides. In all cases, one to two stress fibers were severed per cell in multiple cells. [19]	101
7.9	Schematic diagram of a cell plated on a flexible substrate with fluorescent beads embedded in it. As an actin filament is severed the tension relaxes and the beads in the substrate are deflected.	103
7.10	Contribution of a single stress fiber to cell traction forces and ECM displacement. (A) Confocal images of the actin stress fiber and the fluorescent beads (Arrowhead indicates the point of laser ablation; Bar = 20 μm). (B) Changes in bead displacement and ECM strain distribution. (C) Changes in cell traction as transferred to the ECM. [19]	105
7.11	Effect of cutting a single stress fiber on force transfer to the ECM and associated changes in cell shape. (A) Graph showing changes of cell traction forces relaxed into the ECM substrate measured over time after laser ablation of a single stress fiber using traction force microscopy (N=5; data are presented as mean \pm SE). (B) Quantification of the effect of stress fiber incision on the global shape of cells adherent to flexible versus rigid ECM substrates [19].	106
7.12	Caption [19]	108

List of Tables

2.1	Penetration depth in skin tissue at different wavelengths.	8
6.1	Calculated maximum radius reached for irradiation with 100 and 1000 laser pulses at a 76 MHz repetition rate for different pulse energies.	76

Acknowledgements

I would not be writing these words and would not have had so much fun getting here without the support, help and time that so many people have given me.

I would like to first and foremost thank my advisor, Prof. Eric Mazur and the group that he has established. He provided me with an encouraging and challenging scientific environment. His leadership and friendship set a very high standard to follow. The Mazur group really became my second family. I owe much what I have learned both scientifically and about coping with graduate student life to Rafael Gattass. His unending patience and infectious enthusiasm for science made it a pleasure to go into lab. I am also indebted to Jim Carey, Maria Kandyla, Jon Ashcom, Chris Roeser, Nan Shen, for helping me get on my feet in the lab. I can only hope that I have been as good of a mentor to the younger students as they have been to me.

I also had extreme pleasure getting to know Alex Heisterkamp, who has been a friend and mentor over the last three years. It has been a real privilege to work with him and learn his sometimes crazy, but always effective lab ways. His faith in me and his enduring friendship have encouraged me to try to be the best I can be. Giving me the opportunity to spend my last semester working in Germany was an amazing experience. I am truly grateful for his endless generosity and patience. And I would like to thank the rest of group at Laser Zentrum Hannover for the memorable time I spent there. My work

would not have been possible without the support and collaboration of Prof. Don Ingber and Sanjay Kumar. Their interest in pursuing new techniques and approaches led to many of the interesting results that we achieved at the end.

My time at Havard would not have been the same without the continued additions of great people to the Mazur group. With Sam I shared lab and equipment and I hope he can forgive my untidiness; Brian, Geoff, Prakriti, Loren, Mark, Tina, Eric, Jessica and Mustafa.

I had the opportunity to make many friends at Harvard, who made my days brighter and happier and often times yummiier. I loved riding and racing my bike with the Harvard University Cycling Association. HUCA attracts amazing, strong and driven people. There are few people with whom you can share the pain of long bike rides or a race in the freezing New Hampshire rain, and come out better friends at the end. Robin, Amy, Janet, and Nat, I will miss our rides through the windy, pothole-filled, picturesque New England roads.

My parents and brother have always encouraged and supported me, even when we are sometimes separated by seven time zones. Without them I would not have come to the US and definitely not been here today. I am also grateful to my late grandfather who taught me to believe in myself and gave me the power to dream big.

Steve, you have been my friend and my partner over the last many years. You pushed me further when I wanted to let go and shared in the happiness with me when I've

succeeded. Thank you for your patience, support and your love.

*Iva Maxwell
Cambridge, Massachusetts
December, 2006*

Acknowledgements of Financial Support

This thesis is based on work supported by the National Science Foundation under contract DMR-0213805, PHY-0555583 and the Materials Research Science and Engineering Center at Harvard University.

Citations to Published Work

Parts of this dissertation cover research reported in the following articles:

- [1] A. Heisterkamp, J. Baumgart, I. Maxwell, A. Ngezahayo, E. Mazur, and H. Lubatschowski, “Fs-laser scissors for photobleaching, ablation in fixed samples and living cells and studies of cell mechanics,” in *Laser Manipulation of Cells and Tissues* (M. Berns and K. Greulich, eds.), vol. 82 of *Methods in Cell Biology*, 2007.
- [2] S. Kumar, I. Z. Maxwell, A. Heisterkamp, T. R. Polte, T. P. Lele, M. Salanga, E. Mazur, and D. E. Ingber, “Viscoelastic retraction of single living stress fibers and its impact on cell shape, cytoskeletal organization, and extracellular matrix mechanics,” *Biophysical Journal*, vol. 90, no. 10, pp. 3762–3773, 2006.
- [3] I. Maxwell, C. Chung, and E. Mazur, “Nanoprocessing of subcellular targets using femtosecond laser pulses,” *Medical Laser Applications*, no. 20, pp. 193–200, 2005.
- [4] A. Heisterkamp, I. Z. Maxwell, E. Mazur, J. M. Underwood, J. A. Nickerson, S. Kumar, and D. E. Ingber, “Pulse energy dependence of subcellular dissection by femtosecond laser pulses,” *Optics Express*, vol. 13, no. 10, pp. 3690–3696, 2005.
- [5] A. Heisterkamp, I. Z. Maxwell, S. Kumar, D. E. Ingber, and E. Mazur, “nanosurgery in live cells using ultrashort laser pulses,” in *SPIE, Optical Interactions with Tissue and Cells XVI*, vol. 5695, (San Jose, CA), pp. 121–125, 2005.

Chapter 1

Introduction

Light is a powerful tool when used in biological and medical applications. As scientists, we are constantly searching for new ways to image matter, to look deeper in our bodies, to see faster processes, and to understand the underlying biological mechanisms. Since 1674 when Anton van Leeuwenhoek adapted the first microscope for biological studies, we have been using light in the quest to get a finer view of biology. At the same time light has been used as a therapeutic tool for variety of medical conditions. The advent of the laser has revolutionized biology and medicine. Now, we can monitor a virus infecting a cell, cauterize an ulcer in a patient without making a single incision, or image blood flow inside a mouse brain as it is experiencing a stroke. With improvements in laser technology there is a necessity to discover and develop new ways to use the new generation lasers to their full potential as tools in biology.

Since their introduction in the 1980's, femtosecond lasers have gained ground due to their versatile application to a large variety of problems. What makes them especially advantageous is their near-IR wavelength which has deep penetration in tissue, and their short pulse duration, which means high peak power at very low pulse energy. Through

nonlinear interactions, these laser pulses are able to create localized disruption in delicate, biological materials.

Some of the first application developed for short pulsed lasers in biology was multiphoton imaging. The excitation of a dye through a nonlinear processes is limited strictly to the focal volume of the objective lens, which allows for all optical three-dimensional sectioning.

The second, unique application for femtosecond lasers is the bulk manipulation and disruption of transparent materials, including biological matter. Because the material is transparent to the laser light, the light can be focused within the bulk without affecting any of the above lying layers. The intensity in the bulk can then reach values where nonlinear processes become important, such as multiphoton absorption, plasma generation and material ablation. When the laser parameters are chosen just right, these violent processes are confined only to the nonlinear-interaction volume, which is smaller than the diffraction limited spot and can be smaller than 500 nm across. Due to the short pulse duration there is no damage outside the interaction region. This interaction mechanism allows us to create imbedded waveguides inside in a transparent solids, to sever an axon in a *C. Elegans* and to study the mechanics of single stress fibers in a living cell.

In this dissertation we present an experimental study of the application of femtosecond laser pulses for minimally invasive subcellular nanosurgery. We determine the pulse-energy threshold by studying the laser ablated area through transmission electron microscopy. We then study the effects of pulse energy and laser repetition rate on the nanosurgery precision. Finally, we investigate the dynamics of stress fibers in adherent cells by severing single actin bundles. We visualize the retraction of the actin and model it as a viscoelastic cable. We also measure the cell deformation and the change in traction it exerts on the substrate in response to the actin disruption.

The dissertation is organized as follows:

Chapter 2 reviews the nonlinear interaction that leads to the bulk absorption and plasma-mediated ablation. We describe the absorption mechanism and the importance of the focusing, pulse energy and laser repetition rate, which have been studied in depth in transparent solids.

Chapter 3 reviews the applications of femtosecond laser for imaging and includes a detailed literature review on the use of these laser for disrupting and manipulating biological samples.

Chapter 4 describes the experimental systems that we built and used to perform these experiments. It also discusses possible improvements and further implementations.

Chapter 5 analyzes the threshold for plasma-mediated ablation in fixed cells. We confirmed the ablation and measured the width of the channels drilled in the bulk of cell nuclei using transmission electron microscopy (TEM). The minimum width measured is 250 nm. We also compared the fluorescence and TEM micrographs and determined that there exists a regime where photobleaching occurs without corresponding material ablation. The threshold for ablation is about 20% higher than that for photobleaching.

Chapter 6 determines the effect of the laser repetition rate to the pulse energy threshold necessary disruption. We compare the onset of disruption for kHz and MHz pulse trains. When the laser repetition rate is in the MHz range, heat is accumulated in the focal volume. Therefore, both the pulse energy and the exposure time are important in determining the threshold for material disruption.

Chapter 7 presents our study of the mechanics of stress fiber filaments in adherent, living endothelial cells. By severing a single stress fiber and measuring its retraction in real time, we are able to conclusively show that the stress fiber is under passive tension. By introducing drugs that inhibit various actin binding proteins, we show that the initial

tension in the stress fiber is decreased. We also studied the effect of one stress fiber on whole cell shape and traction, by plating the cells on soft substrates and measuring the displacement of the substrate and the change in cell shape after laser-cutting of the stress fiber. Our results show that a single stress filament can account for much of the whole-cell prestress.

Chapter 8 summarizes the work contained in this thesis and comments on future directions where this research can be applied. The applications for femtosecond laser pulses in biology and medicine are numerous and fruitful collaborations with biologists generates new research avenues.

Chapter 2

Femtosecond laser disruption of transparent materials

The objective of the research described in this thesis is to develop femtosecond lasers as a research tool in cell biology and to use them to study cell mechanics. The techniques employed are femtosecond laser nanosurgery for subcellular disruption and multiphoton, confocal and electron microscopy for visualization and measurement. Before delving into experimental results, we will first cover the principles underlying femtosecond laser nanosurgery.

To understand the light-matter interaction mechanism that makes femtosecond laser nanosurgery possible, we first examine the optical properties of cells and tissues, and show that biological matter is mostly transparent in the near-IR wavelengths. Then, we discuss the disruption of transparent materials through femtosecond laser induced optical breakdown.

2.1 Optical properties of tissues

The basic interaction mechanisms of light with bulk matter are reflection, refraction, scattering and absorption. The optical properties of the material at the wavelength of the incident light determine the relative contribution of each effect. Biological materials, such as tissue, have complex structure and chemical composition. Despite their complexity, their optical properties can be generalized by considering the predominant components: water, hemoglobin and melanin [1,2]. Figure 2.1 shows the absorption spectra of these three components. In the region between 0.6 and 1.2 μm there is a relative dip in absorption in all three components creating the so-called “diagnostic window” for laser-tissue interaction. Light in this wavelength range penetrates tissue more effectively than light in any other wavelength range.

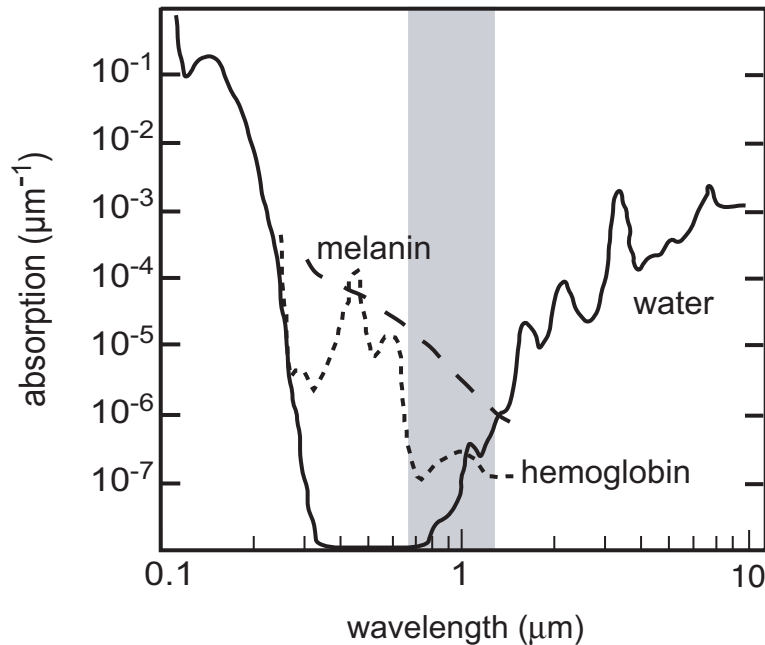


Figure 2.1: Absorption spectra of the major absorbers found in tissue. There are no efficient one-photon absorbers in cells and tissues in the near-IR spectrum, making them nearly transparent in this wavelength range. [1]

Determining the exact optical properties of tissues and specifically, the relative contribution of scattering and absorption is a complex task. The attenuation of light propagating through such a medium can be described as:

$$I(z) = I_0 e^{-\alpha z} \quad (2.1)$$

where I_0 is the incident intensity, α is the attenuation coefficient which is a combination of the absorption and scattering coefficients, and z is the propagation distance in the media. The mean free optical path then is:

$$L = \frac{1}{\alpha} \quad (2.2)$$

The optical properties for many tissues have been measured at different wavelengths. However, biological tissue can be very inhomogeneous and there can be large variation from sample to sample. Determining the exact optical properties is further complicated by the fact that tissue preparations *in vivo* and *in vitro* can differ tremendously in their properties. For example the cornea can turn from being transparent *in vivo* to essentially being opaque *in vitro* [20]. As a general illustration of the optical properties of biological tissues, the penetration depth of skin tissue (dermis) at different wavelength is given in Table 2.1. The penetration depth varies over a few orders of magnitude from the UV to the IR. While we will not be discussing skin tissue specifically, this example illustrates that the near-IR wavelengths indeed have the deepest penetration, and that penetration depths in this range can be as large as hundreds of micrometers.

Understanding optical properties of a biological specimen is necessary in order to determine the best laser parameters for a desired interaction. Variation in laser wavelength, energy, pulse duration and irradiation time can lead to vastly different effects and these

wavelength (nm)	248	514.5	830	1064	2100	2940
penetration depth (μm)	5	330	1300	1400	400	1

Table 2.1: Penetration depth in skin tissue at different wavelengths.

parameters need to be selected accordingly for the particular application. The possible interaction mechanisms are discussed in the following section.

2.2 Laser-tissue surgery mechanisms

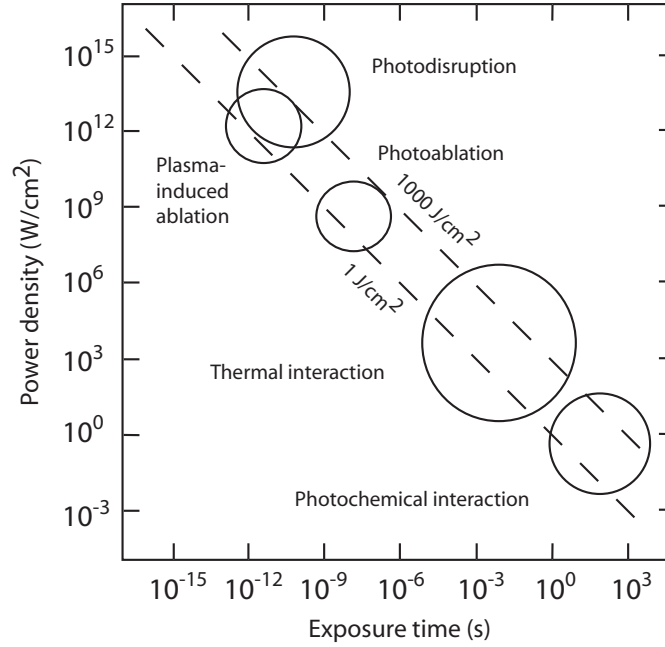


Figure 2.2: Map of laser-tissue interactions. The circles give a rough estimate of the associated laser parameters. Modified from [2].

Precise laser surgery is achieved when the desired target is exposed to the optimal laser conditions for a given interaction pathway. Laser-tissue interactions can be separated in five different categories depending on the laser power and the irradiation duration. Figure

2.2 gives a rough delineation of the interaction zones. This classification of laser-tissue interactions is empirical and describes the dominant mechanism of the interaction and often the boundary between neighboring interactions are not definitively set. The dashed lines indicate constant fluence of 1 J/cm^2 and 1000 J/cm^2 . Even though the variation in power density is not huge, it is possible to access a wide range of interactions from photochemical to plasma-mediated photodisruption.

Photochemical interactions can be produced in tissues by optically triggering changes in specific macromolecules [2]. Perhaps the most famous photochemical reactions are photosynthesis in plants and the photoisomerisation of rhodopsin in retinal cones. In medicine, photochemical reactions are used for photodynamic therapy and biostimulation. A photoactive molecule is injected into the body, then optically activated and through a complex decay path highly toxic reactants are released, causing irreversible damage to the cell structure. The optimal parameters used are low power densities and long exposure time, from seconds to minutes. Another empirical report of photodynamic therapy is biostimulation. Certain observations show that low irradiation levels with near-IR light have wound healing and anti-inflammatory properties [21]. In femtosecond laser nanosurgery, photochemical effects such as reactive oxygen species generation could add additional stress and damage to the cell.

Significant local temperature increase is the signature of thermal interactions. Depending on the irradiation type, tissue structure and temperature increase different effects can be separated: coagulation, vaporization, carbonization and melting [2]. These effects correspond to specific temperature ranges. Normal *in vivo* tissue temperature is 37°C and no measurable effect are observed for a temperature increase of 5°C . Between $42\text{-}50^\circ\text{C}$ is the onset of hyperthermia which, if it lasts for more than a few minutes, leads to irreversible necrosis. For temperatures in the range of $50\text{-}60^\circ\text{C}$, enzyme activity and energy transfer

within the cell is reduced and cell repair mechanisms are disabled. Denaturation of proteins and collagen starts at 60°C and the cell membranes become permeable above 80°C destroying intra- and extra-cellular chemical equilibrium. At 100°C water start to boil. Gas bubbles can be formed creating mechanical ruptures and promoting thermal decomposition. For temperatures above 100°C, carbonization starts and at 300°C, the cell melts. For short times, though it is around 60°C that irreversible damage to the tissue starts. While the specific temperature zones are not crucial to the femtosecond laser disruption, it is important to understand the effect of temperature increase on cells and avoid such temperature rises.

Photoablation is a method of material removal by laser irradiation. The photons directly break molecular bonds at the tissue surface which leads to molecular dissociation and subsequent ejection of material off the surface. The energy density required is high and is typically achieved with pulsed or UV lasers. The cutting precision is very high and there are few thermal effects causing correspondingly small collateral damage. However, a possible hazard for the surrounding tissue is UV absorption in the DNA which can cause mutations and genetic disease [2]. A special application of photoablation is refractive corneal surgery.

The top two interaction mechanisms shown in Figure 2.2 are plasma-induced ablation and photodisruption. They are both mediated by the optical breakdown of the material, which is possible only at very high intensities, exceeding 10^{11} W/cm². Such intensities can be reached by using short pulsed lasers. The difference that separates these two interactions is that in the first case, the optical breakdown leads to plasma generation and material disruption, while in the second case, the power density is higher and additional effects such as shock waves, cavitation bubbles and jet formation are present. In the following sections, we will describe the mechanism leading to the optical breakdown of transparent material and how it can be used for highly localized, subsurface disruption in cells and tissues.

2.3 Plasma-induced material disruption

Earlier, we showed that there is a large transparency window for near-IR wavelengths in the absorption of cells and tissues. This means that at low light intensities there is very little interaction between light and matter. Typically, when we study the propagation of light through a material, it is the material properties that determine the propagation path of the light. This is true, however, only in the regime where the light intensity is low and the interaction is linear. When the light intensity becomes high enough nonlinear effects become significant and it is possible for the light itself to affect its propagation path and change the properties of the material it is interacting with. For example, a typical Ti:sapphire amplified femtosecond laser system outputs 100 fs long pulses, at 800 nm, with an average power of 1 W and a repetition rate of 1 kHz has a peak power of 10 GW. When these pulses are focused, the peak intensity becomes 10^{14} GW/cm², and the strength of the electric field is comparable to the binding field of the electrons. This is the regime where many nonlinear processes are displayed, such as higher harmonic generation, optical parametric conversion, self-phase modulation, self-focusing, multiphoton absorption and optical breakdown [22]. The principle mechanism for creating disruption in transparent materials is laser-induced optical breakdown.

2.3.1 Optical breakdown in transparent materials

Optical breakdown of transparent materials requires a series of events to occur: the absorption of light and the creation of a free electron plasma. This can result in permanent material modification. The first step is multiphoton ionization (MPI). As the energy of a single photon is smaller than the bandgap, the simultaneous absorption of several photons is required to ionize an electron. The number of photons necessary for the promotion of the electron is determined by the energy difference between the electronic binding energy and

the energy of the single photon, Figure 2.3a [3]. For example for water has a bandgap of 6.5 eV therefore five photons at 800 nm (1.5 eV) are necessary to ionize an electron.

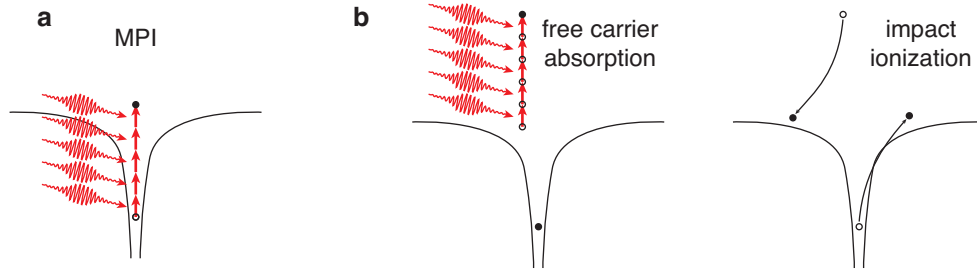


Figure 2.3: Schematic diagram of optical breakdown. First, a free electron is promoted through (MPI); then it linearly absorbs photons until its energy reaches twice that of the binding potential and it impact ionizes an bound electron. Adapted from [3].

Once an electron is promoted to the bottom of the conduction band it serves as a seed for avalanche ionization. The electron linearly absorbs photons and once its energy has reached twice that of the band gap, it can collisionally ionize with an electron in the valence band resulting in two electrons at the bottom of the conduction band, Figure 2.3b. For electrons excited in the conduction band the scattering time is on the order of 1 *fs*, making this a fast and efficient process. [23]. Through this process, it is possible to create a free electron plasma, within the duration of the laser pulse.

In order to initiate the avalanche process, there have to be some electrons already promoted to the bottom of the conduction band. Multiphoton excitation is the lead mechanism of generating these electrons when using femtosecond laser pulses. There is a laser intensity threshold above which the optical breakdown cascade will always proceed. Femtosecond laser optical breakdown is deterministic and there is no pulse-to-pulse variation in the intensity threshold. In contrast, when longer pulses, such as picosecond or nanosecond pulses are used, the laser intensity might not be high enough to generate seed electrons, and these electrons have to come from impurities and defects, or from thermal

excitations. Therefore, the threshold for femtosecond laser breakdown is deterministic and has little pulse-to-pulse energy fluctuation. This makes femtosecond pulses more favorable over longer laser pulses.

2.3.2 Plasma generation and material disruption

Through avalanche ionization the free electron density increases exponentially until a plasma is formed. The electron density grows until it approaches the critical density, where the plasma frequency matches that of the incident laser radiation. The plasma is strongly absorbing through free-carrier absorption, increasing the kinetic energy of the electrons. Because the laser pulse duration is about 100 fs, the energy transfer from the pulse to the electrons is completed before any heating of the ions can start.

The electron plasma thermalizes with the lattice within picoseconds and imparts significant kinetic energy to the ions leading to melting and vaporization. If this takes place at the surface, material removal and ablation can result. Because the material is transparent to the laser wavelength and the interaction is nonlinear, absorption can be confined to the bulk. In this case, the heated ions expand pushing into the surrounding media, resulting in density gradients, or in extreme cases, in void formation [24, 25].

Figure 2.4 is a comparison of the disruption produced in bulk glass by femtosecond and picosecond pulses [4]. As the peak intensity determines the disruption threshold, short pulses have another important advantage: very low total energy deposited in the sample for the same peak intensity. Picosecond pulses produce additional damage due to the large energy deposition and lead to material heating and cracking. This is the reason for the laser size of the damage and the cracks seen in the picosecond sample in Figure 2.4. For biological applications, we demand the highest spatial precision for the least amount of deposited energy in order to avoid thermal effects. Therefore femtosecond pulses have a

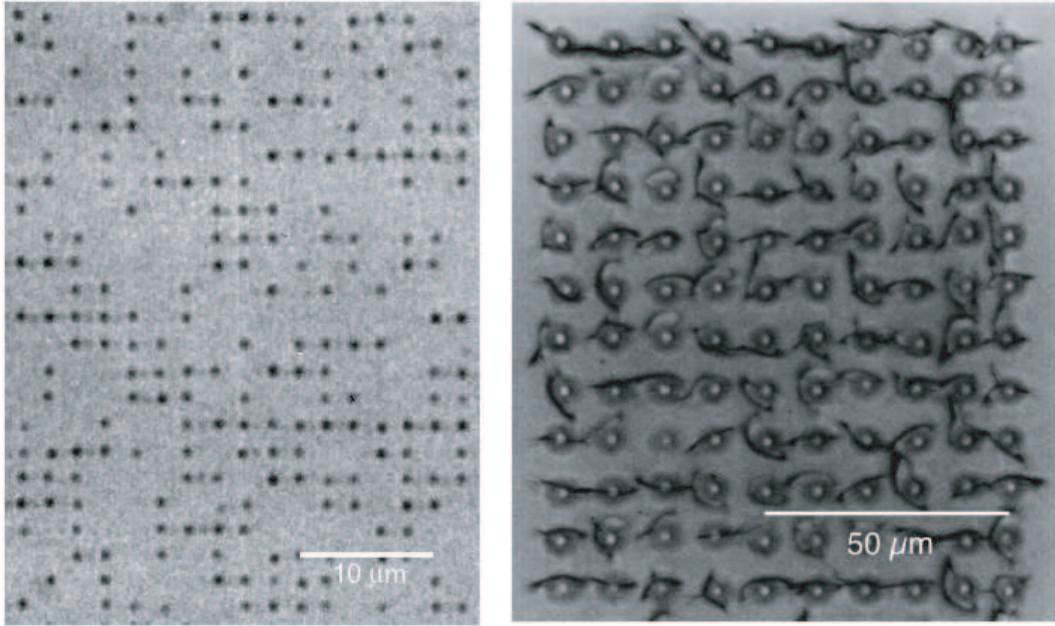


Figure 2.4: Damage produced under the same focusing conditions in fused silica by a) 100 fs pulses with 2 μm spacing and b) 200 ps with 10 μm spacing [4].

clear advantage over longer pulses.

Since the optical breakdown threshold is intensity dependent, stronger focusing conditions (higher numerical aperture (NA)) require lower pulse energy to reach the threshold. This is another way to reduced the total deposited energy and minimize side effects outside the focal volume. Figure 2.5 plots the pulse energy vs. NA at threshold for Corning 0211 glass. The fit line is a constant intensity line. For very high NAs the threshold energy becomes only a few nanojoules. In this regime, nonlinear propagation effects such as self-focusing and filamentation do not play an important role and do not affect the extent of disruption [5].

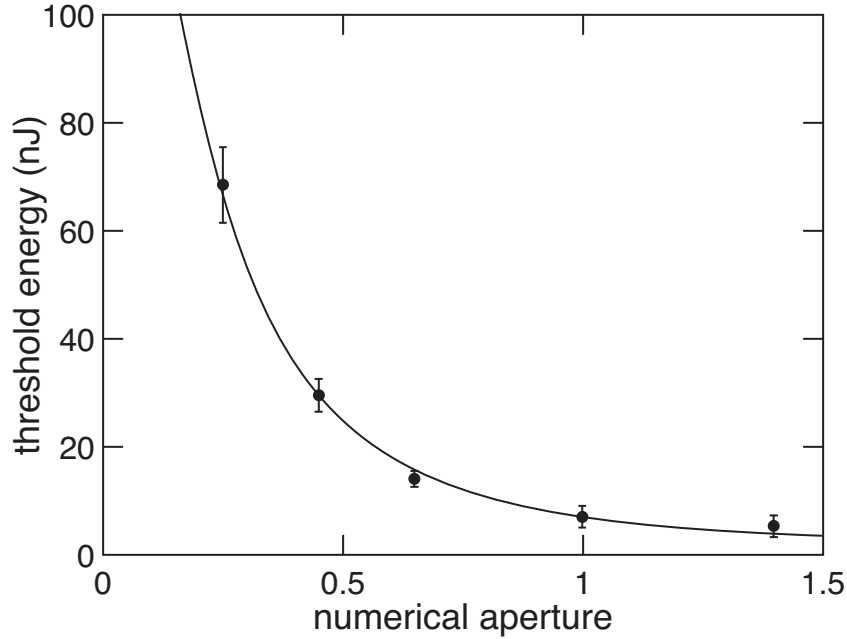


Figure 2.5: Threshold for material disruption as function of NA and pulse energy [5].

2.4 Photodisruption

Both plasma-induced ablation and photodisruption result from nonlinear optical breakdown. The delineation between them is in the total amount of energy deposited in the focal volume. Figure 2.6 outlines the threshold intensity necessary for material disruption as a function of pulse duration. For short pulses there is a smooth transition from plasma-induced ablation to photodisruption. The difference between the two regimes is that in the first case the pulse energy is sufficient to generate a plasma and modify the material only within the focal volume, while in the second case the pulse energy forms a more energetic plasma and generates a shockwave. When soft material, such as fluids, gels or tissues are photodisrupted, cavitation bubbles and jets can form. The mechanical effects due to the launching of the shock wave and subsequent cavitation bubble can be used for faster

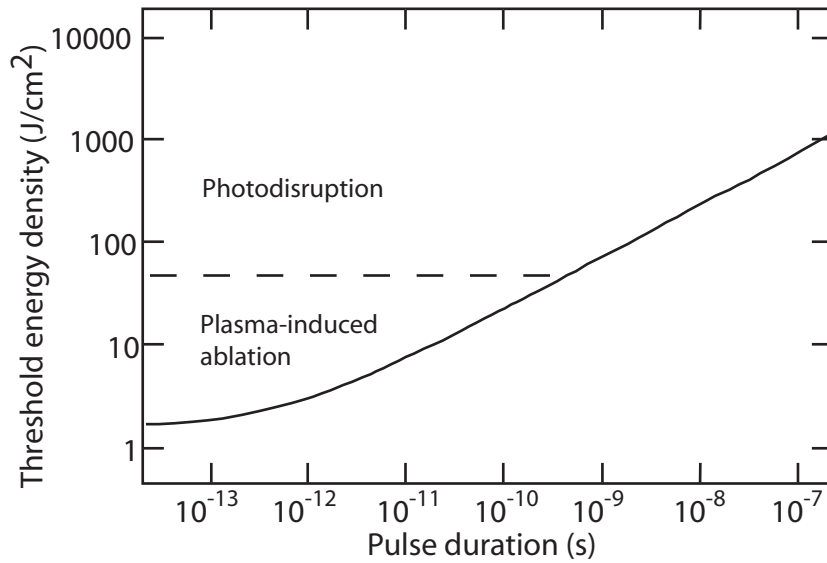


Figure 2.6: Threshold for material disruption as function of NA and pulse energy.

material ablation or can be detrimental and incur undesirable out focus damage (such as the cracking of glass in Figure 2.4 b).

2.5 Bubble formation in water

The optical breakdown of water is a good approximation to the femtosecond ablation in cells and tissues as they are comprised of 80% water. Through nonlinear absorption and plasma generation is possible to vaporize water both at the surface and in the bulk. One of the effects of photodisruption is the launching of a pressure wave and the formation of a cavitation bubble. The size of the region affected by this mechanical disruption increases with the pulse energy and can exceed many times the focal volume [26]. The threshold for cavitation bubble is intensity dependent and the size of the bubble scales down with shorter pulses and tighter focusing. For example, a 10-mJ nanosecond pulsed produces a bubble with a half a millimeter radius [27]. For shorted pulse durations the size of the bubble

is much smaller. A 1- μJ , 100-fs pulse produces cavitation bubble of 11 μm [28]. Force transducer measurements of the pressure wave have established a threshold was of 0.2 μJ per pulse for 100 fs pulse at 0.65 NA focusing [4]. For subcellular surgery we use less than 5 nJ per pulse and for a 1.4 NA objective we estimate that the affected zone is less than 1 μm , which is on the order of the beam size at the focus.

2.6 Laser repetition rate dependence on photodisruption

The laser repetition rate plays an important role in the disruption mechanism. The dependence of damage morphology on the laser repetition rate has been extensively studied in glasses [29,30]. These studies show that two distinct regimes can be defined. At low repetition rates, in the kHz range, damage results solely from the breakdown mechanism described thusfar. In this regime, the pulses are separated by milliseconds and typical heat diffusion time (such as for fused silica) is about 1 μs for a 1 μm^3 volume. Each laser pulse acts independently to generate disruption, and the structures created are limited to the focal region. At high repetition rates, usually in the MHz, the damage is a cumulative process due to the rapid energy energy deposition. The time interval between pulses is as short as nanoseconds, which is significantly shorter than the microseconds required for heat diffusion. The structural changes result from the heat from successive pulses accumulating in and around the focal volume and melting the material. The MHz pulse train acts as a point source of heat at the focal volume within the bulk of the material. The longer the material is irradiated the higher the temperature becomes and the larger the affected area. Melting and resolidification up to 50 times the beam waste has been demonstrated [6,31]. In this cumulative regime, the laser repetition rate, number of pulses, and irradiation time determine the size and morphology of the disrupted area.

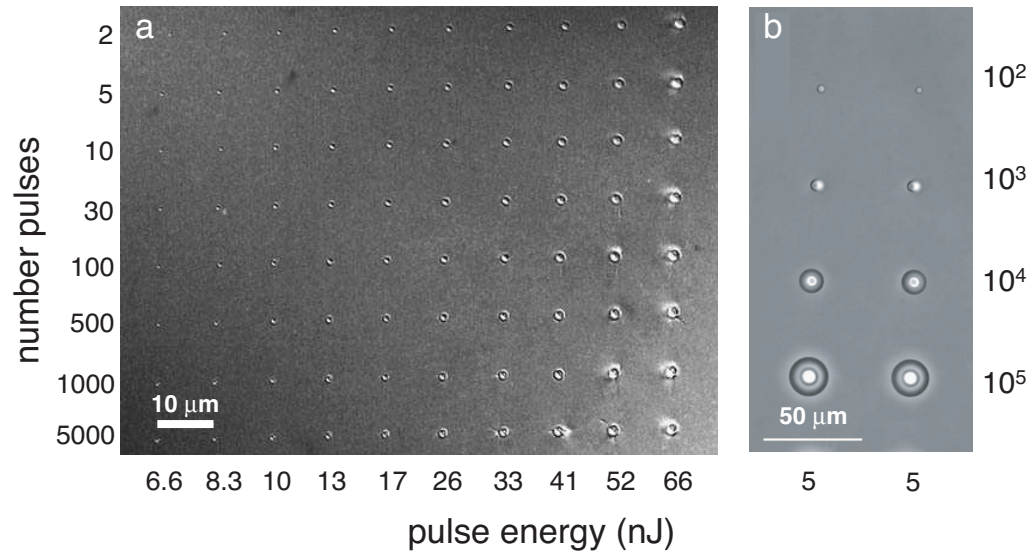


Figure 2.7: Damage in Corning 0211 glass at a) 1 kHz [3] and b) 25 MHz laser repetition rate [6].

Figure 2.7 illustrates the difference in morphologies resulting from different laser repetition rates. Corning 0211 glass was irradiated with a 1 kHz pulse train (Figure 2.7a) and a 25 MHz pulse train (Figure 2.7b) focused by a 1.4 NA objective. In the first case the pulse energy and the number of pulses were varied. The size of the structures remain constant for different number of pulses at the same pulse energy. Increasing the pulse energy results in somewhat larger features, though for all energies the focusing strength limits the size of the structure. For MHz repetition rate however, the size is determined by the number of pulses deposited and it is significantly larger than the focus limited spot, due to the heat accumulation process. Therefore, when optimizing the laser interaction parameters, we have to determine whether we are in the single shot or the cumulative regime.

2.7 Summary

The optical breakdown of transparent materials is possible via multiphoton absorption, avalanche ionization and plasma generation. This leads to material disruption, which can be localized within the bulk of the sample. The extent of the disrupted volume can be determined by choosing the pulse energy, focusing condition and laser repetition rate. The optical transparency of cells and tissues in the near-IR wavelengths allows this technique to be used for bulk tissue disruption and subcellular nanosurgery.

Chapter 3

Applications of femtosecond lasers in biology

In this chapter we will examine the applications of femtosecond lasers in biology. First we will briefly describe the nonlinear imaging techniques made possible through the use of short pulsed lasers. We will then review previous work done by our group and others in the combined field of multiphoton microscopy and femtosecond laser subcellular nanosurgery.

3.1 Nonlinear imaging

Femtosecond lasers were initially introduced to biology as tools for imaging. They offer the best noninvasive means of fluorescence microscopy in tissue slices and living animals. Their short pulse duration and near-IR wavelength make them ideal for deep tissue imaging, optical slicing and three-dimensional reconstruction. The first two-photon microscope was demonstrated by Denk in 1990 [32]. The development of fluorescent proteins and transgenic animals for whole tissue labeling has led to an increased use of multiphoton

microscopy and noninvasive imaging over the last decade [7].

Multiphoton microscopy (MPM) is a laser scanning microscopy technique that uses nonlinear absorption to excite fluorescence. Unlike confocal microscopy, where the excitation occurs in the entire illuminated region of the sample, the multiphoton excitation is limited only to regions of high intensity. Figure 3.1 illustrates linear and two-photon excitation in a fluorescently labeled solvent in a cuvette. Linear absorption occurs throughout the entire focusing cone, thus the entire propagation path is clearly visible. On the other hand, the two-photon excitation is intensity dependent and fluorescence is emitted only in the focal volume. The localized excitation effectively results in confocal-like imaging. In order to construct a full image of the sample laser beam is raster scanned. By changing the focusing depth different planes can be imaged and three-dimensional projections constructed. MPM has been used to study the physiology, morphology and cell-cell interaction in a variety of systems from single cells to tissues and live animals [7].

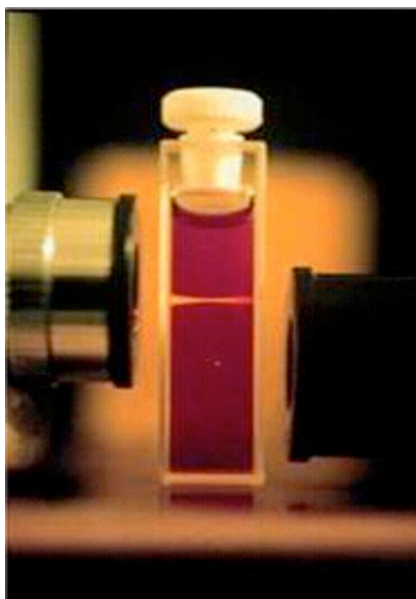


Figure 3.1: Linear (from the left) and two-photon (from the right) excitation of fluorescein [7].

Although, two-photon excited fluorescence is the primary mode of MPM, other nonlinear excitations such as three-photon excited fluorescence, second- and third-harmonic generation imaging (SHG, THG) and coherent anti-Stokes Raman spectroscopy (CARS) can also be used for imaging of biological systems. In fact, SHG was one of the first nonlinear imaging technique proposed for nonlinear biological imaging almost 20 years ago [33]. All these nonlinear modalities are possible with the use of short pulsed lasers.

The phenomenon of multiphoton absorption was first predicted by Maria Goeppert-Mayer [34]. Two-photon microscopy depends on the simultaneous absorption of two photons of half the energy of the single photon normally required. The excited fluorophore then emits a photon as though it were excited through linear or one photon absorption. This process requires that the two photons interact virtually simultaneously with the molecule (within 0.1 fs), resulting in a quadratic rather than linear dependence on the light intensity [7]. Thus the interaction occurs only the focal volume, where the intensity is above the two-photon absorption threshold, as depicted in Figure 3.1.

The necessity to use short pulsed lasers for two-photon microscopy comes from the low two-photon absorption cross-section. The two-photon cross-section, σ_2 , is a measure of the probability of the simultaneous absorption of two photons. It is measure in units of Goeppert-Mayer (GM), where $1 \text{ GM} = 10^{-50} \text{ cm}^4$. Most common fluorophores have cross-sections of 1-300 GM. The intensity of the excited fluorescence $I_f(t)$ is proportional to the cross-section times the input laser intensity squared:

$$I_f(t) \propto \sigma_2 I_0(t)^2 \quad (3.1)$$

Typically the laser beam is scanned over the samples and the signal from any given point is averaged over time:

$$\langle I_f(t) \rangle \propto \sigma_2 \langle I_0(t) \rangle^2 \quad (3.2)$$

Since the fluorescence intensity depends on the average excitation intensity, for a pulsed laser with pulse duration τ and repetition rate f the expression becomes:

$$\langle I_f(t) \rangle \propto \frac{\sigma_2 \langle I_0(t) \rangle^2}{f\tau} \quad (3.3)$$

For 100 fs pulse and laser repetition rate of 80 MHz, the two-photon excitation probability increases by a factor of $1/f\tau \approx 10^5$. Therefore, for an excitation produced by 1 mW of pulsed laser, we need 100 W of continuous wave (CW) power. Not only is the feasibility of such a system a problem, but the thermal load introduced to the sample makes CW laser practically impossible to use for nonlinear imaging of biological systems. Thus, femtosecond lasers offer the advantage of delivering the high peak intensities needed for the two-photon excitation, but have low average power, which avoids thermal damage to the specimens.

3.1.1 Two-photon excitation spectra

The two-photon absorption cross section has a wavelength dependence. Therefore efficient two-photon excitation requires not only short laser pulses, but also appropriate wavelength selection. In general, the maximum frequency of the two-photon excitation cross-section can be approximated by doubling the frequency of the single-photon excitation peak. However, because the selection rules are different for one-photon and two-photon excitation, often there are considerable deviations from this rule [7]. For example Figure 3.2a shows one- and two-photon absorption peaks for the Rhodamine B, which deviate significantly from this rule. Therefore, the exact two-photons absorption cross sections have to be independently measured.

The two-photon excitation spectra for fluorescent proteins¹ are plotted in Figure 3.2b. The excitation maxima for these proteins range from about 850 to 1000 nm. The two- and three-photon excitation spectra were measured for a variety biologically significant molecular fluorophores [35–38]. Femtosecond lasers are very well suited for the excitation of these fluorophores, as their wavelength is typically in the near-IR. For efficient two-photon microscope systems however, a tunable laser source, which can cover the 700-1000 nm range, is necessary.

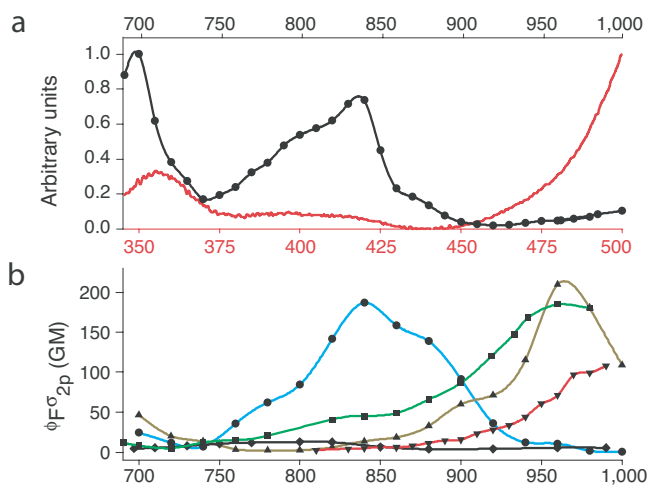


Figure 3.2: Two photon action cross-sections (absorption cross section multiplied by the fluorescence quantum yield). a) Two-photon action spectrum of Rhodamine B (black) compared to the one-photon absorption spectrum (red). b) Two-photon action spectra of five common fluorescent proteins: eGFP (green), CFP (cyan), YFP (yellow), Discosoma Red (dsRed; red) and wild type GFP (wtGFP; black). [7]

3.1.2 Intrinsic autofluorescence excitation

It is especially desirable to observe biological systems in their native state, without the added perturbation of chemical labels. In some cases this is possible due to the

¹There are a number of engineered fluorescent proteins (FPs) engineered at different excitation/emission wavelengths and some of them are: green fluorescent protein (GFP), which can be enhanced (eGFP) or wild type (wtGFP), yellow (YFP), cyan (CFP).

fluorescence of intrinsic molecules native to the biological specimen such as NADH, tryptophan, serotonin, elastin and many others [8]. These molecules can be excited through multiphoton absorption and then their fluorescence is collected and a three-dimensional image can be reconstructed. Figure 3.3 shows the two-photon absorption and emission of a few of these intrinsic markers. The intrinsic emission of these native molecules enables the three-dimensional, high resolution imaging of unstained tissues (see Chapter 4).

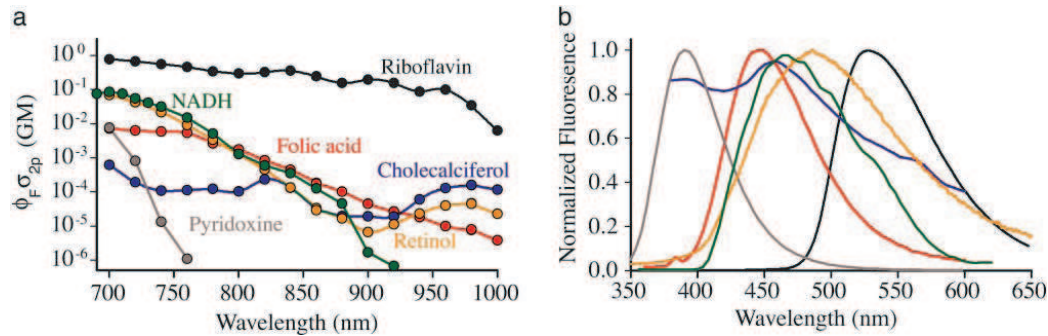


Figure 3.3: Two-photon action cross sections (absorption cross section multiplied by the fluorescence quantum yield) and emission spectra from a basis set of biological molecules. (a) Action cross sections of six molecules that contribute much of the intracellular two-photon excitation intrinsic fluorescence. All compounds were measured in buffered (pH 7.2) saline solution, except retinol and cholecalciferol (vit D), which were measured in EtOH. Riboflavin, cholecalciferol, and NADH were measured at 100 μ M; retinol, folic acid, phyloquinone, pyridoxine, and nicotinamide were measured at 500 μ M. (b) Emission spectra of the compounds shown in a) (measured in the same solvents). [8]

3.1.3 Second- and third-harmonic generation imaging

Another intrinsic imaging modality is higher harmonic conversion of the excitation wavelengths. An incident electric field $E(t)$ on a material induces a polarization $P(t)$:

$$P(t) = \epsilon_0 \chi^{(1)} E(t) \quad (3.4)$$

where the constant of proportionality $\chi^{(1)}$ is the linear susceptibility [22]. When the laser intensity is high this linear approximation is no longer valid. The higher order dependence of the polarization on the applied electric field can be expressed as power series in \mathbf{E}

$$\begin{aligned}\mathbf{P} &= \epsilon_0[\chi^{(1)}\mathbf{E} + \chi^{(2)}\mathbf{E}\mathbf{E} + \chi^{(3)}\mathbf{E}\mathbf{E}\mathbf{E} + \dots] \\ &= [\mathbf{P}^{(1)} + \mathbf{P}^{(2)} + \mathbf{P}^{(3)} \dots]\end{aligned}\tag{3.5}$$

The constants $\chi^{(2)}$ and $\chi^{(3)}$ are the second- and third- order nonlinear susceptibilities and $\mathbf{P}^{(2)}$ and $\mathbf{P}^{(3)}$ are the respective higher order nonlinear polarizations.

The incident electric field, in the case we are considering of monochromatic laser irradiation, is at a frequency of ω and the higher order nonlinear polarization is produced at a multiple of this frequency. The higher order polarization, in turn, drives a radiation field at its corresponding frequency. Second and third harmonics are described by the polarization:

$$\begin{aligned}P^{(2)}(2\omega) &\propto \chi^{(2)}E^2 \\ P^{(3)}(3\omega) &\propto \chi^{(3)}E^3\end{aligned}\tag{3.6}$$

Most isotropic materials are centrosymmetric which means that they have inversion symmetry. If we consider a spatial inversion we have that $\mathbf{P}^{(2)} \rightarrow -\mathbf{P}^{(2)}$, $\mathbf{E} \rightarrow -\mathbf{E}$ but $\chi \rightarrow \chi$, because of the material inversion symmetry. We can then write:

$$-\mathbf{P}^{(2)} = \epsilon_0\chi^{(2)}(-\mathbf{E})(-\mathbf{E}) = \mathbf{P}^{(2)}\tag{3.7}$$

so $\mathbf{P}^{(2)} = 0$ can be true only if $\chi^{(2)} = 0$. This argument holds for all even higher order terms in the power expansion of the polarization.

Therefore, in order to be able to generate a second harmonic, we need a medium with at is non-isotropic and some break in its symmetry exists. This is possible in many crystalline materials and in some biological protein structures, such as collagen or skeletal

muscle. The efficiency of the conversion depends on the excitation wavelength, the type of structure studied (collagen, skeletal muscle, etc.), the relative polarization of the light with respect to these protein fibers, and the forward or reflected mode of detection.

The second harmonic generation (SHG) signal is, by definition, at half the illumination wavelength and it is therefore easy to spectrally separate from other fluorescence sources in the sample. The strength of the SHG signal is observed to decrease only linearly with depth when measured in a polymerized gel made up of type I rat-tail collagen, Figure 3.4 [9]. Similarly to fluorescence excitation, SHG can be used to create three-dimensional image stacks.

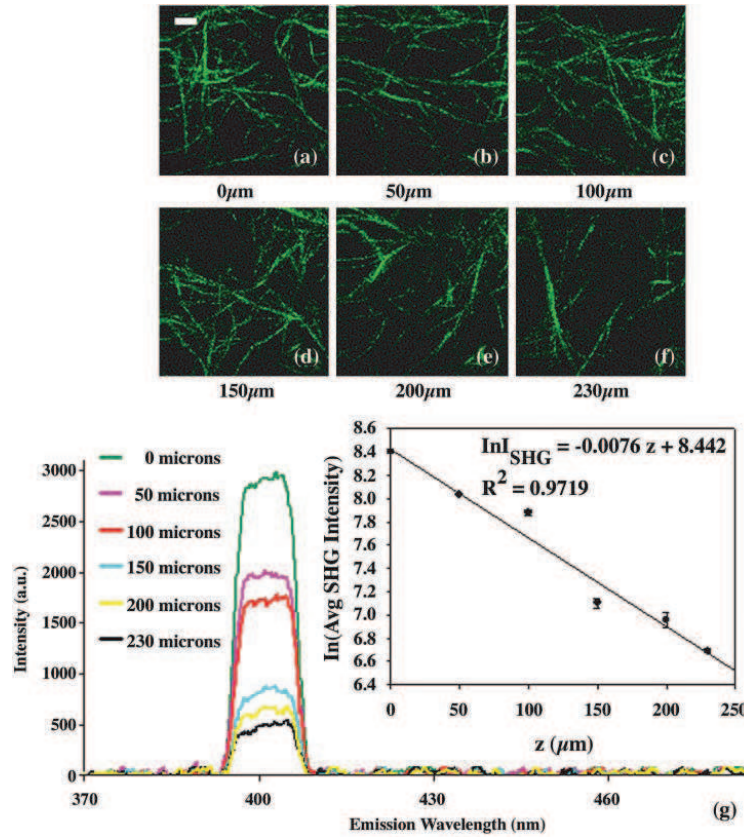


Figure 3.4: SHG image from RAFT collagen at depths of 0, 50, 100, 150, 200 and 230 μm for $\lambda_{ex} = 800 \text{ nm}$ (a-f) (Bar = 5 μm). The corresponding spectra and plot of SHG signal intensity vs. depth are shown in (g). [9]

Third-harmonic generation can also be used for imaging of biological structures. THG signal can be produced at interfaces in transparent media with low intrinsic contrast [39]. Debarre *et al.* showed that third-harmonic generation imaging can be used to detect micrometer sized lipid bodies in cells, plant seeds and intact tissue [40]. THG is a weak process that requires high intensities. Photodestructive effects are present when the wavelengths used are in the 700-900 nm [41]. Therefore, for long term, sustained THG imaging 1,100-1,200 nm wavelength range is more efficient and less damaging to the cell.

Autofluorescence, SHG, and THG imaging can all be combined together to image cells and the extra-cellular environment in tissue [8, 40]. They are native to the tissue and changes in these markers can be used as an indication of morphological and chemical changes due to diseases. For example changes in the NADH fluorescence can be used to distinguish normal and cancerous tissue [42]. Structural changes in the extra-cellular matrix in diseased tissue can be mapped using SHG imaging. Combining these imaging modalities with femtosecond disruption offers new avenues for the study of living systems.

3.1.4 Photobleaching and photodamage in MPM

Photobleaching is a process through which a fluorophore permanently loses its ability to fluoresce due to a non-reversible photo-induced chemical change. In a fluorescence cycle, a molecule is excited to a singlet state, transitions into a triplet state and then decays back to the ground state emitting a photon. The triplet state is relatively long lived compared to the singlet state having sufficient amount of time to interact with the environment and decay to a state which cannot be optically excited. The photobleaching propensity is then dependent both on the molecular structure and the local environment. Photobleaching rates are fluorophore dependent, some emitting only a few photons while other undergo millions of cycles before photobleaching.

Photobleaching of samples is generally slower for multiphoton excitation, due to focal-volume localized excitation of the fluorophore. Each focal spot is typically illuminated only for a few microseconds greatly decreasing the overall sample exposure time. There is some indication, however, that locally, within the excited volume, photobleaching is accelerated for two-photon excitation than for conventional microscopy [43]. By carefully studying the photobleaching dependence on excitation power, wavelength and pulse shape it is possible to prolong the imaging time [43,44]. It is necessary to point out that higher harmonic imaging does not suffer from photobleaching as there is no electronic excitation and moreover there is no energy deposited in the sample.

Photodamage is another possible side effects in biological samples that are studied for long periods of time. In contrast to linear excitation in confocal imaging, two-photon excitation reduces the overall photodamage by limiting it to the narrow region around the focal plane. For example, two-photon excitation imaging of mitochondrial distribution in hamster embryos over 24 hours did not jeopardize the embryo's development, while 8 hours of confocal imaging significantly compromised it [45].

The nonlinear nature of the two-photon near-IR excitation, requires very high intensities at the laser focus, and could can potentially inflict irreversible photodamage to living samples during long observation periods. There are reports that prolonged femtosecond laser irradiation even at relatively low power can cause reactive oxygen species production, DNA strand breakage and apoptosis like death [46]. Depending on the excitation intensity, photodamage and higher order mechanism become important as a damage mechanism [47,48]. Higher order nonlinear excitation could reach the regime of large thermal accumulation or optical breakdown, discussed in the previous chapter.

3.1.5 Summary

Multi-photon microscopy is a way to obtain high resolution images hundreds of micrometers deep within living tissues. It requires short pulsed lasers to achieve efficient fluorophore excitation and still have low energy deposited in the sample. The development of fluorescent proteins made feasible the study of living samples in as close as possible to their natural state. There are also a number of naturally occurring molecules and proteins that have strong autofluorescence signals and can be used for live tissue imaging. While photobleaching and photodamage have to be considered when observing any systems for long periods of time, their relative effects in multi-photon microscopy are smaller than that in conventional linear imaging.

3.2 Femtosecond laser cell and tissue disruption

In Chapter 2 we examined the physical mechanism of ablation of transparent materials through their optical breakdown and showed that the optical properties of tissues allow them to undergo this disruption mechanism. Our group is among the pioneers in the use of femtosecond lasers for subcellular disruption. In parallel with our work there are number of other research groups who are also working on similar applications. In some cases the disruption is combined with MPM, drawing on the versatile use of femtosecond lasers. Here is an overview of many of the interesting results, complementary to our work, that have been published in this field over the last few years .

3.2.1 Plasma-induced ablation for subcellular nanosurgery

The first published report of femtosecond laser subcellular nanosurgery was by Karsten Koenig's group in 1999, where he showed that it was possible to drill holes in a single

chromosome by tightly focusing high repetition rate femtosecond laser pulses, Figure 3.5b [10]. Subsequently, they sliced through chromosomes both *in vitro* and *in situ*. The severed chromosomes are visualized by atomic force microscopy, Figure 3.5a, or by monitoring cell division and observing the severed chromosome piece did not participate in the cell division process [1]. They demonstrated single cell gene transfection by creating a 100 nm sized puncture in the cell membrane that stayed open long enough to allow for eGFP tagged protein to infuse in the cell and later be expressed [11]. A summary of this result is shown in Figure 3.5c.

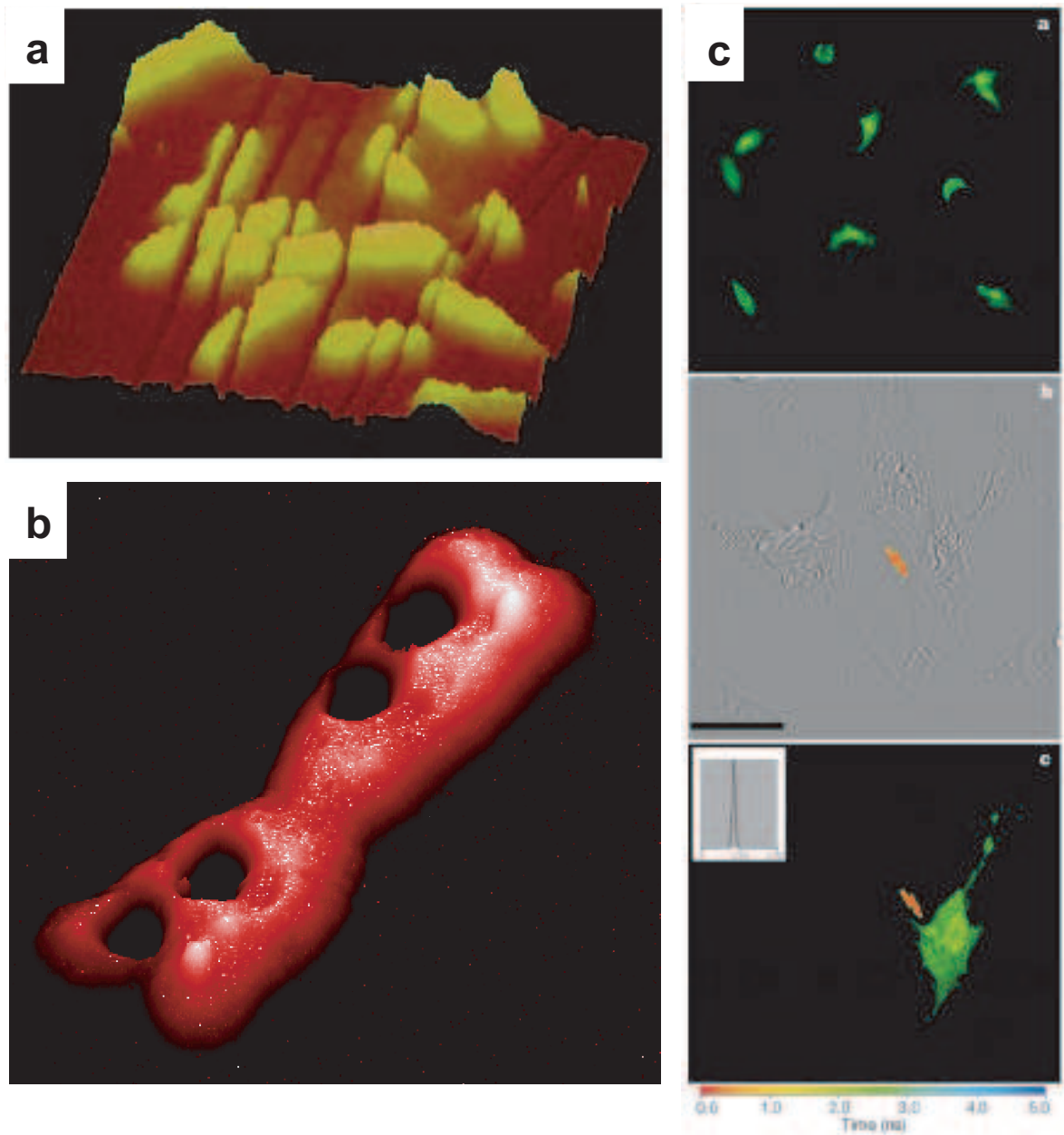


Figure 3.5: Femtosecond laser nanodissection of human chromosomes. a) slices through a chromosome are created by scanning the laser beam in parallel lines across [1] and b) holes are drilled in the chromosome by fixing the laser on a spot [10]; c) Targeted cell transfection through laser irradiation of the cell membrane. eGFP is expressed in the irradiated cells. Scale bar, 25 μm . [11]

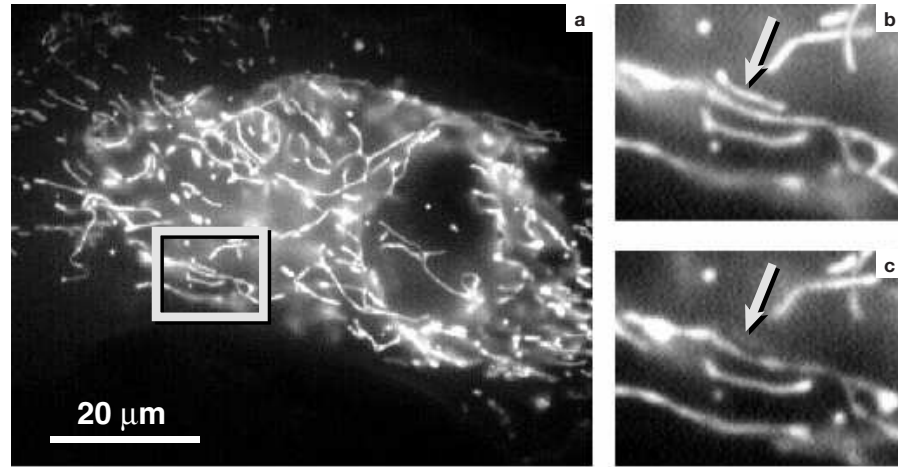


Figure 3.6: Ablation of a single mitochondrion in a living endothelial cell. (a) Fluorescence microscope image showing multiple mitochondria before femtosecond laser irradiation. Target mitochondrion (marked by arrow) (b) before and (c) after laser ablation with 2-nJ pulses [12]

The first subcellular organelle disruption with low repetition rate pulses was presented by our group in 2001 [12]. A single mitochondrion in living cells is disrupted through femtosecond laser irradiation without compromising the cell's viability [12]. To visualize the mitochondria, capillary endothelial cells were transfected with eYFP fused to cytochrome C oxidase Figure 3.6a. The cell was positioned such that the laser was focused in the middle of a single mitochondrion. Figure 3.6b and 3.6c show the ablation of a single mitochondrion, about 5 μm in length and separated by less than 1 μm from multiple neighboring mitochondria. After irradiating a fixed spot on the organelle with a few hundred 2-nJ laser pulses at a 1-kHz repetition rate, the entire mitochondrion disappears from the image, whereas neighboring mitochondria are not affected by the irradiation despite being only a few hundred nanometers away (Fig. 3.6c). Even though the laser is focused to a 0.5 μm diameter spot in the center of the mitochondrion and remains stationary during the irradiation time, the fluorescence immediately disappears throughout the entire mitochondrion over a length

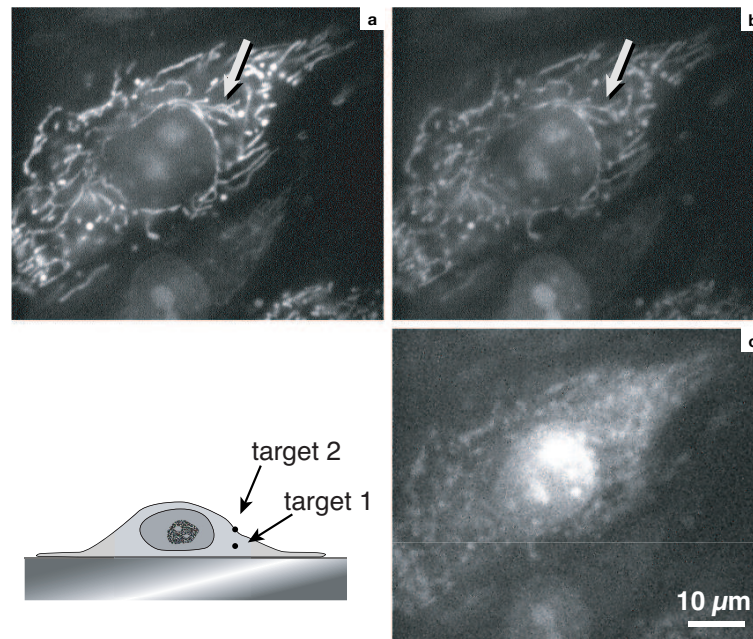


Figure 3.7: Ablation of a mitochondrion in a live cell without compromising cell viability. Fluorescence microscope images of a live cell containing EYFP-labeled mitochondria in a cultured medium containing ethidium bromide (a) before femtosecond laser irradiation, (b) after ablation of a single mitochondrion within its cytoplasm (target 1 in diagram at bottom left), and (c) after irradiation of the apical cell membrane (target 2). An increase in nuclear ethidium bromide staining is only observed after irradiation of the apical membrane. [12]

scale of up to tens of micrometers. These observations demonstrate that local ablation causes a major structural change in the target mitochondrion and results in destruction of the entire mitochondrion, but not its neighbors. This result has direct evidence that mitochondria do not form an interconnected network.

While the dissection of a single mitochondrion did not cause any apparent distress to the cell, a test was performed to verify that the membrane is not ruptured during the nanosurgery [12]. Cells were incubated with the DNA-binding dye ethidium bromide. The dye cannot penetrate through the cell membrane and little nuclear fluorescence is observed in living cells prior to laser exposure, Figure 3.7a. After dissecting a single mitochondrion with 2-nJ pulse energy there is no detectable change in the nuclear fluorescence (Figure

3.7b). In contrast, when we focused the laser beam at the top surface of the cell and irradiated the apical cell membrane, the intensity of fluorescent signal from the nucleus immediately increased by a factor of ten as the ethidium bromide rapidly diffused into the cell through the incision in the surface membrane (Figure 3.7c). In conjunction with the absence of any morphological changes in the cell or other mitochondria over a period of one hour following ablation, these results show that nanosurgery can be used to selectively ablate internal cell structures without inflicting generalized injury or causing cell necrosis.

There are number of other groups who have since addressed questions regarding mitochondrial ablation in living cells. Watanabe *et al* [49] ablated mitochondria using high repetition laser pulses and studied their fragmentation. They also observed that cells undergo normal division and are fully viable after the laser intervention. While many of the proof-of-principle experiments on femtosecond laser ablation were performed on mitochondria, there a number of other studies currently underway directed at the role of mitochondria in apoptosis [50].

In addition to disrupting subcellular organelles femtosecond lasers can be used to dissect neurons within living tissues or animals. The nematode worms *C. elegans* is particularly well suited to femtosecond laser nanosurgery due to its transparency and size. The invariant neural circuit of *C. elegans* totals 302 neurons and encodes a universal behavior. The study of the individual neuron function has been limited to observing behavioral changes in mutant worms. Femtosecond laser dissection enables us to directly observe the function of individual neurons by severing neuronal fibers, much like cutting wires in an electrical circuit. The function of a neuron or neuronal part can then be identified by observing behavioral changes after the surgery. An example of this is the study coming from our group, by Chung *et al.*, on the thermotactic behavior of the nematodes. *C. elegans* retain a memory about the temperature at which they were cultivated, and when placed at

a higher temperature they crawl down the gradient toward the cultivation temperature [13]. Through genetic mutations the AFD neuron was implicated in this cryophilic behavior, but the exact sensing mechanism and signal processing remained unknown.

Through femtosecond laser nanosurgery it is possible to ablate the neuronal cell bodies and the sensory dendrites to investigate their comparative contribution to the cryophilic movement. Figure 3.8 is a confocal microscope image of a GFP transfected AFD neuron pair a day after one of the dendrites was cut. Severing the dendrites in young adult worms permanently abolishes these dendrites' sensory contribution. The AFD neuron also regulates the cryophilic bias of the worm, but there is no evidence that it does so by generating an opposing thermophilic behavior. By disrupting other neurons, interconnected with the AFD it was possible to isolate the source of the cryophilic behavior to the AFD neuron.

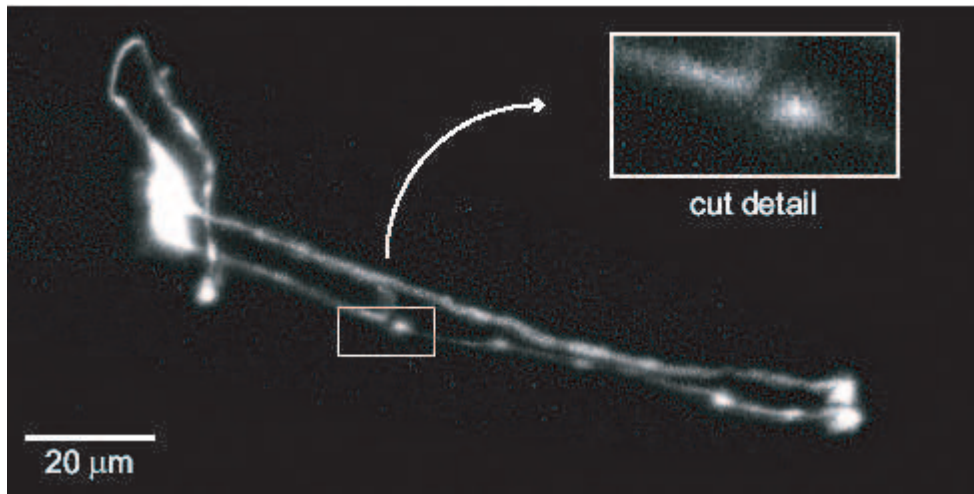


Figure 3.8: Confocal microscope image of a GFP-labeled AFD neuron a day after severing one of the dendrites [13]

In another set experiments on neuron ablation in *C. elegans*, Yanink *et al.* severed the axons that controls the crawling motion of the animal, Figure 3.9a. After the laser nanosurgery the backward crawl of the nematode was greatly hindered. Remarkably,

however, the normal locomotion of the worm gradually returned within 24 hours in all the worms Figure 3.9c. Some of the axons also exhibited partial or full regrowth when they were reimaged Figure 3.9b. Femtosecond laser nanosurgery can facilitate the understanding of neural regrowth and the important biochemical and genetic pathways responsible for neuronal regeneration.

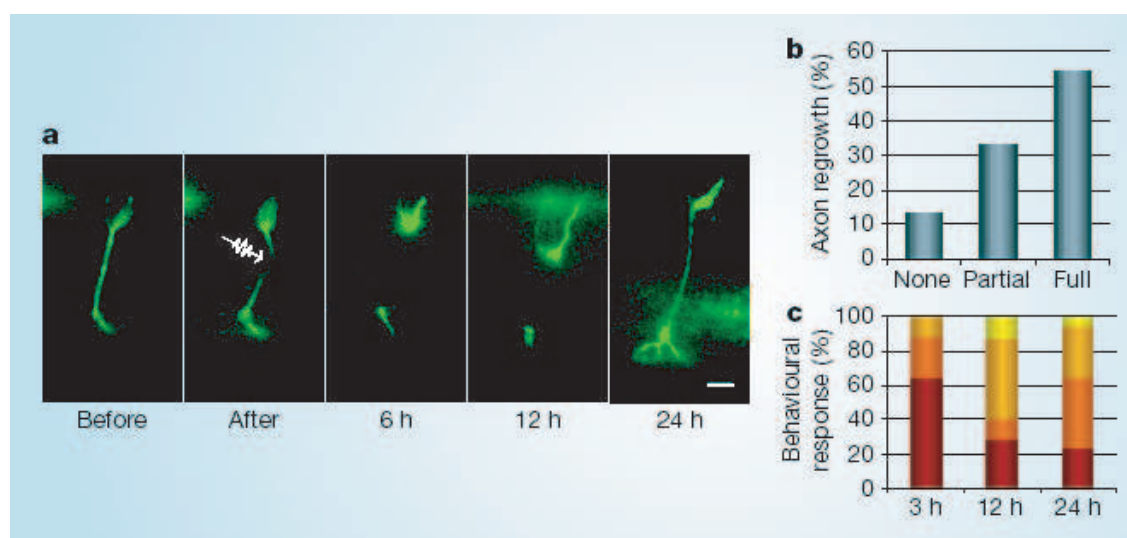


Figure 3.9: Femtosecond laser axotomy in *Caenorhabditis elegans* worms using 100 pulses of low energy (40 nJ) and short duration (200 fs) and a repetition rate of 1 kHz. (a) Fluorescence images of axons labelled with green fluorescent protein before, immediately after, and in the hours following axotomy. Arrow indicates point of severance. Scale bar, 5 μm . (b) Statistics of axon growth 24 h after axotomy, based on fluorescence images ($n=52$ axons). (c) Time-course analysis of backward motion of worms following axotomy. Seventeen worms were scored blindly at different time points (for criteria, see supplementary information). Improvement in backward motion was graded as four levels from shrinker behaviour (dark red) up to wild type behavior (yellow) in the hours following axotomy. [14]

The experiments described here cover some of the initial work on subcellular femtosecond laser nanosurgery. They encompass a variety of subcellular structures: chromosomes, cell membrane, mitochondria, axons and dendrites. The early experiments are focused more on showing that subcellular ablation is feasible and the *C. elegans* experiments are aimed at addressing specific neuro-biological problems. We add to this body of work by

investigates the underlying physical processes leading to subcellular disruption and showing explicitly that material ablation occurs on a submicrometer scale. We also use femtosecond laser nanosurgery to study stress fiber dynamics and cell mechanics with a specificity and resolution not previously achievable.

3.2.2 Photodisruption of tissues

Femtosecond laser ablation can be applied to larger scale systems such as whole tissues, rather than a single cell or subcellular organelle. While, we are primarily concerned with single cell nanosurgery, an overview of femtosecond disruption in tissue adds to overall motivation for our work and points to some of the potentials future development. The femtosecond laser operates in the energy regime of photodisruption, where the plasma formation, together with the shockwave propagation and cavitation bubble generation are responsible for the material disruption. In this way, it is possible to ablate tissue at the surface or disrupt it in its bulk. Still, the unprecedented precision of the femtosecond laser ablation supersedes than of other laser-based or mechanical tools.

One of the applications that utilizes the versatility of femtosecond lasers is an all-optical histology. Tsai *et al.* showed that by combining two-photon microscopy and surface laser ablation they are able to create a three-dimensional map of mouse cortical tissue [15]. This is a two step process: in the first step the specimen is labeled and a thin slice is imaged through multi-photon microscopy; in the second step, the imaged section is ablated and removed, and the process is repeated. Figure 3.10 shows the vasculature of fixed neocortex of a fluorescent transgenic mouse obtained through four imaging-ablation iterations. Each iteration creates a 200 μm thick stack and the images from four slices are combined to generate a three-dimensional reconstruction of the tortuous vascular architecture of the neocortex, Figure 3.10e. This technique allows for large sections of tissues

to be reconstructed. It has an important advantage over typical pathological methods in using fresh, rather than frozen tissue. The laser ablation also has higher precision than mechanical knives and induces smaller additional damage to the tissue during slicing.

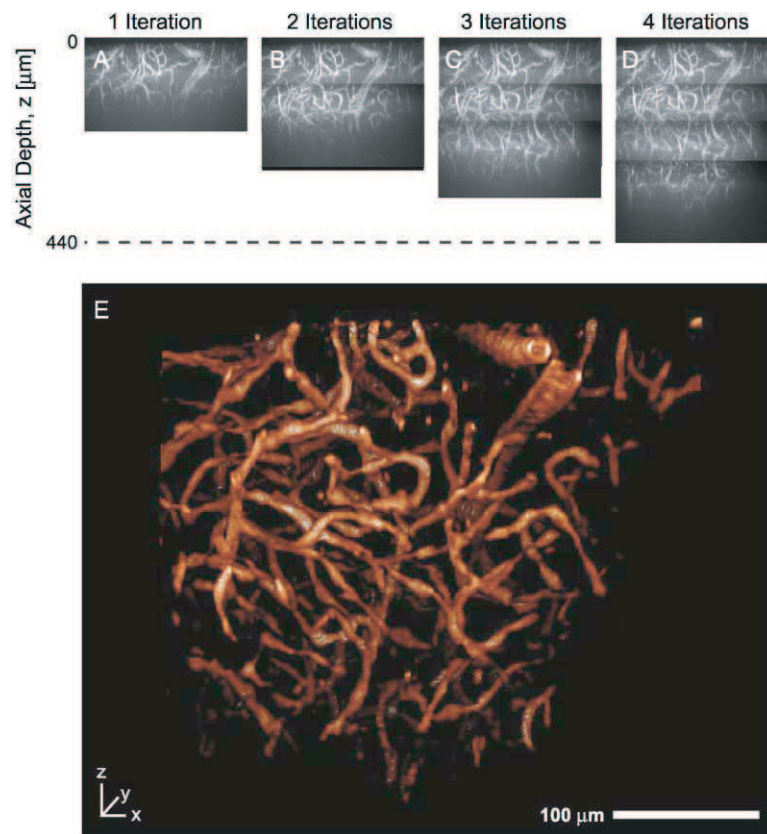


Figure 3.10: Optical cutting, optical sectioning and volumetric reconstruction of labeled vasculature in mouse neortical tissue [15]

Another application of femtosecond laser pulses is in imaging blood flow through cortical blood vessels and developing a model for stroke by disrupting subsurface blood vessels in living animals [16]. Figure 3.11b, c shows optically created three-dimensional reconstruction of vasculature in the cortex of a living mouse. The vasculature was imaged and the blood flow rate was quantified through two-photon microscopy. High-fluence, femtosecond laser pulses are focused on a blood vessel and the laser parameters are varied in order to achieve three different forms of vascular insult Figure 3.11d. First, vessel rupture is induced at the highest optical energies, which provides a model hemorrhage. Second, extravasation (blood vessel leakage) of blood components is possible to focusing low energy pulses, while still maintaining blood flow through through the vessel. And last, a blood clot can be formed by further irradiation of the extravasated blood vessel. The blood flow through the downstream vessels is imaged in real time before and after the induced infraction. The speed of flow drops significantly after the stroke is induced. This demonstrates that blockage of a single microvessel can lead to local cortical ischemia.

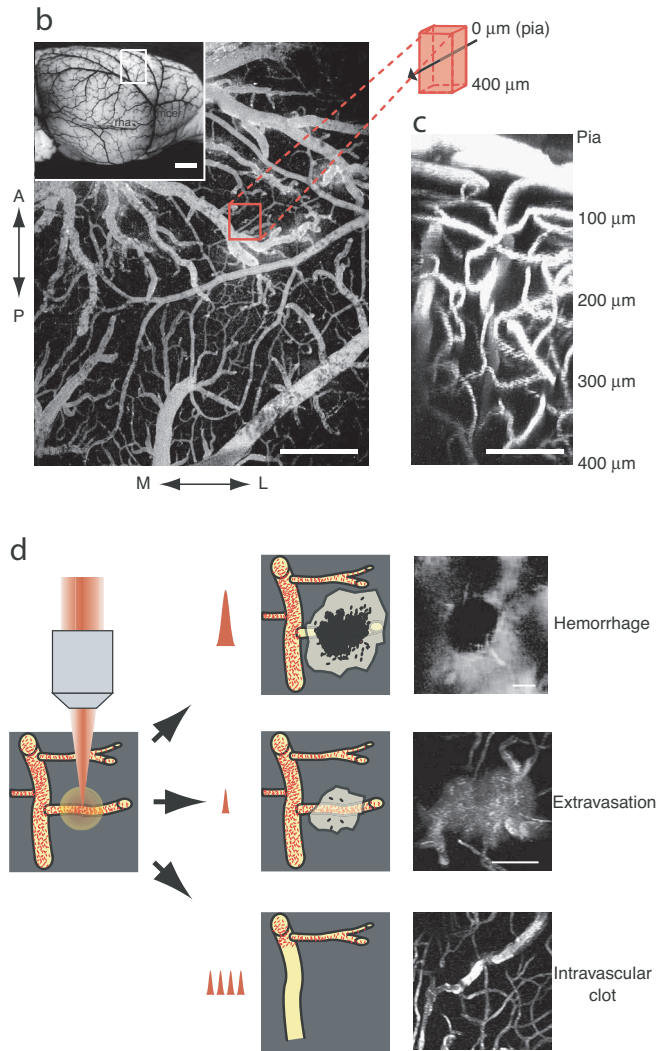


Figure 3.11: (b,c) Maps of fluorescein-dextran-labeled vasculature of rat parietal cortex. Inset in (b) shows latex-filled surface arteries and arterioles in rat cortex, and the white rectangle indicated the approximate location of the craniotomy. The images in (b) are maximal projections along the optical axis of near-surface vasculature. Scale bars: (b) 500 μm (inset 5 mm) (c) 100 μm . (d) schematic of the three different vascular lesions that are produced by varying the energy and number of laser pulses. At high energies, photodisruption produces hemorrhages, in which the target is ruptured, blood invades the brain tissue, and a mass of RBCs form a hemorrhagic core. At low energies the target vessel remains intact, but transiently leaks blood plasma and RBCs forming and extravasation. Multiple pulses at low energy leads to thrombosis that can completely occlude the target vessel, forming an intravascular clot. Scale bar, 50 μm . Adapted from [16]

Laser eye surgery is currently the only wide commercial application of femtosecond lasers. In a LASIK operation, the refractive power of the eye is adjusted by ablating and reshaping the cornea. Traditionally, a mechanical knife is used to create a flap of tissue which is lifted and the cornea is then ablated and the flap is resealed. It is possible to use femtosecond laser photodisruption to create a flap, which is more reproducible and has fewer complications such as whole-flap separation during the preparation. Additionally, histological evidence shows that wound healing reaction is minimal in the flaps created through femtosecond laser ablation [17]. The next level of incorporation of femtosecond lasers in refractive surgery, would be to perform the whole surgical procedure opening of the flap and changing the refractive power by cutting out a lenticule. Figure 3.12 is an SEM image of an eye with a flap and a lenticule cut out using femtosecond laser pulses. When the lenticule is removed and the flap closed the refractive power of the eye is changed. A zoom in on the laser ablated surface shows that there is very little surface roughness created through the laser ablation process.

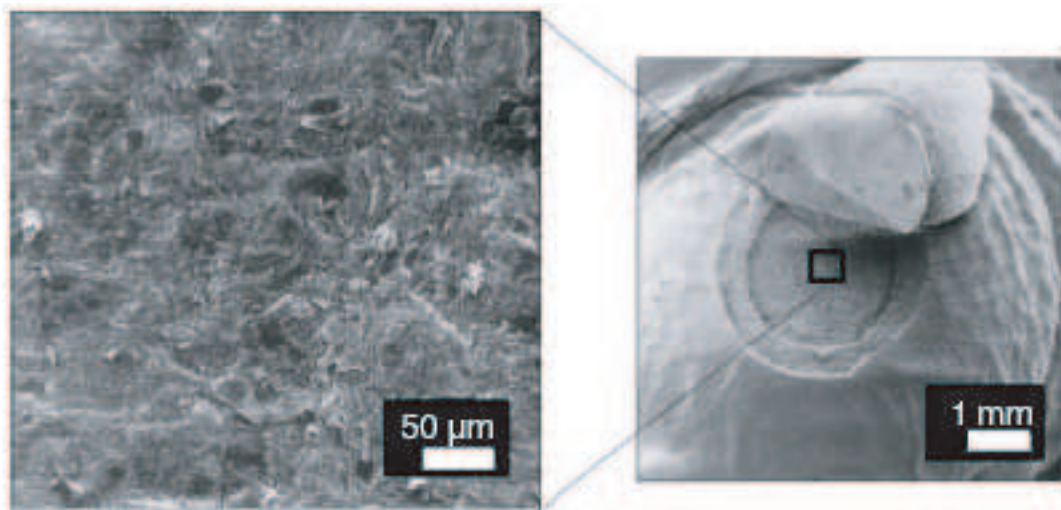


Figure 3.12: Scanning electron micrograph of a corneal flap and an intrastromal lenticule cut out with femtosecond laser pulses. [17]

3.2.3 Conclusion

The list of applications for femtosecond laser photodisruption is increasing rapidly. A sampling of the more prominent applications are mentioned here and there are many others currently being developed. New companies are emerging that offer an all-femtosecond laser based tool for pathological sectioning (Rowiak) or for refractive eye surgery (Intralase, Ziemer Ophthalmic Systems). There are other projects underway, such as applying selective intra-lens ablation to change the accommodation of the eye as a way to correct for presbyopia.

Femtosecond laser nanosurgery on the cellular and subcellular level and tissue photodisruption is a fairly new field that is rapidly expanding. Historically other laser systems, such as picosecond, nanosecond and UV lasers, have been also used for subcellular disruption [51–53]. Due to the shorter wavelengths (smaller penetration depth) and longer pulse duration, the disruption these lasers create is limited to surfaces or thin samples, such as a single cell. The advantage of femtosecond lasers is that by varying the laser repetition rate, pulse energy, number of pulses irradiated and the focusing conditions we can access different interactions regimes and work both on the subcellular and the tissue level with unprecedented precision and accuracy. Combining the laser ablation with nonlinear imaging, as was presented in some of the experiments mentioned above, further increases the utility of this technique.

Chapter 4

Experimental Setup

To image cells and study subcellular processes with submicrometer resolution and in real time, we constructed two systems: a fluorescence and a multiphoton microscope with an integrated femtosecond laser. The experimental setups used are described in this chapter.

4.1 Femtosecond laser systems

Femtosecond lasers generate a pulse train of short, subpicosecond pulses. A comprehensive review of the mechanism of pulse generation and the design of femtosecond laser systems is presented by Brabec and Krausz [54]. The average laser output power is relatively low, about 1 W, and due to the short pulse duration, the peak power can be tens of gigawatts. The high peak power at low pulse energy is what makes subcellular nanosurgery possible. For subcellular nanosurgery we require energies of a few nanojoules at the sample. Femtosecond laser oscillators with energy per pulse this high are only very recently commercially available. Therefore, we used an amplified system, that has more than microjoule per pulse output energy which we reduced to the nanojoule range. To this end, we used

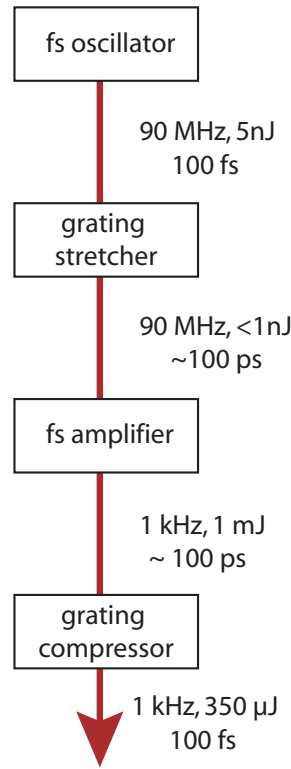


Figure 4.1: A schematic diagram of the stages of an amplified femtosecond laser system with corresponding repetition rate, pulse duration and pulse energy.

two different systems: a home-built and a commercial regenerative amplifier.

Femtosecond laser systems, typically have two stages: an oscillator and an amplifier. A schematic of the pulse propagation through the different stages is shown in Figure 4.1. The first laser system we used is a home-built regeneratively amplified system. The oscillator generates a pulse train at 90 MHz with a single pulse energy of 3-5 nJ and 100 fs duration. The pulse energy is increased via regenerative amplification [55]. In this scheme, a pulse coming from the oscillator is selected and the pulse duration is increased by passing the pulse through a “grating stretcher” to tens of picoseconds. This allows the pulse to gain energy while keeping the peak energy and intensity low. The pulse is injected into the amplifying stage. It circulates for about 20 roundtrips through the amplifier cavity, gaining

energy and is then ejected. The output pulse is recompressed using a “grating compressor” back to 100 fs. The repetition rate of the laser decreases to ≈ 1 kHz and while the energy per pulse increases to ≈ 350 μ J.

A second laser system that we used is made by Coherent and has a Mira oscillator and RegA regenerative amplifier. The principle of operation is as described above, though the laser parameters vary slightly. The Mira puts out a pulse train at 76 MHz with energy per pulse of up to 9-10 nJ. The pulses feed into the RegA amplifier, which has a variable repetition rate of 10-250 kHz and maximum energy per pulse of 6 μ J at 10 kHz and 2.5 μ J at 250 kHz. For subcellular surgery we typically use less than 5 nJ per pulse at the sample and therefore have to greatly attenuate the beam from the amplified laser.

Short pulses stretch as they propagate through dispersive media such as glass. In a typical set up there are a few lenses and a microscope objective at the end which in total have a few centimeters of dispersive material. To ensure that the pulse duration at the focus is the shortest, we move the position of the grating compressor and precompensate for the external dispersion [56, 57].

4.2 Fluorescence microscope

Our work required the construction of our own microscope, because the integration of an near-IR laser with a commercial microscope is not trivial. Figure 4.2 is a schematic of a custom built inverted fluorescence microscope. The principle of operation is that fluorescence in the sample is excited from a mercury lamp and is imaged onto a CCD¹. The appropriate excitation wavelength for the fluorescence is selected with a filter cube which has excitation and emission bandpass filters. A femtosecond laser beam is integrated with

¹The CCD camera used is a CoolSnap *cf* made by Photometrics. It is a monochrome camera with maximum speed of 10 frames per second at maximum resolution of 1392x1040. It has maximum quantum efficiency of about 50 percent at 480 nm.

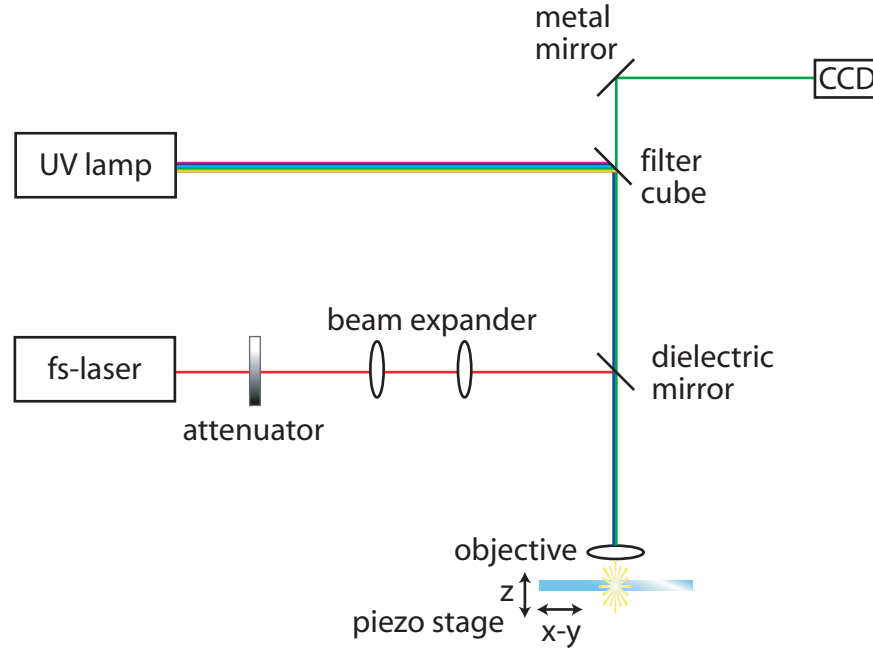


Figure 4.2: This is a schematic setup of the custom built inverted fluorescence microscope

this setup by placing an 800 nm dielectric mirror between the filter cube and the input aperture of the objective lens. This mirror is transparent to the excitation and emission wavelength (typically in the visible, 400-600 nm) and reflective to the laser light. This allows the laser light to be reflected towards the objective while the fluorescence excitation and emission pass freely through this mirror. This is an important degree of freedom of our custom built system, which allows for the simultaneous fluorescence imaging and disruption. The placement of this mirror has the added advantage that it acts as a filter for any laser light that would be scattered back from the sample back to the CCD. The CCD is connected to a computer for image download, storage and processing.

The choice of objective lens is key when deciding on the resolution and precision of femtosecond laser nanosurgery. Specifically, the numerical aperture (NA) determines the size of the diffraction limited focal spot. Since the ablation has an intensity dependent

threshold, larger NA means lower pulse energy to achieve disruption. Lower pulse energies also minimize side effects such as cavitation bubbles which can be detrimental in certain situations. All the images presented in this thesis were obtained with a 1.4 NA Plan-apochromat, 63x, infinity corrected, oil immersion objective from Zeiss with transmission of 55% at 800 nm. The working distance of the objective is 180 μm and it is coverslip corrected.

The cells are plated (see experimental methods in Chapters 5 and 7 for procedures) on a glass cover-slip bottom dish with thickness of about 160 μm , which allows us just enough space to image single cells with the 1.4 NA objective lens. If it is necessary to disrupt more than a single point in the sample, we can move the sample with respect to the laser beam using high precision translation stages with piezo actuators (model MDT 630 from Thorlabs). The manual screws have 4 mm translation range and the piezo actuators have a range of 20 μm with 10 nm precision. This allows us sufficient range to examine large samples, and precise enough control to position the desired location in the sample at the submicrometer laser beam focus.

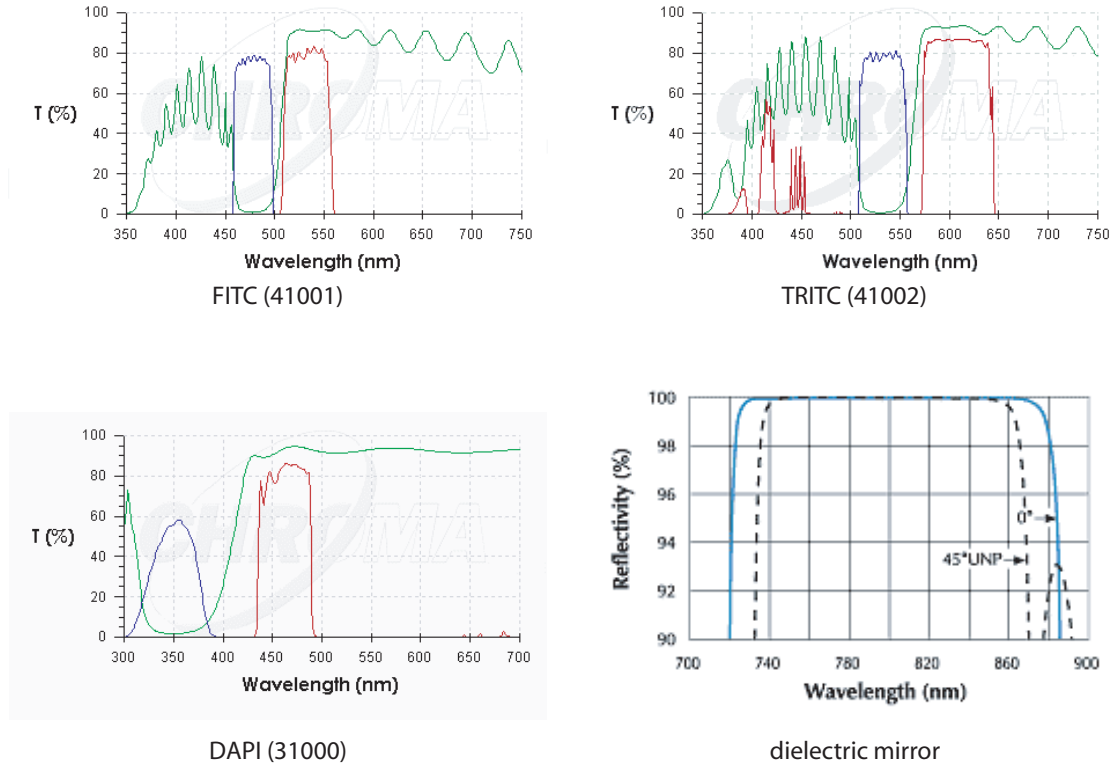


Figure 4.3: Transmission plots for FITC, TRITC and DAPI filter sets from www.chroma.com (blue:exciter, green:dichroic, red:emitter), and a typical laser dielectric mirror from www.cvilaser.com.

The fluorescent labels used and their corresponding absorption/emission peaks in nm are: GFP 488/507 and YFP 513/527, Alexa 488 495/519, fluorescein 490/525, rhodamine 550/573, and DAPI 359/461. The corresponding filter sets, from Chroma (www.chroma.com), are: FITC (set number 41001), TRITC (41002) and DAPI/Hoechst (31000). The spectral characteristics of these filters are plotted in Figure 4.3. Also shown is the reflectivity of a dielectric mirror, showing it is highly reflective only in a narrow range around the laser wavelength.

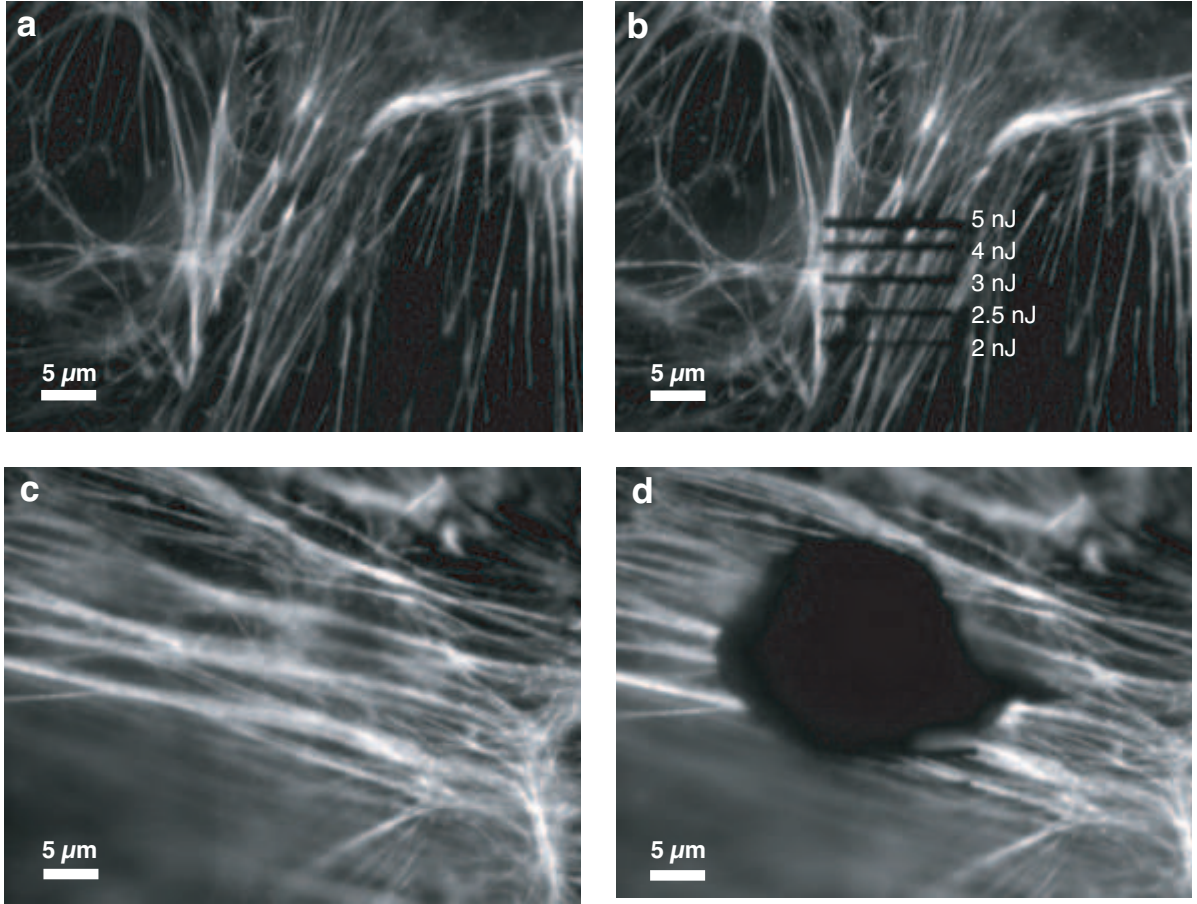


Figure 4.4: Fluorescence images of Alexa 488 labeled actin in an endothelial cell a) before and b) after irradiation along 5 parallel lines with corresponding per pulse energies. c) shows a cell before and d) after irradiation with a 60 nJ pulses and the extent of the damage due to a cavitation bubble.

An example of the imaging and subcellular disruption that we can achieve with this system is presented in Figure 4.4a. It shows a fluorescence image of a fixed endothelial cell stained with Alexa 488 stained actin network, imaged using the setup described above. Only the actin cytoskeleton is visible in the cell. In the image on Figure 4.4a, we irradiated the cell and translated it with respect to the laser beam at approximately $0.7 \mu\text{m/s}$ corresponding roughly to 15,000 pulses per line at a 1 kHz repetition rate. The energy per pulse varies from 5 nJ at the top line down to 2 nJ at the bottom one. The width of the laser affected

area has a marked decrease with the decrease in the energy per pulse.

Figure 4.4c,d shows a pair of images before and after laser irradiation. This time however, there was an error when selecting the laser pulse energy and instead of 5 nJ per pulse we estimate that we irradiated the area with 60 nJ per pulse. We see at this energy the extent of the shock zone and the area disrupted by the cavitation bubble, which is not produced at lower energies. There is a round hole about 20 times larger than the laser focus spot. There is a marked transition from the plasma-induced ablation of the lines shown in Figure 4.4b and the photodisruption due to the cavitation bubble in Figure 4.4d.

Photobleaching of the sample is always an issue when long exposure time and continuous imaging is necessary. With our samples we were able to image anywhere from one to a few minutes before the sample was too photobleached. Realistically, we need to image the sample for two to three minutes, before we can select the area of interest and position it at the laser focus. For cell mechanics studies we observe the cell continuously for at least one minute after laser disruption. In order to get a sufficiently sharp image on the CCD camera we use 500 ms integration time for each snapshot. The chemical dyes such as Alexa, fluorescein and DAPI are more robust to photobleaching than the fluorescent proteins.

Figure 4.5 is an example of some of the live cell work that we have done. It shows a series of images of an endothelial cells that has been transfected with actin YFP. We target an individual filament and disrupt with the femtosecond laser. Then we translate the sample such that the neighboring filament is at the laser focus and we ablate it too. In the live cell sample the width of the laser cut appears to be larger than that in the fixed cell sample in Figure 4.4. This is due to the immediate mechanical response of the cell to the stored prestress in the actin network as discussed in detail in Chapter 7. The last image shows the cell 10 minutes later. What limits the amount of time we can currently do live

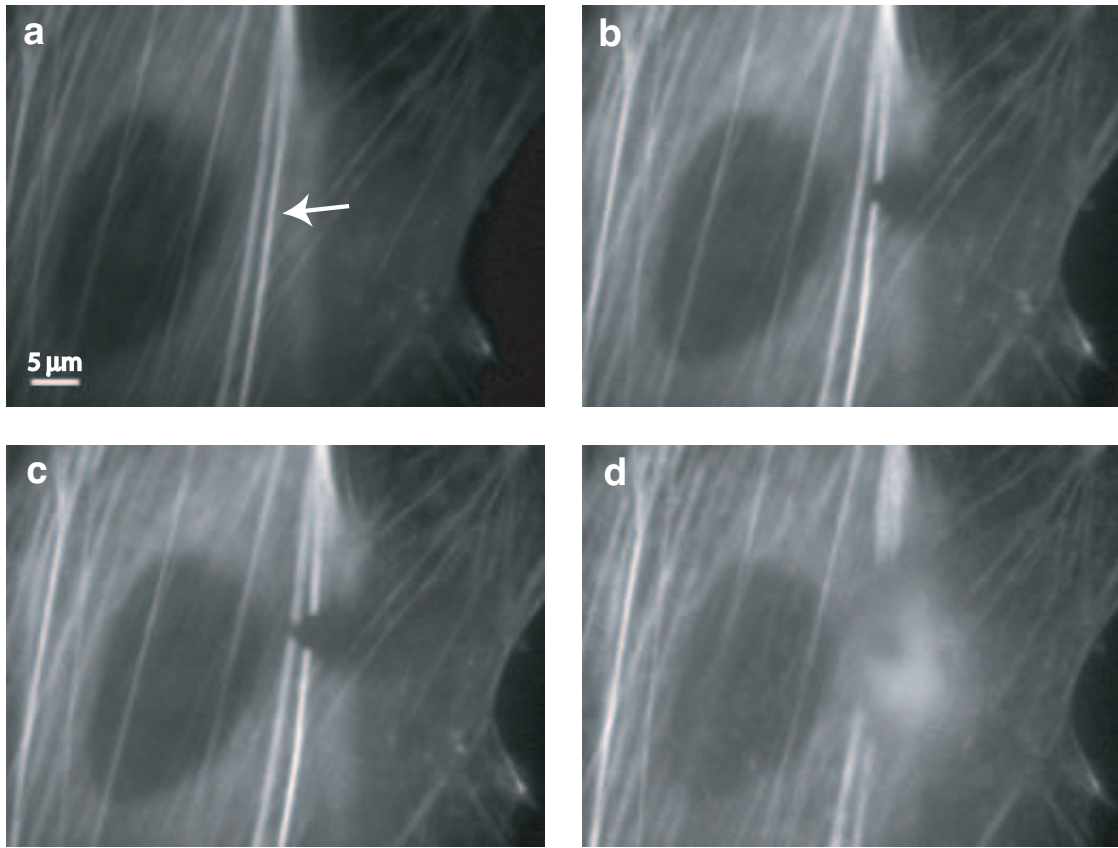


Figure 4.5: Fluorescence images of live endothelial cells transfected with YFP actin: a) before laser irradiation, b) after a single filament was cut, c) a second filament was cut, d) 10 minutes after laser nanosurgery.

cell studies is the temperature and atmosphere control of the sample. Currently, during the experiment the cells are at ambient temperature and in a CO_2 independent media. We have about a 20-30 min window to perform experiment before the cells exhibit signs of death. This time can be prolonged by incorporating an incubator with the setup.

With this system we can image and ablate any fluorescently labeled subcellular structures. In the following chapters we will describe some studies on the size of the ablated subcellular structures (Chapter 5), investigate the dependence of the disruption threshold on the laser repetition rate (Chapter 6) and show how we have used this system to study

subcellular mechanics by disrupting single cytoskeletal filaments and monitoring local and global cell deformation (Chapter 7).

4.3 Custom-built multiphoton microscope

With our home-built fluorescence microscope we can image cells and study subcellular process. However, we are limited to single cell layers, due to the short penetration depth of visible wavenegths, and the observation time is shortened because of weak sample fluorescence and fast photobleaching. To improve on these constraints and still be able to perform subcellular disruption we constructed a multiphoton microscope nanosurgery system. We built an inverted multiphoton microscope that allows us to have the real time imaging and the high spatial resolution necessary for subcellular surgery. The design for the microscope was published by Tsai *et al.* [58]. Specifications on the parts, distance ratios and scanning software are given there. Similarly to the fluorescence microscope, we integrated a stationary high repetition rate laser beam, which allows us to cut and image the same plane in the bulk of a sample.

The design of a multiphoton microscope is a bit more complicated than that of a straight fluorescence microscope. Figure 4.6 shows a schematic of the combined multiphoton imaging and and surgery setup. Part of the output of the Mira laser oscillator is split off and used for imaging, while the rest seeds the RegA amplifier. The advantage of this system is that we can use two independent femtosecond laser beams simultaneously and be able to monitor the laser cutting through the high resolution imaging.

The laser beam from the Mira is focused into the sample to a spot of less than $1\text{ }\mu\text{m}$ diameter. Fluorescence is excited in the focal volume and the emitted light is collected by the PMT. The beam is then scanned across the sample, using a pair of scanning mirrors. The

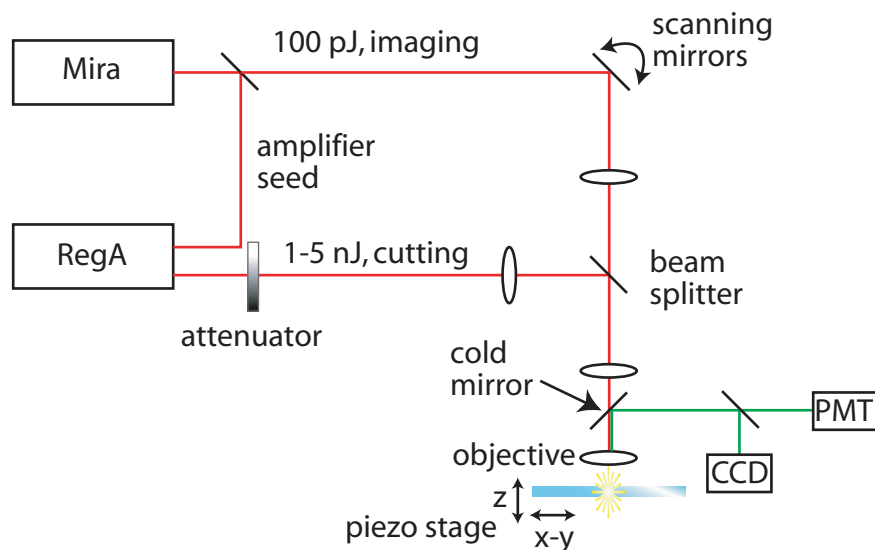


Figure 4.6: Schematic of a combined multiphoton imaging and surgery setup.

signal from the PMT is correlated with the position of the scanning mirror to reconstruct an image. Multiphoton laser scanning microscopy has the advantage that only the focal volume is excited, reducing photobleaching and eliminating out-of-focus fluorescence to increase the background noise. It is also possible to narrow down the scan area only to the spot of interest, thereby increasing imaging times and decreasing overall photobleaching and degradation of the sample.

The Mira laser we used has a fixed wavelength of 800 nm which limits the fluorophores that can be efficiently excited. Unfortunately, fluorescent proteins such as GFP and YFP have two-photon absorption peaks above 900 nm, see Figure 3.2. At the pulse energies (more than one nJ) that we were able to detect the fluorescence with our 800 nm pulses we observed great sample degradation. Due to the excess amount of energy deposited we raised the temperature over 100°C and likely caused cavitation bubbles [26]. Therefore with this laser system, we are limited to using fixed cells and select dyes. An example of the

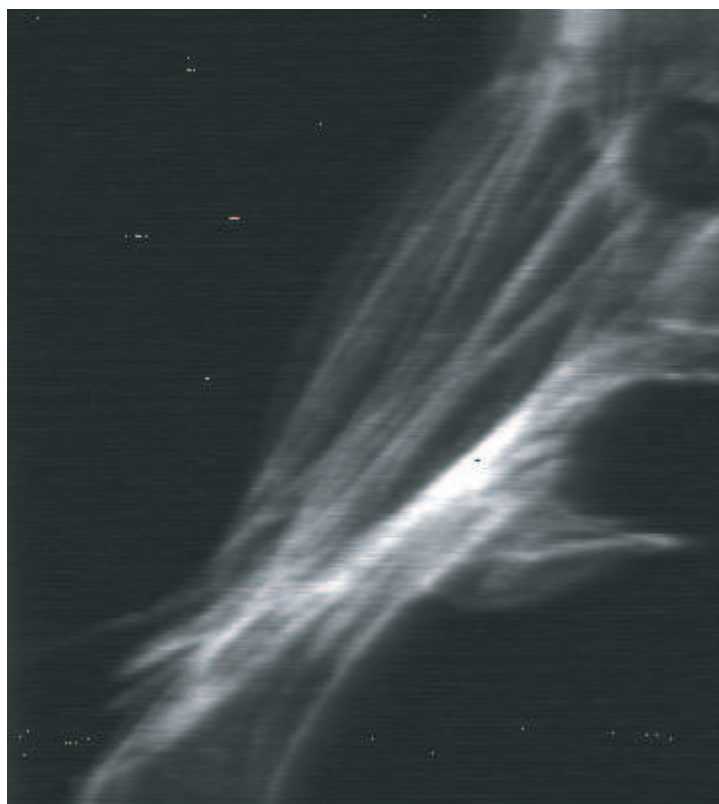


Figure 4.7: Two-photon image taken of Alexa 488 labeled actin in a fixed endothelial cell.

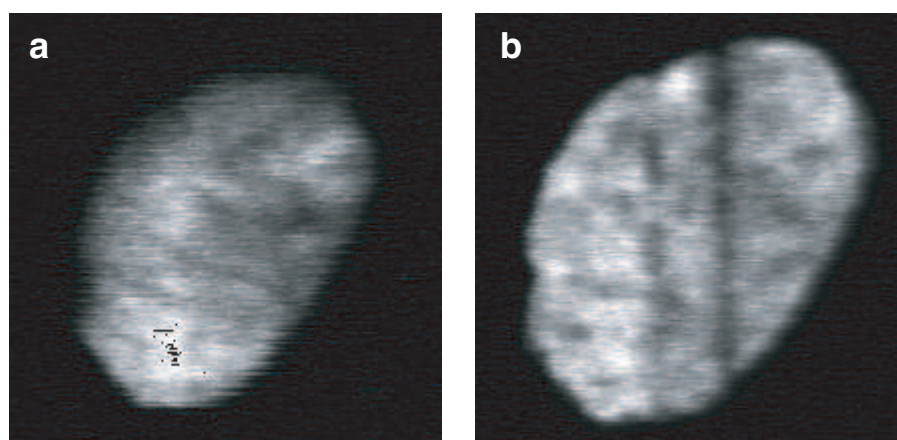


Figure 4.8: Two-photon image taken of DAPI labeled nucleus in a fixed cell a) before and b) after laser surgery.

images that we could achieve are Figures 4.7 and 4.8 which show respectively two-photon excitation images of an Alexa 488 labeled actin network and a DAPI labeled nucleus in fixed endothelial cells. Two lines were dissected through the nucleus by irradiating it with the stationary 10 kHz repetition rate from the RegA and translating the sample with respect to the laser beam.

We are also able to image the native state of a system through autofluorescence. Figure 4.9 is an image of a leaf, picked from a plant outside of our lab. While we do not know the exact molecules that we are exciting, they are likely the chromophores that give some of the natural color to the leaf. The set of nine images show a z-scan through the leaf from bottom to top (a) being deepest and (i) the top most layer. Each imaged layer is spaced by approximately 5 μm . We see changes in the types of cells and structure as the leaf is scanned through.

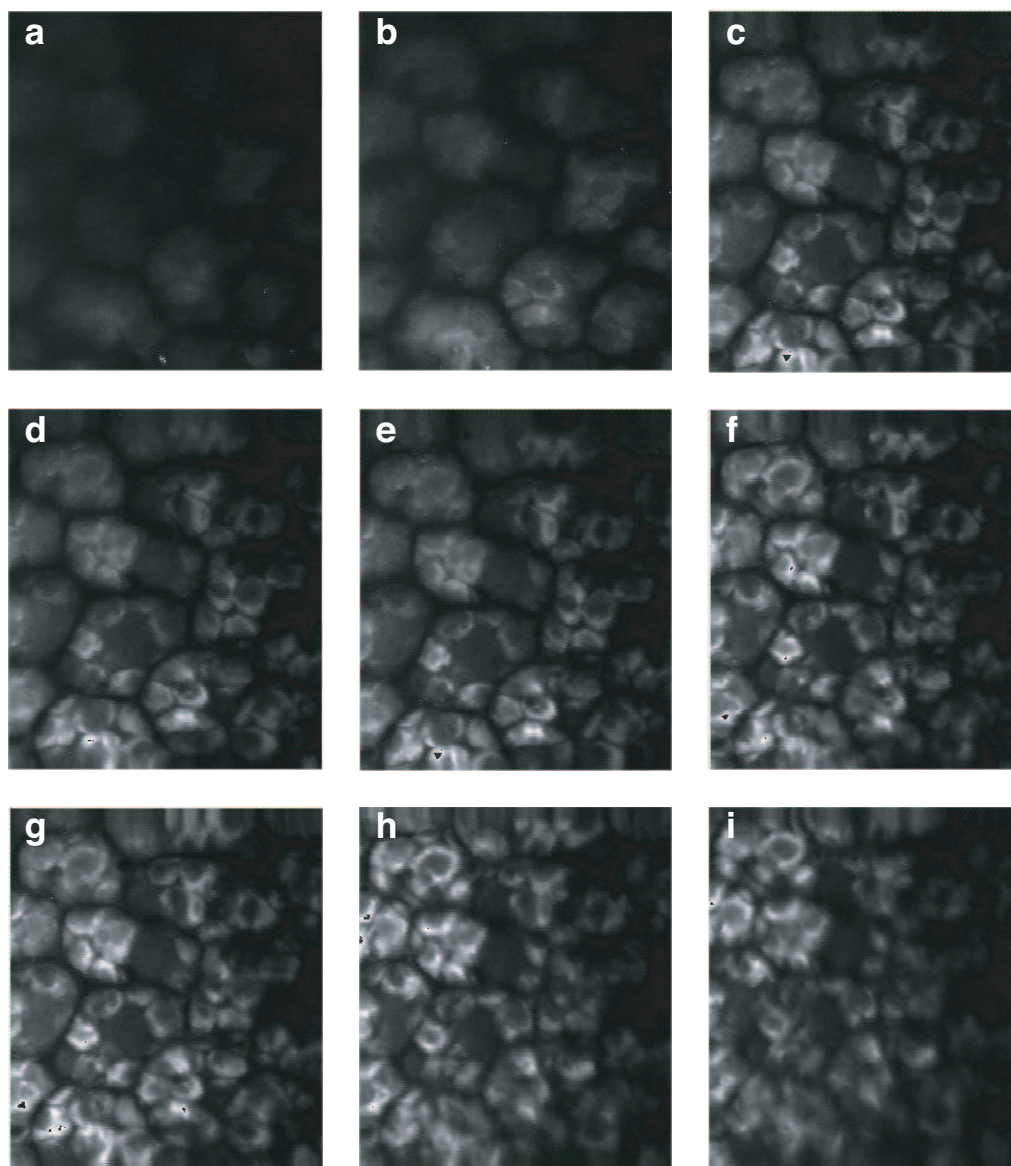


Figure 4.9: Two-photon excitation of autofluorescence in a leaf.

We can also take SHG images of unstained samples. Collagen gels can be imaged via SHG. Figure 4.10 is an image of a collagen gel through second harmonic generation. The collagen was obtained from Vitrogen, pipetted in a coverslip bottom dish and incubated for 30 minutes at 37°C. As it gels it forms a mesh network of single strands which can be identified in this image. The image is a z-projection of 15 different planes taken 1 μm apart. The width of the image is 150 μm .

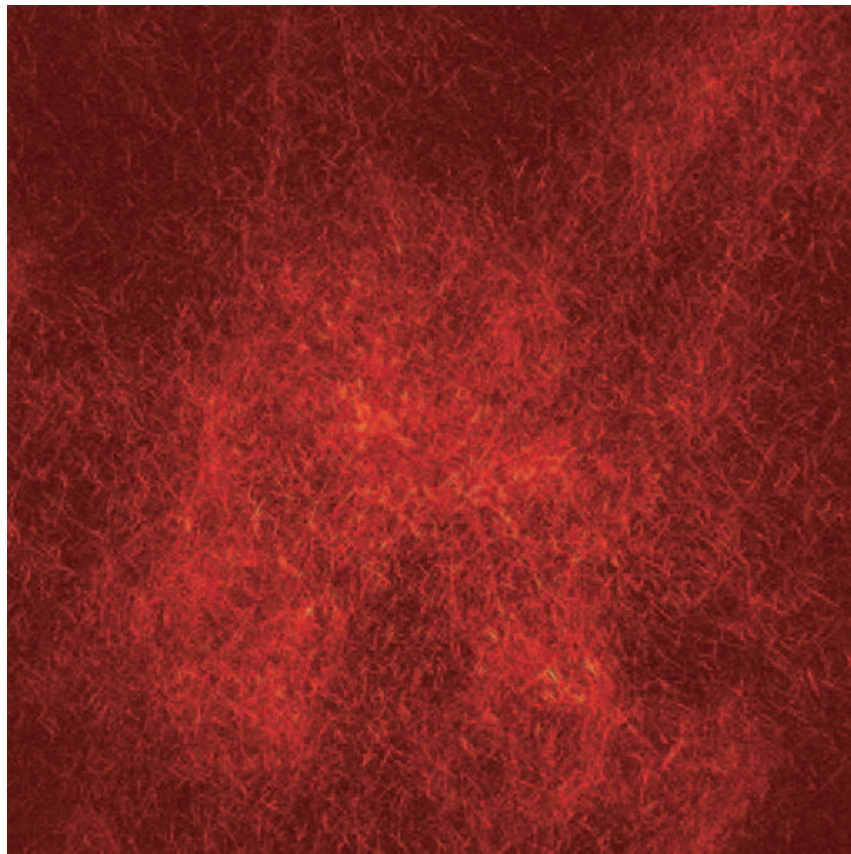


Figure 4.10: Two-photon image taken of DAPI labeled nucleus in a fixed cell.

4.4 Summary

We have built two systems for femtosecond laser nanosurgery. With our fluorescence microscope we image cells and ablate subcellular structures with submicrometer precision. Photobleaching and the incubation conditions currently limit us in the amount of time we can study individual cells, and the penetration depth of visual wavelength restricts us to studying single cell layers. The dual femtosecond laser beam multiphoton microscope nanosurgery system has immense potential in allowing us high resolution imaging, three dimensional sectioning and simultaneous disruption. We have already demonstrated some two-photon, autofluorescence and second-harmonic generation images. The shortcoming of the current configuration of the system is the stationary wavelength of the Mira, which precludes the imaging of most fluorescent proteins and therefore live cell samples.

Chapter 5

Subcellular dissection confirmed by TEM

5.1 Introduction

Femtosecond pulses focused in the bulk of inorganic transparent materials can create structural modification ranging from a local density gradient to void formation in the irradiated area. Comprehensive studies with glasses and soft materials have revealed the extent of photodamage as a function of pulse energy [6]. The material properties of glass make it relatively simple to observe these changes, under a conventional light microscope. At relatively low pulses energies the resulting density gradient in glasses can be visualized as marked changes in the index of refraction, and at higher energies the void formation is observed by cleaving the sample at the plane of the laser focus and imaging the surface with an scanning electron microscope. However, studying the bulk damage incurred in organic matter such as a single cell has not been observed as clearly.

To conclusively show the bulk interaction of femtosecond laser pulses with biolog-

ical materials we studied the effects of femtosecond laser irradiation in fluorescently-labeled structures in the cytoskeleton and the nuclei of fixed cells using a combination of fluorescence microscopy and whole mount TEM. We used fluorescence microscopy to evaluate the extent of apparent photodamage, and TEM to determine the actual degree of material removal. This let us define three regimes of interaction: no interaction, photobleaching with no apparent structural modification and bulk material removal.

5.2 Experimental methods

The laser radiation is generated in a custom-built chirped-pulse amplified titanium-sapphire laser system. A passively mode-locked oscillator delivers 100-fs pulses at a repetition rate of 80 MHz and a central wavelength of 790 nm. These pulses are regeneratively amplified to energies of up to 1 mJ at a repetition rate of 1 kHz. As these energies are far too high for subcellular ablation, we reduce the pulse energy to the nanojoule range with an attenuator. An adjustable neutral density filter wheel is used to regulate the energy at the sample. The laser light is focused into the sample with a 1.4-NA oil-immersion objective (Zeiss, Plan- Apochromat), leading to a theoretical spot size of roughly 340 nm. As the intense laser pulses experience group-velocity dispersion inside the microscope objective, the resulting pulse duration at the sample is approximately 200-250 fs [1]. The sample is placed on a piezocontrolled microscope stage that permits sample positioning with 10-nm precision along all three axes. A UV lamp (Osram, HB103 W/2) illuminates the sample and the emitted fluorescence is collected through the objective using a standard filter cube (FITC, Chroma Technology Corp.) and recorded with a CCD camera.

Bovine capillary endothelial cells (passage 10 to 15) were maintained at 37°C in 10 % CO₂ on tissue culture dishes in a complete medium composed of low-glucose

Dulbeccos modified Eagles medium (DMEM; Gibco-BRL) supplemented with 1% fetal calf serum (FCS) (Hyclone), 10 mM HEPES (JRH-Biosciences), and glutamine (0.292 mg/ml)/penicillin (100 U/ml)/streptomycin (100 g/ml) as previously described [59].

For the live cell experiments, cells were transfected for 48 h with an adenoviral vector system [60, 61] encoding enhanced green fluorescent protein (EGFP)-tagged G-tubulin, trypsinized (TrypsinEDTA, Gibco), harvested, and seeded onto glass-bottomed 35 mm dishes (MatTek) in complete medium. Prior to imaging, cells were transferred into a nonfluorescent, CO₂-independent medium (pH 7.3) containing (in mM): CaCl₂ (1.26), MgSO₄ (0.81), KCl (5.36), KH₂PO₄ (0.44), NaCl (137), Na₂HPO₄ (0.34), D-glucose (5.55), L-glutamine (2.0), sodium pyruvate (1.0), HEPES (20.0), 1% bovine serum albumin, 10% calf serum, and MEM essential and nonessential amino acids (Sigma) [62].

For the fixed cell experiments, cells were then trypsinized (Trypsin EDTA, Gibco), harvested, and seeded either onto glass-bottomed 35 mm dishes (MatTek) or onto carbon-coated formvar on Embra TEM finder grids (Electron Microscopy Sciences) in complete medium. After allowing the cells to attach and spread for 12-24 hours, the cells were fixed in 4% formaldehyde (electron microscopy grade) in phosphate buffered saline (PBS) for 40 minutes, permeabilized in 0.1% Triton X-100 in PBS for 5 minutes, blocked in 1% bovine serum albumin in PBS for 1 hour, and stained for either actin (Alexa Fluor488 phalloidin, Molecular Probes) or nuclear DNA (Hoechst 33348, Molecular Probes), all at room temperature. Afterwards the cells were stored and treated in an aqueous solution (PBS). Following laser treatment, cells were fixed in 2.5% glutaraldehyde in 0.1 M cacodylate buffer, pH 7.4, at 4°C for one hour and then washed and stored in this buffer at 4 C until processing. Prior to TEM imaging with a Philips CM-10 microscope, cells were fixed in 1% osmium tetroxide in 0.1 M cacodylate buffer, pH 7.4, at 4 C for 30 minutes, washed in the same buffer, dehydrated in graded ethanol solutions, critical point dried, and carbon coated. The

TEM analysis gives a direct measure of the ablated area, as the electrons are sensitive to the amount of material they travel through. The ablated region appears lighter on the film, even if it is confined in the bulk of the sample. We took pictures of the cell samples at two different angles creating a stereoscopic image and then we measured the width of the ablated region averaging over three positions along the laser cut.

5.3 Results

Figure 5.1 shows the fluorescence from the actin network of a fixed endothelial cell after it has been irradiated along five parallel lines with various pulse energies. The sample was translated once per line at a speed of approximately 0.7 m/s corresponding to roughly 15,000 pulses per line. Figure 5.1(b) shows that the fluorescence intensity following irradiation depends strongly on pulse energy. At 1.8 nJ the effect of irradiation is barely visible in the fluorescence image. Increasing the pulse energy to 2.2 nJ produces a clear dip in fluorescence with a width of 240 nm at FWHM. At higher energy the FWHM-width of the dip in fluorescence scales with pulse energy, from 360 nm at 2.8 nJ, to 500 nm at 3.5 nJ and 600 nm at 4.4 nJ.

Figure 5.2 shows that loss of fluorescence does not always correspond to removal of material. The figure shows both fluorescence and TEM images of the nucleus of the same fixed endothelial cell after irradiation at three different energies. While a slight loss of fluorescence can be observed for a pulse energy of 1.45 nJ, the TEM image shows no material removal. The loss of fluorescence must thus be due to photobleaching. At higher energies we see clear cuts in both images.

Figure 5.3a shows the dissection width of the cuts observed in Figure 5.2. The data allow us to define three regimes of irradiation: no interaction (no damage visible in

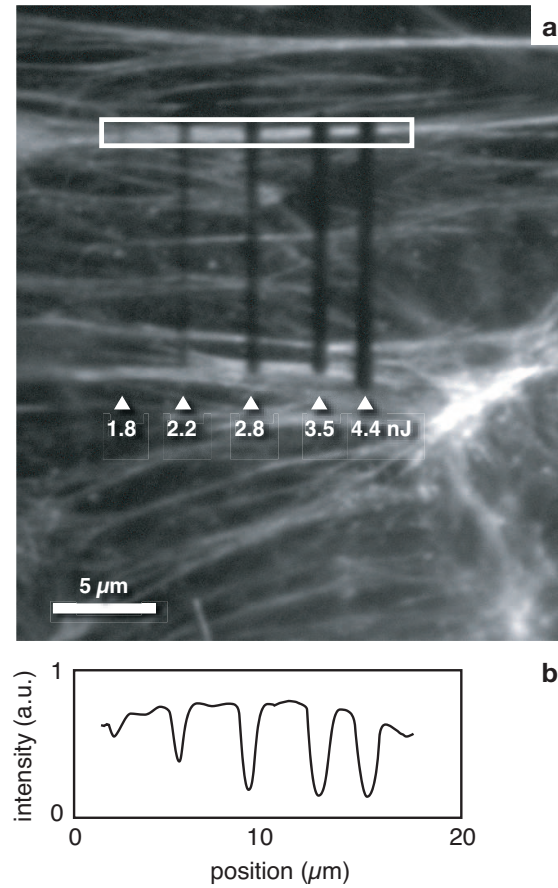


Figure 5.1: (a) Cuts through fluorescently-labeled actin fibers in a fixed endothelial cell obtained by irradiation with femtosecond laser pulses of energies between 1.8 nJ and 4.4 nJ. (b) Fluorescence intensity profile along the actin bundle outlines in the image.

either image), photobleaching without material loss (only the fluorescence image shows a change), and removal of material (both images show cuts). Figure 5.3b and 5.3c show similar data obtained in the nuclei of two other cells. In each case, irradiation at pulse energies below 1 nJ causes no change in either image, while energies above 1.7 nJ do cause changes in both images. Thus, the threshold energy for plasma-mediated ablation falls between 1-1.7 nJ. For pulse energies above 1015 nJ, a much larger part of the cell is ablated (not shown). This phenomenon is most likely due to cavitation, which has been observed during laser irradiation of water, soft materials, and biological tissues [63,64]. Part of the

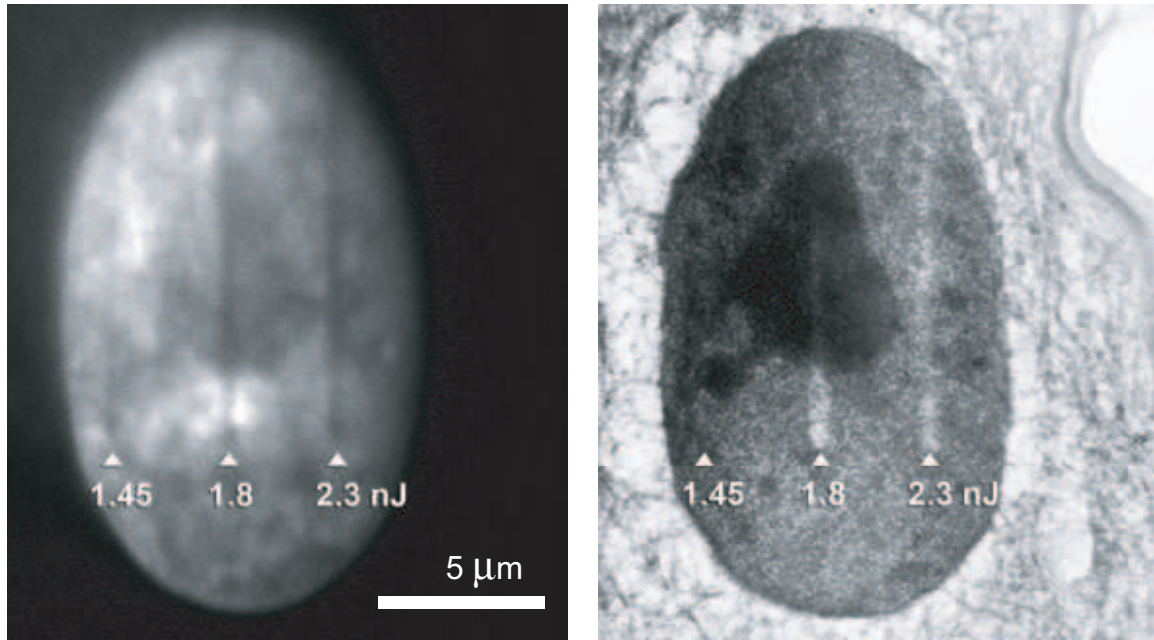


Figure 5.2: Cuts in the nucleus of a fixed endothelial cell at various laser energies, imaged by (a) fluorescence microscopy and (b) electron microscopy.

energy delivered to the sample cannot be dissipated through thermal diffusion, producing a rapid, local increase in material temperature, leading to an explosive expansion of the material and, thus, damage far from the laser focus.

While the thresholds in Figure 5.3 vary from sample to sample, the energy threshold of ablation is at most 20% higher than the photobleaching threshold. In other words, at energies exceeding 1.2 times the threshold for which fluorescence disappears, one can be assured of material removal. The TEM and fluorescence microscopy measurements reveal that the plasma-mediated ablation width depends strongly on pulse energy, with pulse energies between 1.2 and 1.7 nJ producing material loss as small as 200 nm (Figures 5.3a and 5.3c). Above 1.7 nJ, the dissection width increases with energy; around 3 nJ the width is approximately one micrometer. At higher pulse energies, the dissection widths obtained from the TEM images are consistently larger than those obtained from the fluorescence

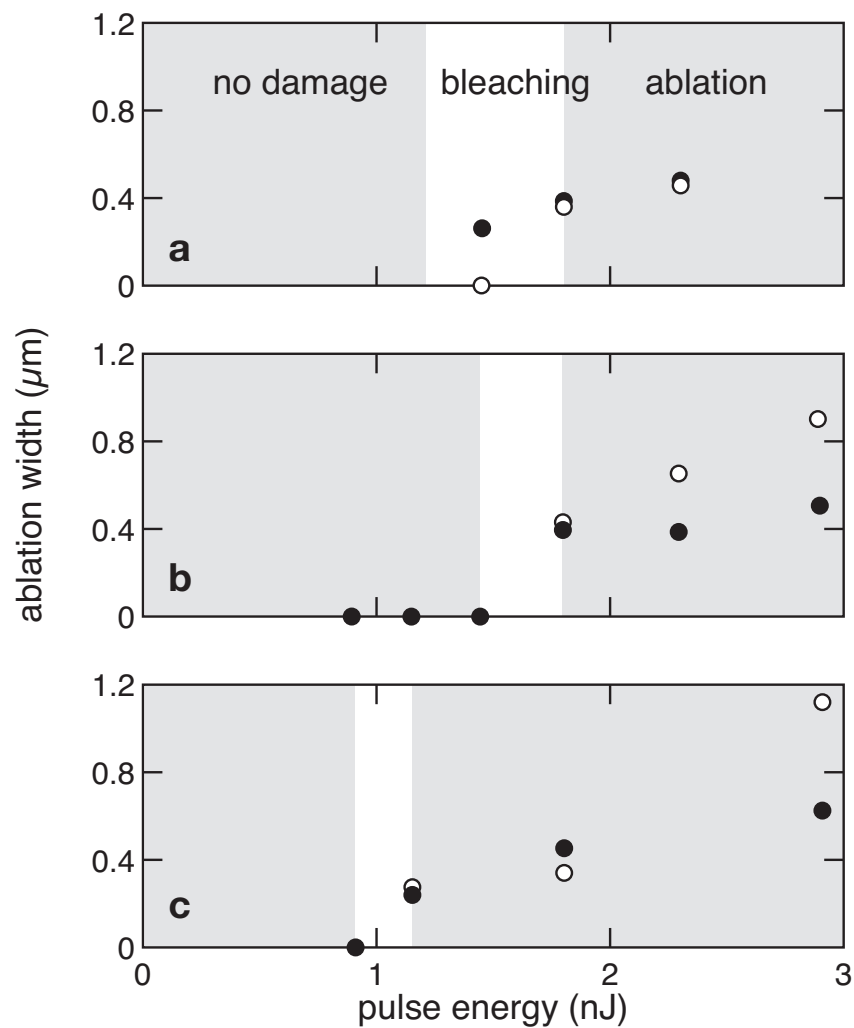


Figure 5.3: Pulse energy dependence of the ablation width of cuts in the nucleus of endothelial cells measured by fluorescence microscopy (filled circles) and TEM (open circles) in three different cells a-c.

images. This discrepancy is likely due to the TEM sample processing. Post-fixation, dehydration and critical point drying have all been shown to cause shrinkage in cellular contents while maintaining the usual structural relationship of components within the cell [65, 66]. This shrinkage can result in a retraction of cellular material away from the ablated area, thus enlarging the ablation zone in the cells subsequently viewed by TEM. The TEM data in Figure 5.3 therefore likely overestimate the extent of laser induced material removal.

To show the spatial selectivity of femtosecond laser nanosurgery in cells we targeted microtubules in live cells. The microtubule network is sensitive to external disruptions and can be used as good indicator for the extent of damage induced by the laser irradiation outside the focal volume. Figure 5.4 is a fluorescence microscope image of a live bovine endothelial cell whose microtubules express green fluorescent protein. The dark region in the middle of the cell is the nucleus. We severed a bent region of a single microtubule located above the nucleus using about 1000 laser pulses with an energy of 1.5 nJ. The curved end of the microtubule immediately recoiled to a straight configuration within the first 2 s after laser ablation, indicating the release of stored elastic energy in the molecular filament; this was immediately followed by depolymerization of the cut ends of microtubule due to release of tubulin monomers, as shown in time-lapse frames in Figure 5.4b. The neighboring microtubules, which are less than 1 μm away, remain undisturbed. Even though it is impossible to get a measure of the exact size of the laser dissection in this type of live cell experiment, the narrow confinement of plasma-mediated laser ablation confirms the TEM data obtained for fixed cells.

5.4 Conclusion

The use of ultrashort laser pulses for dissecting and imaging cells and subcellular structures in cellular and developmental biology is increasing rapidly. In this report we presented a first systematic study of the relationship between pulse energy and subcellular material loss using femtosecond laser pulses. We used a combination of fluorescence and electron microscopy to establish the thresholds for fluorescence photobleaching and material removal under tight focusing conditions. The results presented here show that there is a range of energy for which photobleaching occurs without ablation. We find that the optimal

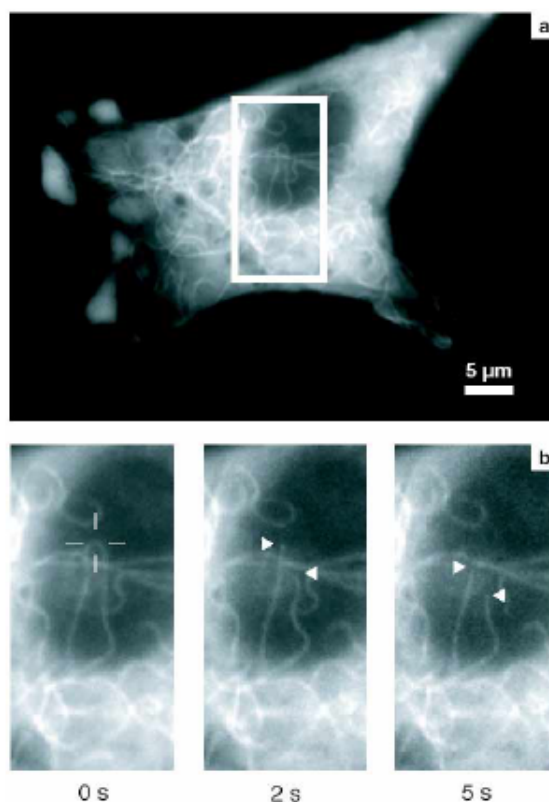


Figure 5.4: (a) Fluorescence microscope image of GFP-labeled microtubule network in an endothelial cell. (b) time-lapse sequence showing rapid retraction of microtubule due to depolymerization. The cross hair shows the position targeted by the laser; the triangles show the retracting ends of the microtubule.

energy range for plasmamediated ablation is from about 20% above the photobleaching threshold to about 3 nJ. In this range, one is assured of dissection with a resolution as small as 200 nm. At higher energies the size of the dissected region increases rapidly with laser pulse energy. We also demonstrated that this technique can be successfully applied to live cells with high spatial resolution. These results will help guide and interpret femtosecond laser material removal and real time fluorescence imaging to investigate cell structure and function at increasingly small length scales.

Chapter 6

Dependence of the subcellular disruption threshold on the laser repetition rate

In the previous chapter we showed that femtosecond laser pulses disrupt subcellular structures with just a few nanojoules of energy per pulse. In recent years, femtosecond laser technology has improved rapidly, and currently there are commercial laser sources that work at high repetition rates, are tunable and have output energies per pulse of tens of nanojoules. Such a laser system should be sufficient for subcellular nanosurgery. The critical difference between such a laser system and the system used for the ablation studies in the previous chapter is in the repetition rate: MHz vs. kHz. In section 2.6 we showed that the morphologies of structures created in glass differ significantly at the two repetition rates due to the cumulative vs. single shot interaction mechanism. We would therefore expect such a difference to exist in the subcellular-disruption threshold.

To determine the dependence of the ablation threshold on the pulse energy and

irradiation time, we studied the ablation of actin stress fibers in living endothelial cells. The motivation for using endothelial cells is that they build a strong actin network, which is excellent for the laser ablation threshold studies. There is a distinct transition that occurs when an actin fiber has been disrupted: it retracts due to the tensile load on the fiber and thus the ends pull apart much further than the size of the laser interaction volume (Chapter 7) [19]. Therefore, there is no need to resort to electron microscopy to see the onset of disruption.

6.1 kHz laser repetition rate

For a laser repetition rate in the kHz regime the energy of a single pulse defines the plasma-ablation threshold. If the energy is very low, less than 0.5 nJ per pulse for 1.4 NA focusing, there is no interaction with the material. Figure 6.1 shows a fluorescence image of an endothelial cells transfected with YFP actin. We irradiated the filament at the location indicated by the arrow with a 14 kHz pulse train of 0.5 nJ pulse for 3 s. There is a slight loss of fluorescence at the irradiated site, but the fiber was not disrupted.

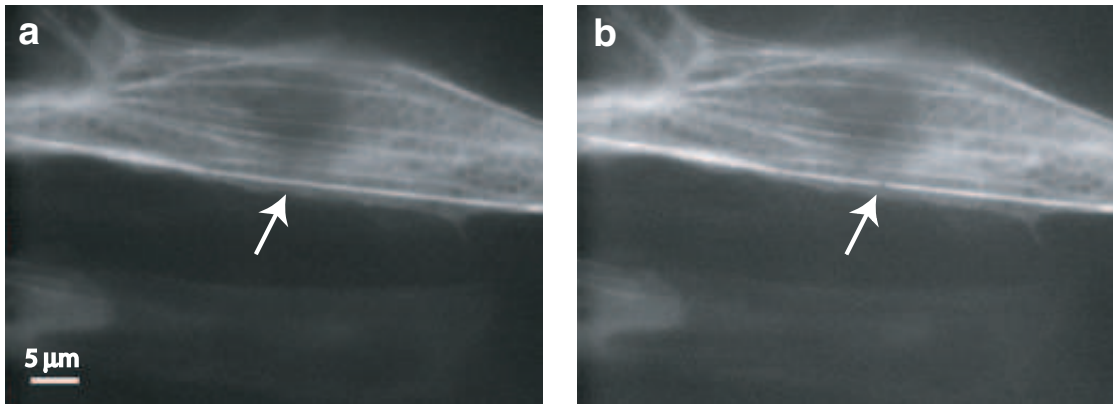


Figure 6.1: An actin filament in an endothelial cell irradiated with 14 kHz, 0.5 nJ for 3 s is not disrupted.

At higher pulse energies at a kHz repetition rate, we observe plasma-induced ablation, which results in a severed the actin filament. Figure 6.2 shows before and after images of a cut filament. The energy per pulse is 1 nJ at the focus and the irradiation time is 3 s. We expect that the minimum number of pulses necessary to sever a filament will depend on the size and thickness of the filament. Even though we have not extensively studied the minimum irradiation time, there seems to be no apparent detrimental effect on the cell due to prolonged exposure with a kHz femtosecond laser pulse train.

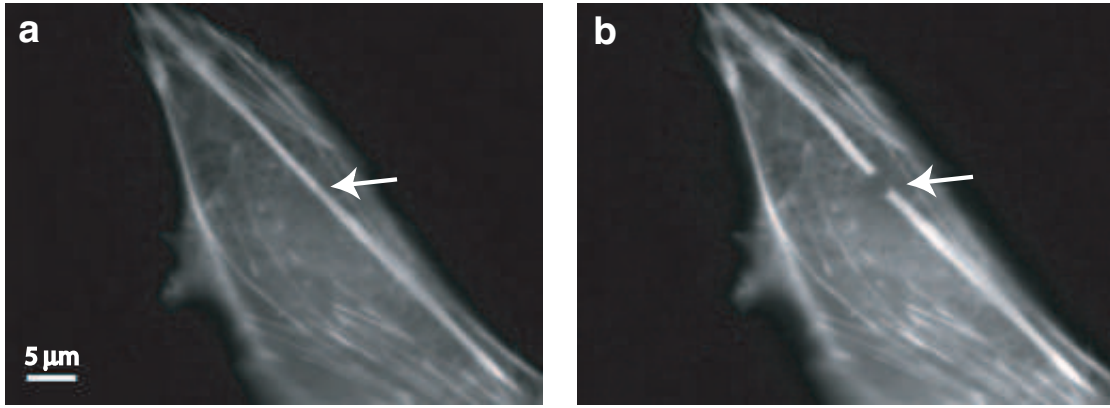


Figure 6.2: An actin filament in an endothelial cell irradiated with 14 kHz, 1 nJ for 3 s is severed.

6.2 MHz laser repetition rate

MHz femtosecond laser disruption is fundamentally different from disruption with kHz pulse trains [5, 29]. The heat diffusion time out of the focal volume is typically about 1 μ s corresponding to a repetition rate of 1 MHz. This implies that for repetition rates lower than that, the heat diffuses out of the focal volume before the next laser pulse arrives and there is not additional heating. While for repetition rates higher than 1 MHz, there is an accumulated heating effect due to the residual heat left in the focal volume from each

preceding pulse. While it is extremely hard to measure directly the temperature increase in the focal volume of $1\ \mu\text{m}^3$, it can be indirectly inferred in glasses, by looking for index changes, which mark the edge of the molten zone, see Figure 2.7. In this way, one can estimate the distance from the focus at which the temperature has reached the melting temperature of the glass.

Pulse energies used for femtosecond laser ablation at kHz repetition rate show a markedly different effect at MHz repetition rates. We determined that with the threshold for kHz ablation is around 1 nJ per pulse and that 3 s of laser irradiation produce a nice clean cut in actin. Applying the same pulse energy and exposure time for a 76 MHz pulse train has a disastrous effect on the cell. Figure 6.3 shows a cell irradiated at these conditions. There is a large cavitation bubble formed which destroys the actin filament and rips through the cell. This is a clear indication that the pulse energy and irradiation time for optimal subcellular disruption need to be optimized for the high repetition rate system.

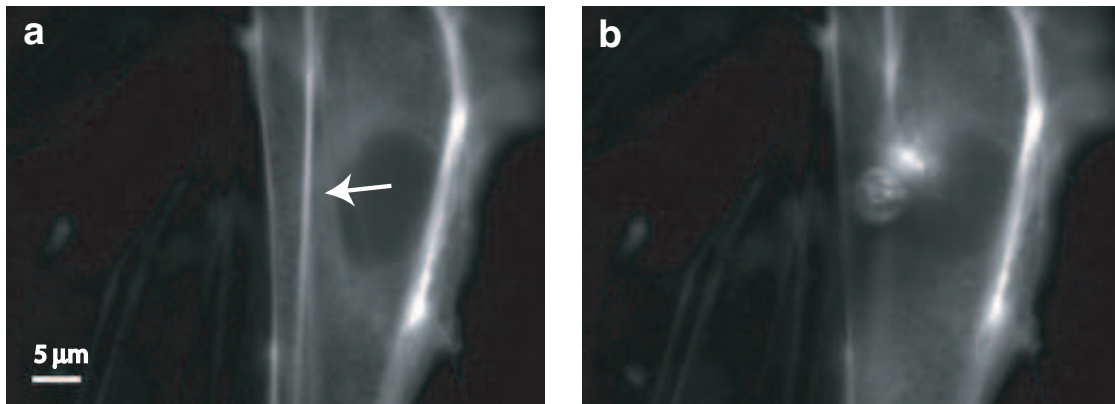


Figure 6.3: A large cavitation bubble is launched in an endothelial cell when irradiated with 76 MHz, 1 nJ for 3 s.

If we lower the pulse energy and shorten the irradiation time we are able to sever actin filaments with MHz pulse trains, without causing obvious distress to the cell. Figure 6.4 shows an actin stress fiber before and after irradiation with 0.5 nJ per pulse for 500 ms

at 76 MHz. This pulse energy is not enough to disrupt a filament at 10 kHz (Figure 6.1) but produces clear disruption at this high repetition rate.

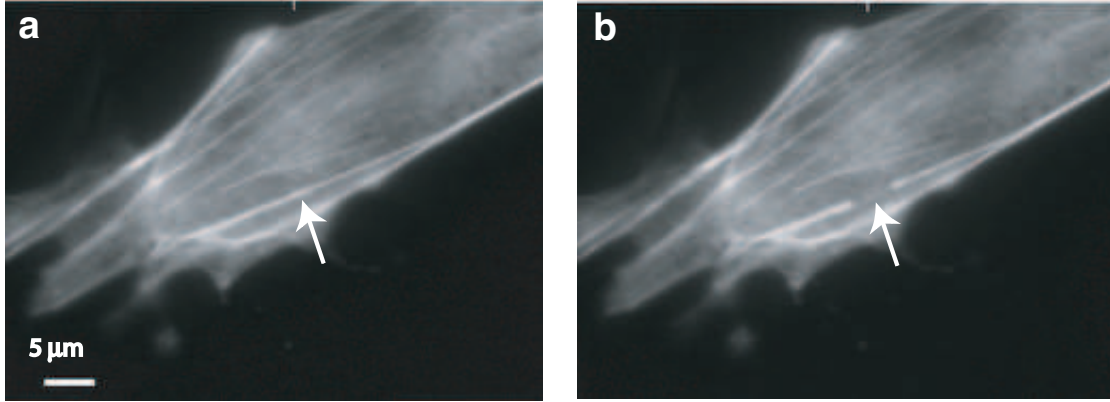


Figure 6.4: 0.5 nJ at 500 ms.

We measured the threshold for actin cutting as a function of the irradiation time, Figure 6.5. As the pulse energy increases, shorter irradiation time is necessary to achieve actin disruption. We are limited by the apparatus to irradiation durations longer than 10 ms. From this graph we can infer that we are indeed observing a cumulative effect that leads to disruption, as the pulse energy decreases there is an increase in required exposure duration. The shaded areas in the graph indicate regimes of no interaction or excessive cell damage. The transition from these regimes to the minimally disruptive subcellular nanosurgery is not sharply defined.

The mechanism behind the low pulse energy high repetition rate disruption is more complicated than pure plasma-induced ablation. There is experimental evidence that low density plasma is formed in the range below the optical breakdown [67]. It can in turn produce chemical changes, heating and thermoelastic stress [26]. These effects are very well localized due to the nonlinearity of the plasma-formation process, which at intensities near threshold is smaller than the diffraction-limited focus.

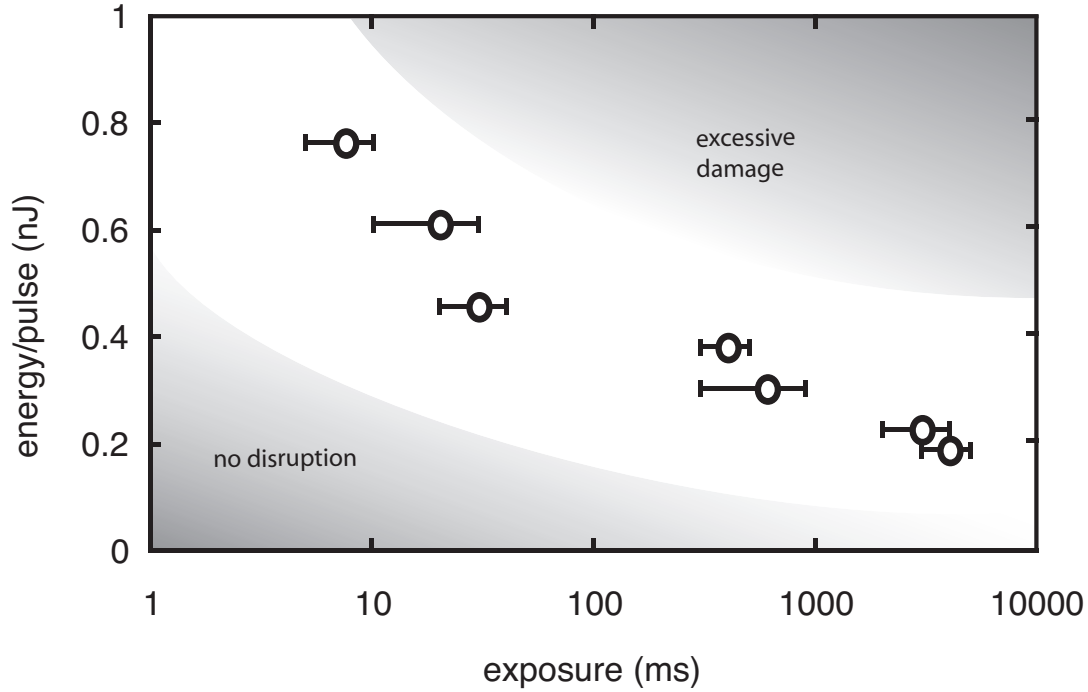


Figure 6.5: Threshold for ablation as a function of irradiation time and pulse energies for a 76 MHz pulse train. The shaded areas indicate regions of no disruption (lower left) and excessive cell damage (upper right).

In order to understand the conditions of disruption in this cumulative regime at high laser repetition rate we model the temperature distribution at the focus as a function of pulse energy and exposure time. The parameters entering this heat diffusion calculation are the material properties and the input laser parameters. The relevant material constants for water are the specific heat (1 cal/g K), density (1 g/cm^3), and thermal conductivity ($1.47 \times 10^{-3} \text{ cal/cm s K}$). The input laser parameters are pulse energy, laser focus radius, time separation between pulses (inverse laser repetition rate), and number of pulses (irradiation time). The way the temperature distribution is calculated is that it assumes 100% absorption of the incident pulse energy, then converts this energy into heat and calculates the heat diffusion away from the focal volume. If more than one pulse is deposited into the

sample, the model takes into account the diffusion of each pulse with respect to its arrival time and then adds the contributions of all pulses at the instant the last pulse is deposited. This model can also predict the radius away from the focus at which the temperature drops below a certain threshold; in this case, the threshold is 100°C . This should be an indication of extent of damage away from the focus.

Figure 6.6 is a plot of the maximum temperature reached versus radius for different input pulse energies at a repetition rate of 76 MHz. Two plots are shown, one for a train of 100 pulses and one of 1000 pulses. The maximum temperature is extremely high, tens of thousands of degrees, however, the radius at which this temperature rise occurs is very small, less than a few micrometers.

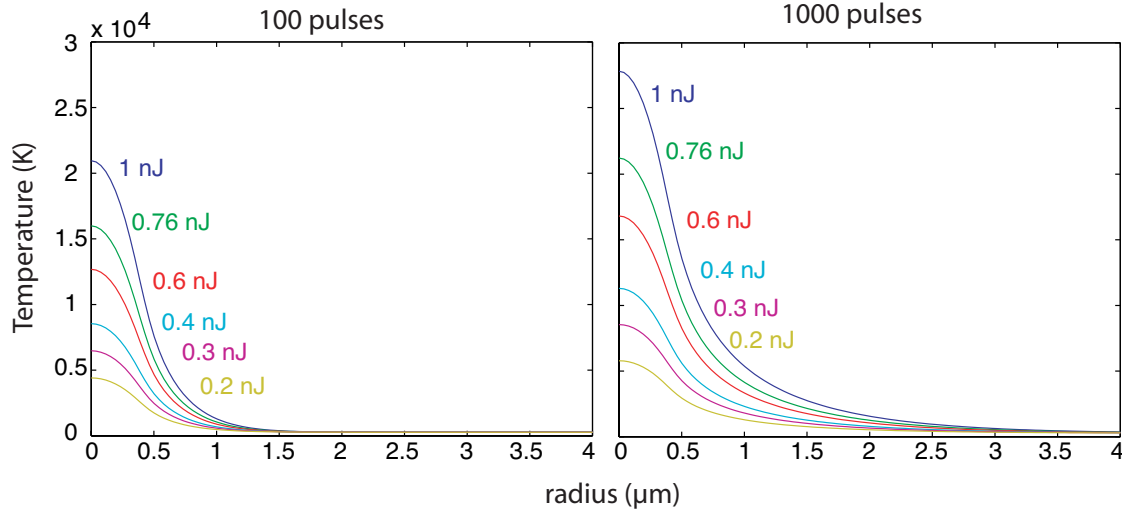


Figure 6.6: Heat diffusion calculation results for maximum temperature distribution after 100 (left) and 1000 (right) pulse are deposited at a 76 MHz repetition rate and varying pulse energies

We can calculate the radius at which the temperature rise is less than 100°C . Table 6.1 shows the maximum radius away from the center of the focal region that reaches 100°C . We see that while relatively confined, the boundary of the 100°C is further from the

focus than we would have predicted based on the experimental observations. The maximum radius for this temperature rise is calculated to be more than $4\text{ }\mu\text{m}$ for a 1000 pulses. This is an overestimate that results from some of the simplifications included in the model.

pulse energy (nJ)	0.2	0.3	0.4	0.6	0.76	1
max R 100 pulses (μm)	1.45	1.62	1.77	2.04	2.24	2.4
max R 1000 pulses (μm)	3	3.4	3.8	4.3	4.6	4.95

Table 6.1: Calculated maximum radius reached for irradiation with 100 and 1000 laser pulses at a 76 MHz repetition rate for different pulse energies.

This heat diffusion calculation is good in qualitatively justifying our assumption for a cumulative pulse energy damage mechanism at high repetition rates. However, there are many assumptions coming into this model that prevent it from providing a good quantitative agreement with experimental observations. First, the assumed energy converted into heat is 100%. We know this to be definitely not true, as there are reflection and transmission losses and the multiphoton absorption coefficient is quite low. Experimental measurements of the damage in glass can be used to fit the predictions of the model and they estimate about about 30% [29] to 40% [30] absorption of the pulse energy. There are no measurements for amount of energy converted in heat in water, so using 100% gives an absolute upper bound. While a smaller percentage is closer to the real conditions, there is no justification in using a specific lower value. Another consideration which cannot be accounted for in this model is that each subsequent pulse experiences different focusing conditions. The focal spot is heated up, there is likely local vaporization and a cavitation bubble is formed. All these condition contribute to distortion of the laser focus and change the amount of energy absorbed. The change in the absorption as a function of number of pulses likely also depends on the initial pulse energy, further complicating the model. Therefore, not

only do we not have a precise number on the initial absorption, but we cannot account for how it change in time. And the third shortcoming of this qualitative model is that it takes the bulk material parameters. When we are considering a small volume of $1 \mu\text{m}^3$, within a larger volume of water, the values of the bulk constants would likely deviate. However, with all these extra considerations taken into account, our first order qualitative approximation, does indeed show, that there is bulk accumulation of energy at MHz repetition rates, and that the high temperature rise is confined around the focal volume.

6.3 Variable repetition rate

We have shown that there is profound difference in the energy threshold at low kHz and high MHz laser repetition rate. However, there is a range of repetition rates in between which would have a disruption energy threshold different from the two extremes. To further investigate this problem we carried out experiments at the Laser Center in Hannover, Germany. The experimental setup there is schematically described in Figure 6.7. It is based on a Chameleon femtosecond laser system from Coherent. It has a repetition rate of 90 MHz and a tunable wavelength from 750 to 950 nms. The maximum output power is 1.3 W at 780 nm, which corresponds to 15 nJ/pulse. The laser pulse train is sent through an acousto-optic modulator (AO), which acts as a fast switch. It can pick a single pulse from the 90 MHz pulse train and deflect it from the original beam. The maximum switching rate is 4.5 MHz. The laser beam passing through the AO is split in two paths: a switched out beam with a low repetition rate and a high repetition rate beam which is missing pulses corresponding to the low repetition rate. For example, if the AO is set at a divide by 90, then we would have a switched out pulse train at 1 MHz, and the original pulse train will be missing one out of every ninety pulse. This system offers the advantage that it is possible

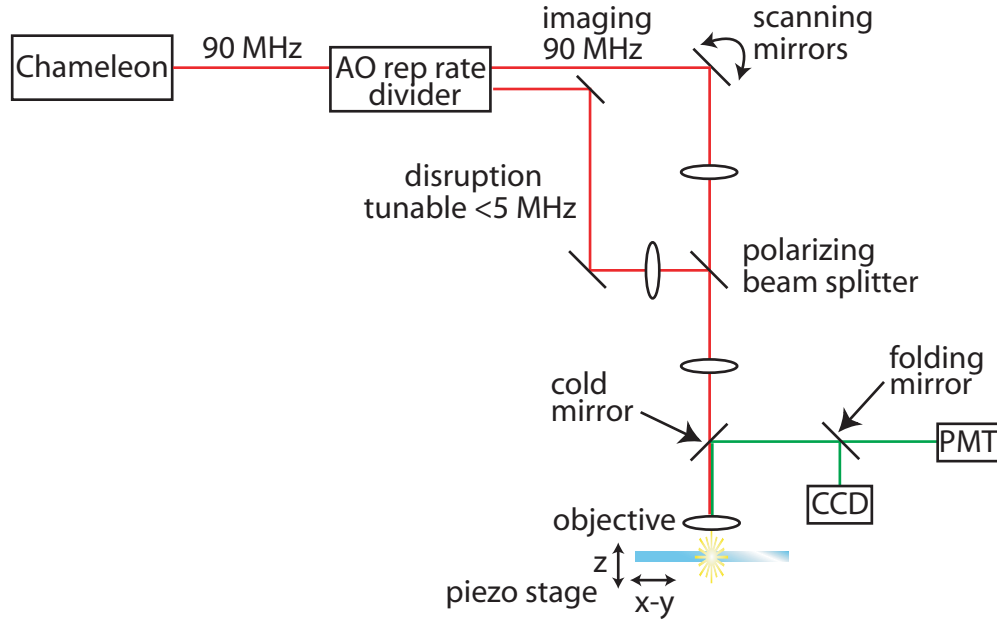


Figure 6.7: MPM imaging and nanosurgery setup based on a single femtosecond laser with a repetition rate pulse splitter (AO modulator). The high repetition rate pulses are used for imaging and the low (variable from single pulse to 5 MHz) repetition rate pulses are used for disruption.

to use the high repetition rate pulses for MPM imaging and the switched out pulse train for subcellular nanosurgery.

The imaging portion of this setup consists of a modified Zeiss microscope. This allows for white light imaging with a CCD and MPM imaging through a PMT. The original optics inside the microscope are removed and a PMT is placed at the bottom of a scope. A mirror can be pulled in and out of the setup to direct the light to the PMT or the CCD. The CCD can be used only to image white light illumination, which is extremely convenient when looking for small samples, that are sparsely distributed (such as cells plated on a glass slide) at high magnification. The sample is held by an adapted Thorlabs stage, described in Chapter 4. This allows for precise position and translation of the sample.

Figure 6.8 shows ablation at laser repetition rate of 4.5 MHz, 900 kHz, 180 kHz,

45 kHz and 18 KHz in a fluorescein stained epoxy. We used an epoxy, because we wanted a fluorescently labeled solid sample, where we could image the effect of the laser damage. The lines corresponding to different repetition rates were made by translating the sample with respect to the laser beam at $1\text{ }\mu\text{m/s}$. The energy per pulses is 2 nJ at the focus and is constant for all repetition rates. The width of the lines has a marked decrease at lower repetition rates as we expected. At the 18 kHz we observe a beading along the line, which is an artifact of the epoxy material that we are using. The likely explanation for this effect is that once a damage spot has been formed, the threshold for absorption in it is lower than outside and that traps the laser energy in it, resulting in a broken up line as the sample is translated along.

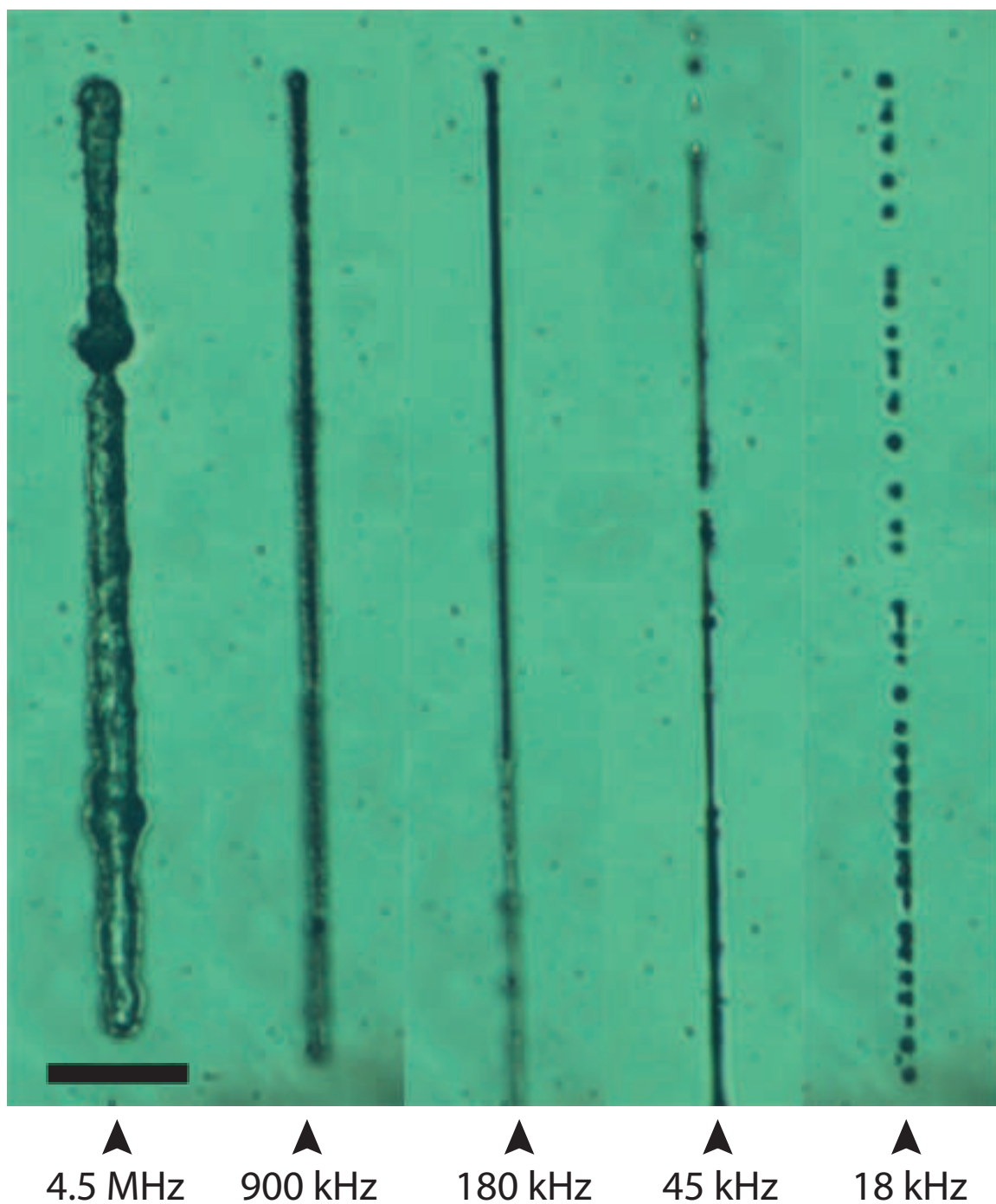


Figure 6.8: White light illumination images of fluorescein epoxy. Lines were ablated in the epoxy at different repetition rates showing the transition from the cumulative (4.5 MHz, 900 kHz) to the single shot regime. Scale bar = 50 μm

Initially, we set out to study the pulse energy threshold for actin at different laser repetition rates. Unfortunately, due to a few quirks in the setup, this proved to be a hard task. The first problem is that there is a small tilt to the stage and when translating the sample in the x - y plane there was a significant enough z translation. If the cells were sufficiently far apart from each other, moving from one cell to the next requires refocusing. In order to find neighboring cells, the imaging had to be switched from the PMT (fluorescence) to the CCD (white light) mode. This required for the PMT to be turned off, the collecting lens to be switched and folding mirror placed. The mirror mount holding that mirror is easy to misalign, further increasing the time necessary to switch from one mode to the other. The time necessary for this task made it impractical to undertake the size of the study (hundreds of cells), necessary to establish the shift in ablation threshold as a function of the laser repetition rate.

6.4 Outlook

This femtosecond nanosurgery and imaging setup has a potential for being an extremely versatile system when the above-mentioned engineering problems are solved. A necessary advantage of this system is the tunable wavelength femtosecond laser. This allows MPM imaging at different wavelengths by tuning the same laser source to the peak multiphoton absorption wavelength of the fluorescent label. Figure 6.9 is a fluorescence image of an endothelial cell which is transfected with YFP actin and the mitochondria are labeled with Mitotracker orange. A two-photon image is taken at the wavelengths corresponding to the peak two-photon absorption of Mitotracker, 850 nm and YFP, 950 nm. There is almost no overlap of the two excitations, and if we overlay the two images we can see the distribution of mitochondria with respect to the actin network.

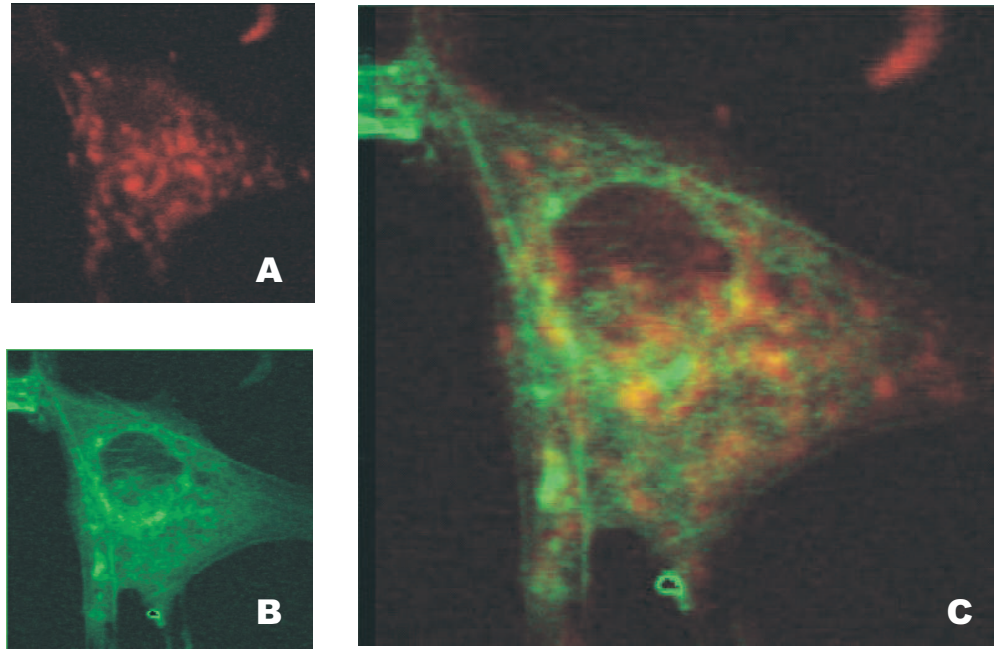


Figure 6.9: Two-photon image of an endothelial cell labeled with a) Mitotracker orange mitochondria, imaged at 850 nm and b) YFP actin imaged at 950 nm; c) overlay of both images

With this system we can take also SHG images of tissue samples. Figure 6.10 is the z-projection of a three dimensional image of a tissue sample taken from the oral cavity. The collagen fibers, which have strong second harmonic generation, are visible. The depth of the image is about $90\text{ }\mu\text{m}$ and three dimensional structure integration of the collagen can be clearly determined. This allows us to do minimally invasive studies in tissue systems.

6.5 Summary

We used actin as a model system to study the ablation threshold in living cells. Due to the prestress in the filaments, disruption is unambiguously marked by a pulling apart of the severed ends. The laser repetition rate has a profound effect on the disruption

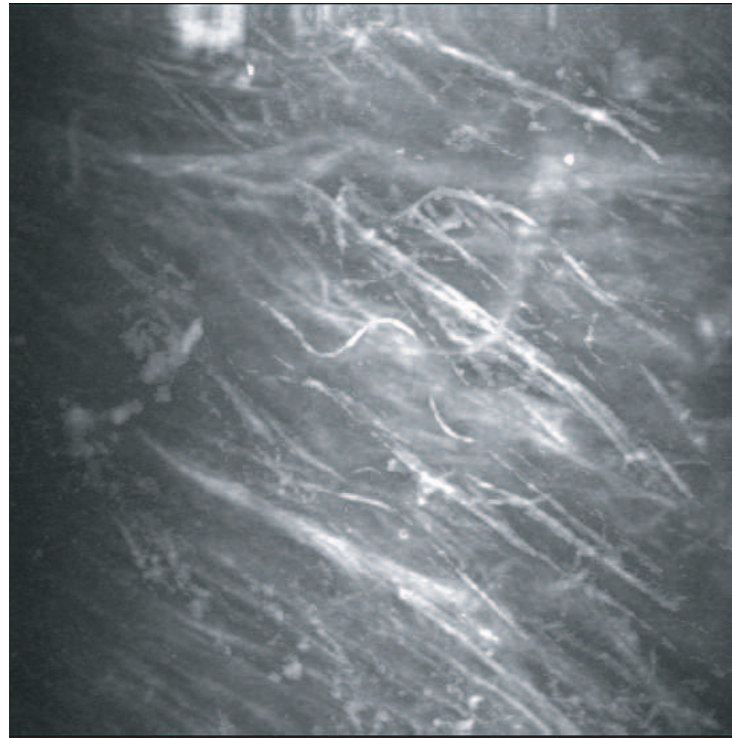


Figure 6.10: SHG image of collagen structures in healthy tissue.

in cells. It is not possible to carry over the ablation pulse energy and irradiation time from the lower repetition rate to the high repetition rate and vice versa. In one case we might cause bubble formation and whole cell destruction while in the other we might be below the ablation threshold and not achieve disruption. We have determined the minimum irradiation time necessary for filament disruption at 76 MHz for pulse energies below 1 nJ. The mechanism responsible for disruption is a cumulative damage due to bond breaking and localized heating due to the energy accumulation in the focal volume.

We were able to set up a combined nanosurgery and imaging setup based on a single tunable high repetition rate source and an AO pulse switch. This allows us simultaneous disruption and MPM imaging through a tunable source. Unfortunately, some engineering hurdles were a hindrance in being able to carry out a systematic study on ablation threshold

in cells with varying laser repetition rate and define the optimum conditions.

Another important question which arises from the variable repetition rate disruption study is at what laser parameter do we induce the least collateral damage to the cell. It is easy to visualize the least amount of energy for actin cutting: the actin filaments separate. And there is a maximum upper bound to the energy, which is a visible cavitation bubbles. But within this energy range the disruption mechanism can be predominately plasma-induced ablation (kHz) or local heating and vaporization (MHz). Which of these is less harmful to the cell? In a future study it might be possible to visualize calcium propagation through the cell or reactive oxygen species generation, which can be used as indication for distress in the cell. Then the relative magnitude of these markers can be compared at the different range of laser parameters.

Chapter 7

Probing cell mechanics: disruption of stress fibers in live cells

7.1 Introduction

Cell shape and deformation in response to external mechanical forces is critical for cell functions such as cell growth, differentiation, motility and apoptosis [59, 68, 69]. The geometry and the mechanical deformation of living adherent cells are determined by the cytoskeleton, a three-dimensional protein structure comprised of interconnected filaments of microtubules, actin and intermediate filaments [70–72]. Actin stress fibers assemble at the base of the cell and anchor to the extracellular matrix through focal adhesions across the cell membrane [73]. Cell shape is modulated by the polymerization of actin microfilaments that associate with myosin filaments, and by the resulting actomyosin-dependent traction forces that cells exert on their focal adhesion contacts with the ECM. The actin filaments assemble to form long, aligned actomyosin filament bundles, known as stress fibers, that span between each pair of focal adhesions at the cell base. The actin stress fibers are stiffer

than the surrounding cytoplasm and thus provide local shape stability as they are able to resist stress on a short length scale [74]. The contribution of these actin bundles at the base of the cell to shape stability over the entire cell length scale, often greater than hundreds of micrometers long and tens of micrometers high remains unclear.

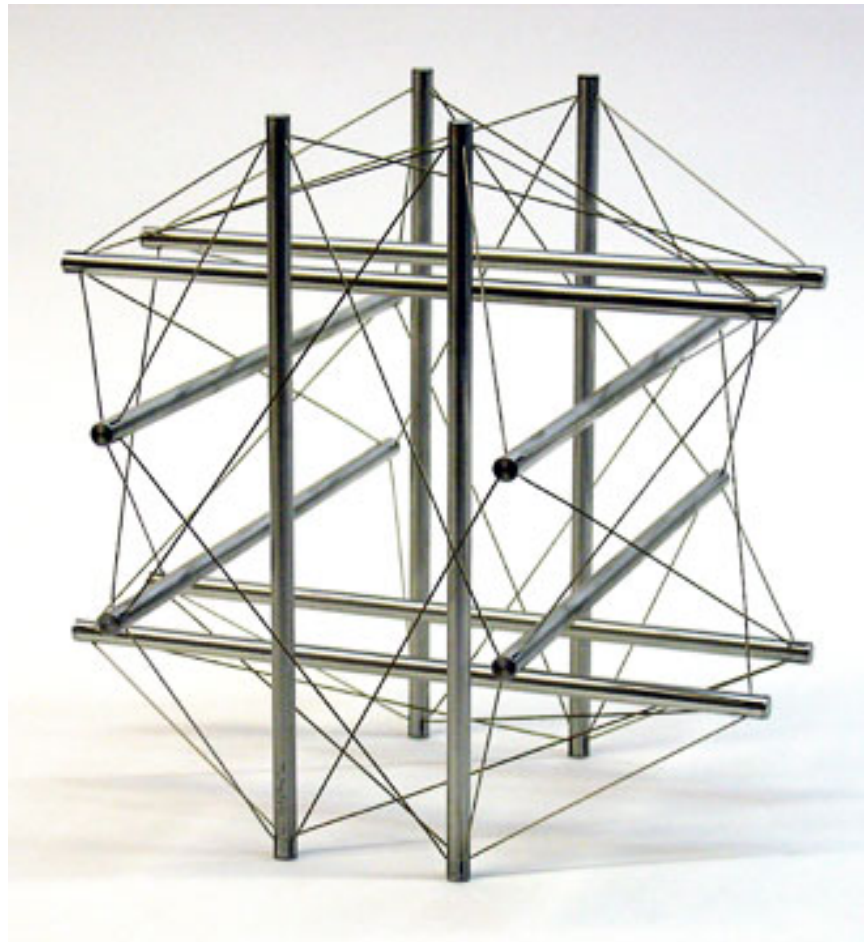


Figure 7.1: Double Six, 1967 a tensegrity based sculpture by Kenneth Snelson. Reprinted with permission of the artist. [18]

A comprehensive theoretical model of cell mechanics, called cellular tensegrity, predicts that cell shape stability may be governed by the level of pre-existing tensile stress or isometric tension stored in the cytoskeleton. In general, tensegrity structures are stabilized

by "tensional integrity" or continuous tension rather than by compression (i.e. a stone arch) [75]. Tensegrity structures rely on a network of flexible elements under tension along with stiffer elements which resist compression. This building principle was first described by architect R. Buckminster Fuller [76] and most prominently visualized in the sculptures of Kenneth Snelson [18]. Figure 7.1 is an example of a sculpture by Snelson, where the stiff rods are pulled in place by ropes to form a stable structure [18]. Cells can also be modeled as tensegrity structures in which the actin network is under tension and the microtubule array and the culture substrate are under compression [71, 75]. This model still remains controversial [77–79] and a major limitation has been the ability to evaluate the load bearing properties of individual stress fibers in living, adherent cells.

There are many approaches to understanding the mechanical properties of actin and its contribution to cell shape. It is clear that stress fibers in cells align and deform in response to external tension that is transmitted through the focal adhesion attachments to the extracellular matrix [80–82]. However, all the available quantitative data on the stress fiber mechanics come from in vitro experiments, when the fibers have been removed from the living cell [83, 84]. Alternatively, pharmacological tools are commonly used to underline some of the contributions of actin network to cell shape and function. However, introducing chemicals to the cell affects the entire actin lattice that permeates the cytoplasm and does not permit the study of individual stress fibers. For example it has been shown that large stress fibers disassemble in living cells when the actomyosin-based contractility has been inhibited or the stiffness of the extracellular matrix has been decreased [85–89]. It is also known that stress fibers are actively tensed in cells because certain actin-binding proteins in the cell assume a sarcomeric distribution [90, 91] and the fibers can be forced to contract in membrane-permeabilized cells with the addition of magnesium and ATP. In the end, there is little known about the properties of an individual stress fibers in situ, and how they

contribute to the prestress in the cytoskeleton or the surrounding extracellular matrix and their importance for the overall shape and stability of the whole cell.

Cell shape and tensile load distribution across the cells is directly related to the arrangement of actin stress fibers along the base of the cell. As actin filaments assemble and disassemble rapidly in lamellipodia (the mobile edge of the cell) and other cellular compartments [92–94], the entire cytoskeleton is regarded as highly unstable and cell shape changes are often ascribed to sol-gel transitions driven by actin polymerization [95–97]. The ability of the actin to rapidly polymerize has been used to argue that static forces, such as tensile prestress, borne by actin-based structures, does not significantly contribute to cell shape stability [78]. On the other hand, adherent cells can change their shape from round to fully spread without altering their total microfilament or microtubule mass [98,99]. Thus the relative contribution of the active polymerization-depolymerization dynamics and the static tensile prestress to cell shape stability remains a point of contention.

To directly show the tensile prestress in the actin cytoskeleton we used femtosecond nanosurgery [12,100] to sever individual stress fibers in living cells, while simultaneously visualizing the stress fiber retraction and cell shape change. As previously described in Chapter 5 this technique allows us to sever the stress fiber by ablating $< 300\text{ nm}$ section along the fiber without comprising neighboring structures or cell viability. We directly observed the retraction of the stress fibers after laser cutting and we show that their response can be modeled as that of viscoelastic cables. We also observed that the stress fiber retraction is slowed down by pharmacological inhibition of Rho-associated kinase (ROCK) and completely eliminated by inhibition of myosin light chain kinase (MLCK), thus demonstrating that the observed behavior is due to the contractile actin of unopposed myosin motors. As the traction force exerted by the cell on the substrate is proportional to the substrate stiffness, we performed traction force microscopy experiments. We cultured cells

on a flexible substrate and measured the deflection of the substrate after the laser stress fiber was severed and showed that the traction is primarily dissipated into the substrate along the axis of the stress fiber.

7.2 Materials and methods

7.2.1 Cell culture

Bovine capillary endothelial cells (passage 1015) were maintained at 37°C in 10% CO₂ on tissue culture dishes in a complete medium composed of low-glucose Dulbeccos modified Eagles medium (DMEM; Gibco-BRL) supplemented with 10% fetal calf serum (Hyclone), 10 mM HEPES (JRH-Biosciences), and glutamine (0.292 mg/ml)/penicillin (100 U/ml)/streptomycin (100 g/ml) as previously described [59]. For experiments, cells were transfected for 48 h with an adenoviral vector encoding enhanced yellow fluorescent protein (YFP)-tagged G-actin [53], trypsinized (TrypsinEDTA, Gibco), harvested, and seeded onto glass-bottomed 35 mm dishes (MatTek) in complete medium. Prior to imaging, cells were transferred into a CO₂-independent medium (pH 7.3) containing: CaCl₂ (1.26 mM), MgSO₄ (0.81 mM), KCl (5.36 mM), KH₂PO₄ (0.44 mM), NaCl (137 mM), Na₂HPO₄ (0.34 mM), D-glucose (5.55 mM), L-glutamine (2 mM), sodium pyruvate (1 mM), HEPES (20 mM) pH 7.4, 1% bovine serum albumin, 10% calf serum, and MEM essential and nonessential amino acids (Sigma) [101]. For ROCK inhibition studies, cells were treated with Y27632 (Calbiochem) for 1 hr at 10 μ M. For MLCK inhibition studies, cells were treated with ML7 (Sigma) for 30 *min* at 67 μ M.

7.2.2 Laser nanosurgery and photobleaching

For measurements of retraction dynamics of stress fibers, we used a previously described custom-built femtosecond laser nanosurgery system, Chapter 4 [12, 100]. Briefly, a passively mode-locked oscillator delivers 100-fs laser pulses at a repetition rate of 80 MHz and a central wavelength of 790 nm. These pulses are amplified in a chirped-pulse system to energies of up to 1 mJ at a reduced repetition rate of 1 kHz and then attenuated to energies known to produce subcellular material ablation at sub-300 nm precision (1-2 nJ). The laser light is then focused onto the intracellular target with a 63x, 1.4-NA oil immersion objective lens (Zeiss Plan-Apochromat) that is also used for real-time imaging. The sample is epilluminated with light from a UV lamp that passes through the appropriate filter cube; fluorescence emission is collected through the objective lens and recorded by a camera (Photometrics CoolSNAPcf). Images were collected using IPLab (Scanalytics).

For studies in which the femtosecond laser nanosurgery was combined with either photobleaching or traction force microscopy, we used a Zeiss upright laser scanning confocal microscope (LSM 510 Meta/NLO) equipped with a 63x, 0.9-NA water-dipping objective optimized for infrared imaging (Zeiss IR-Achroplan). To visualize YFP-actin and Texas red-labeled microspheres, we scanned the sample with the 488 nm laser line attenuated to 10% maximum transmission. Both YFP and Texas red emission were collected through the objective lens and then separated using primary and secondary dichroic beam splitters. Bandpass filters appropriate for either Texas Red or YFP emission fluorescence positioned in front of separate photomultiplier tubes enabled simultaneous red and green imaging. Single stress fiber was disrupted by focusing energy from a pulsed Ti:Sapphire laser at 100% transmission (Chameleon, Coherent) over a $0.5 \mu\text{m}^2$ area within the body of the stress fiber for 15 iterations (approximately 170 μs) through the objective lens at a wavelength of 740 nm, nominal laser-head power of 1.5 W, pulse duration of 140 fs, and repetition rate of

90 MHz. For photobleaching, fluorescent structures were irradiated with a 488 nm laser for 150 iterations at 100% transmission. Images were collected using the Zeiss LSM 510 software (version 3.2). All experiments on both microscopes were performed at 37° C using a temperature-controlled stage. In both cases, the objective lens of the microscope was focused onto the plane adjacent to the base of the cell to ensure interrogation of basal stress fibers.

7.2.3 Traction force microscopy

Fibronectin-coated polyacrylamide substrates for traction force microscopy (Young's modulus of 3.75 kPa) were prepared on glass coverslips, as previously described [62, 102]. Texas red-labeled microspheres (0.5 μm diameter, Molecular Probes, Eugene, OR) were suspended in the polyacrylamide before gel formation and used as fiduciary markers. Maps of substrate displacement (strain) and traction relaxation associated with single stress fibers were computed from bead positions before and after stress fiber incision using Fourier transform traction cytometry [103]. To measure tractional force returned to the ECM substrate by the cell (i.e., traction relaxed), we used the positions of the fiduciary markers before laser incision as the baseline state, rather than the positions of the beads in the unstressed (cell-free) gel. Cells were cultured and imaged on these substrates under the conditions described above. Changes in cell shape induced by laser severing of individual stress fibers were measured by using computerized image analysis (Zeiss LSM 5 Image Browser) to quantify alterations in the longest cell diameter oriented parallel to the severed fiber. In all cases, these length measurements were made at the focal plane of stress fiber incision, near the cell-ECM interface. The contrast of fluorescent images of cells expressing YFP-actin was digitally enhanced to visualize the thinnest portions of the cytoplasm, and thereby optimally define the cell periphery in these studies. The Student's t-test was used to determine

statistical significance between changes in cell length induced by stress fiber cutting in cells cultured on rigid versus compliant ECMs.

7.3 Results

7.3.1 Disruption of individual actin stress fibers in living cells

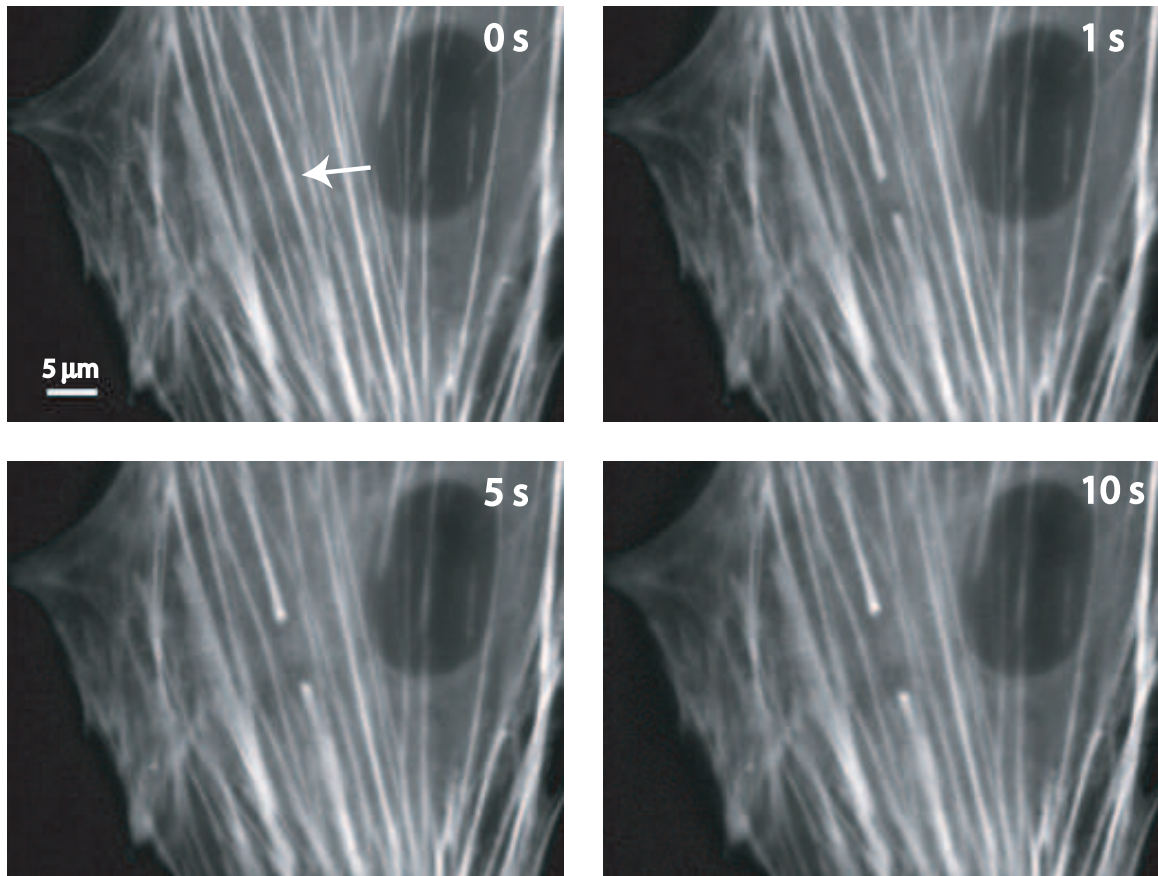


Figure 7.2: Severing and retraction of single stress fibers in living endothelial cell expressing YFP-actin

We used femtosecond nanosurgery to directly probe the mechanical properties of stress fibers in adherent, living endothelial cells that express YFP-actin [101]. The YFP-transfected cells generated stress fibers much like endogenous actin in these cells. These cells

also attach, spread, move and proliferate normally. The laser pulses are focused through the bottom of the glass cover slip onto the stress fiber. Figure 7.2 is a series of four time lapse fluorescence images, where the first image is of the cell before the laser pulses are applied and the following show the cell 1 s, 5 s and 10 s after laser irradiation. The actin network is the only fluorescently labeled structure in the cell and only it is visible in these images. The fibers are spread out across the base of the cell, and their ends are anchored to the glass dish through the focal adhesion. The arrow in the first image indicated the stress fiber where the laser pulses are targeted. After laser irradiation, severed ends pull away from the incision site as a result of the release of the isometric tension in the stress fiber. They also pull directly away along the original line of the fiber, which is consistent with the model that the tension is borne at the end points of attachment of the fiber. The newly severed ends also fray or widen, shown in the inset in Figure 7.2, as expected of a suddenly unloaded elastic element [104].

To ascertain the precision of the femtosecond laser nanosurgery, we focused the laser pulses onto fibers that were in close proximity to other stress fibers. Figure 7.3a and b shows two different cells before and after nanosurgery. Arrows indicate the irradiated stress fibers in the images on the left, before the laser pulses were applied. The images on the right reveal that only the targeted fibers were severed, while the neighboring fibers, distance less than $1\ \mu\text{m}$ away remained undisrupted. This is once more a confirmation of the precision of the laser femtosecond nanosurgery technique and an indication of its minimally disruptive nature.

The interaction area of the laser beam with the actin fiber can often be smaller than the width of the fiber, as in Chapter 5, we showed that the minimum incision width can be as small as 250 nm. Therefore, it is possible to puncture a whole in the stress fiber without severing through the entire filament. Figure 7.4a is an illustration of such a scenario. The

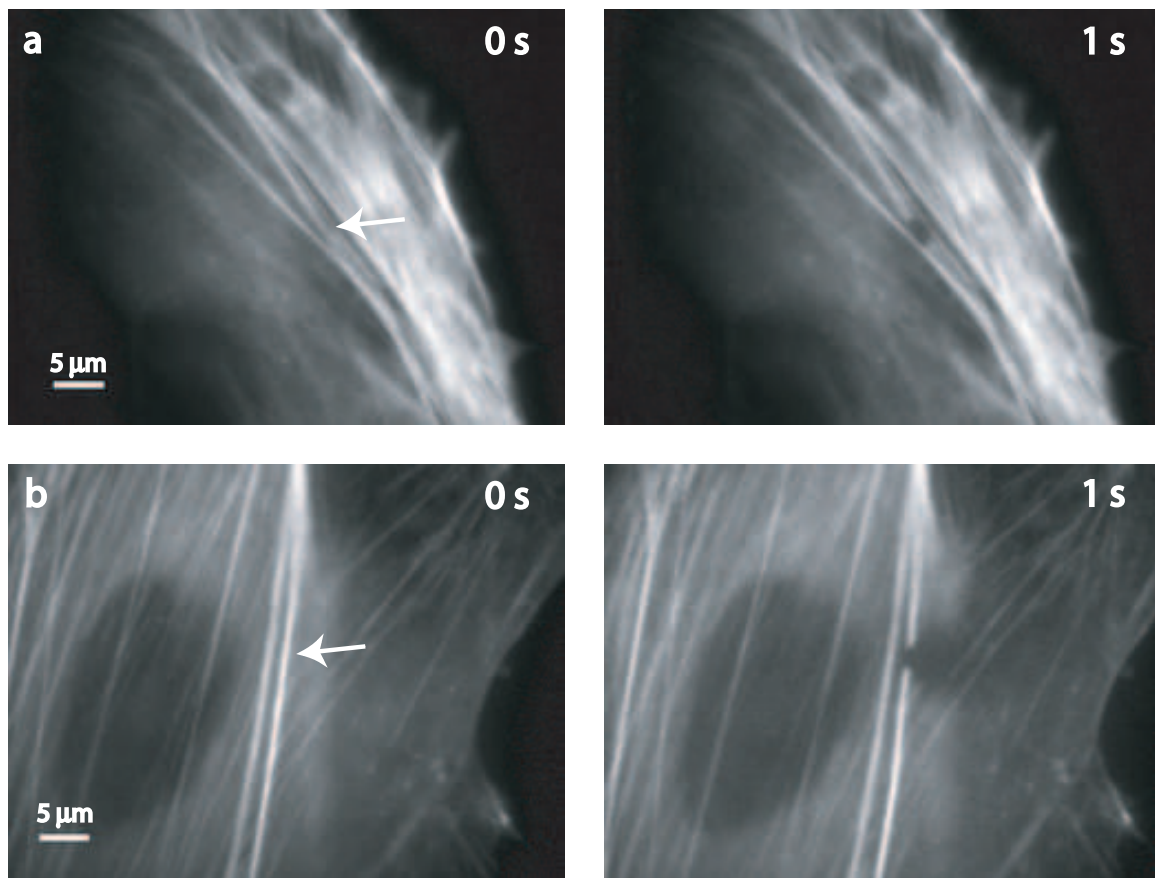


Figure 7.3: A fluorescence image of live endothelial cells transfected with YFP actin. a) and b) show different scenarios where the actin filaments are in close proximity with each other and only a single filament is cut.

figure again shows time lapse images which show the hole becoming progressively elongated along the axis of the filament over the course of 10 s. This is a result of the rearrangement of strain as the stress fiber attempts to accommodate the loss of tensile strength while supporting the same load. Figure 7.4b is an image of the same cell about 5 minutes later. The hole has greatly distended, though the two strings on either side still remain. We severed through one of the two remaining strands which pulled away, albeit at a much slower rate showing that it still retained some elasticity though the tensile load was vastly dissipated in this fiber.

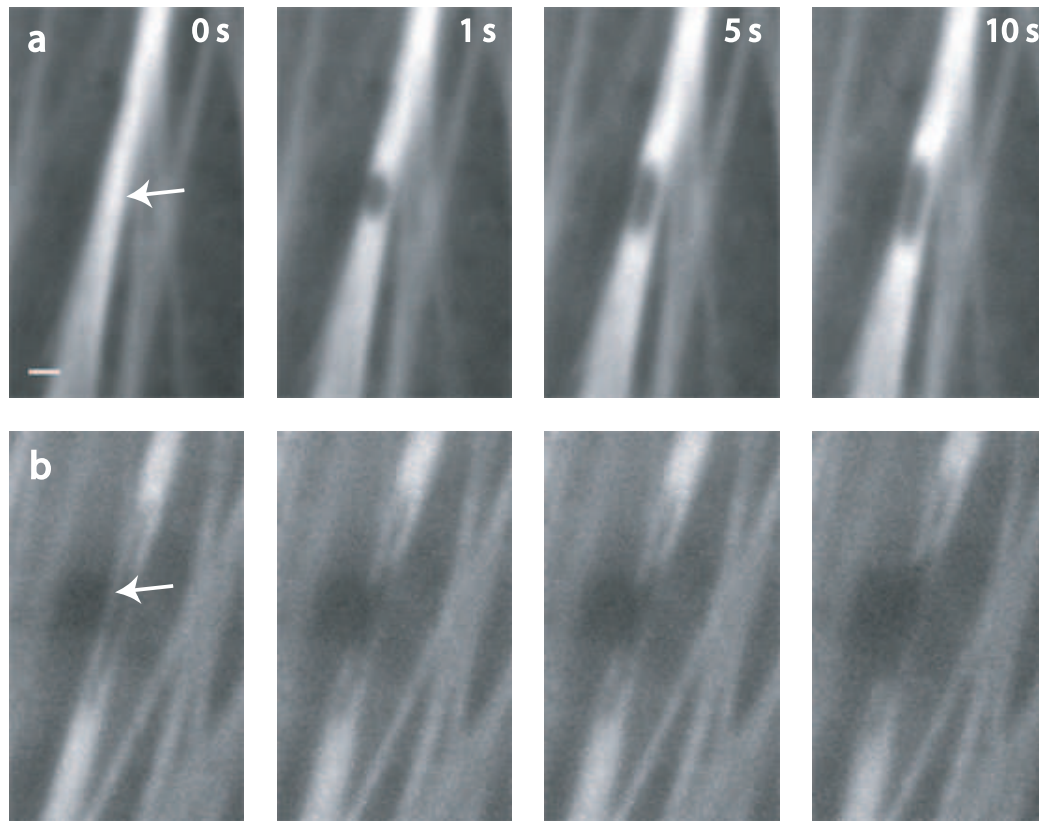


Figure 7.4: Strain relaxing in a single stress fiber after a 300-nm hole was punched in the fiber. The hole became elliptical as it distended along the original fiber tension field line. (Bar = 2 μm)

We needed to verify that the retraction that we are observing is due to the relaxation of mechanical forces rather than the rapid depolymerization of the filament. To distinguish between the two possibilities, we severed a fiber near a branching point. Figure 7.5b illustrates that if the filament were to disassemble due to depolymerization at the bifurcation point, then both branches will become unraveled. The image sequence in Figure 7.5a show that there is a relaxation rather than a disassembling at the incision point, leading us to the conclusion that we are observing mechanical forces in action rather than substantial actin depolymerization on the time scale of the experiment.

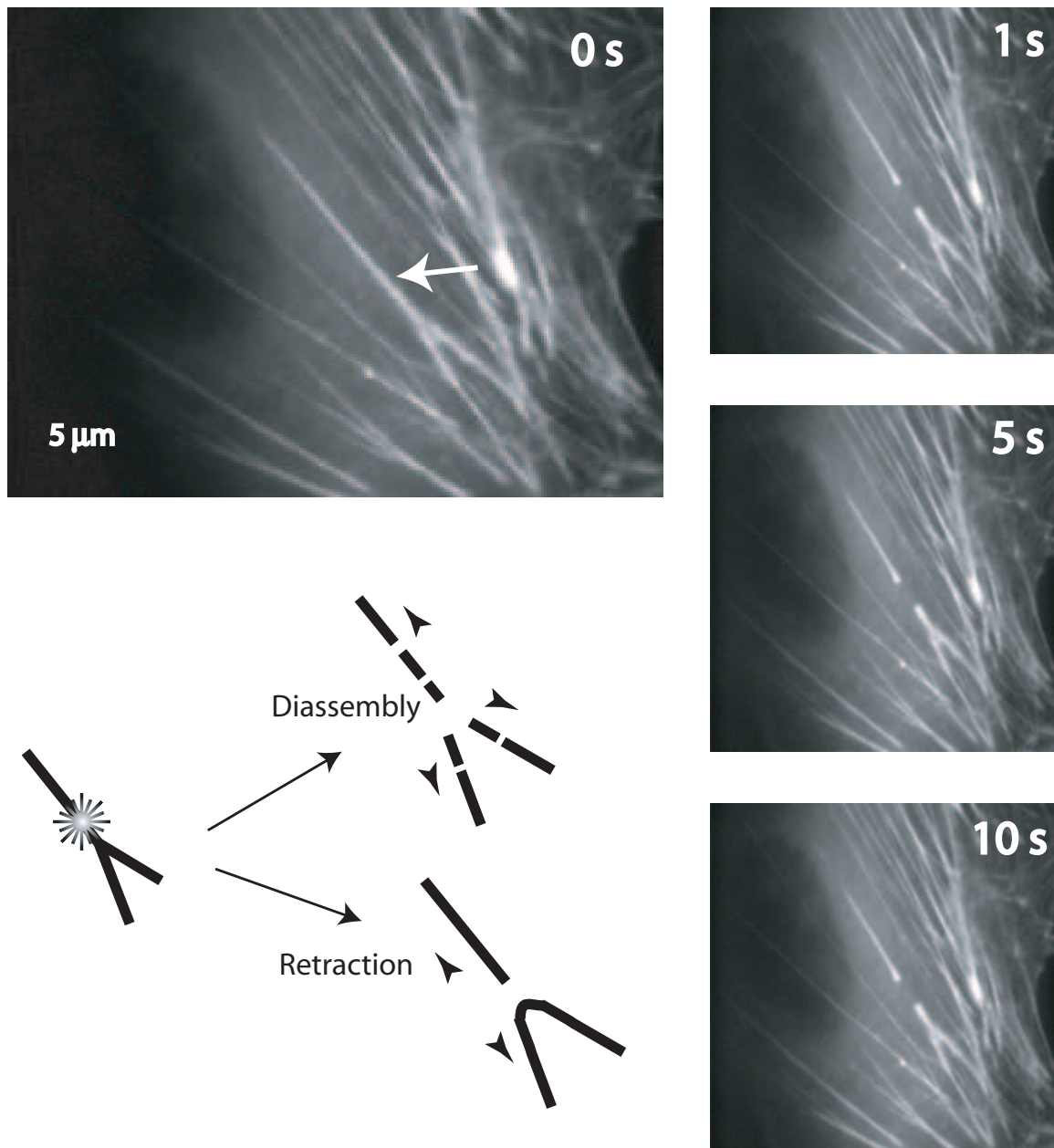


Figure 7.5: Actin stress fibers retract rather than dissolve. Schematic shows predicted observations in the case of stress fiber retraction versus diassembly in response to laser incision. In the case of actin depolymerization (top), both severed ends of the bundle should diassemble, including the branch point. In the case of passive elastic retraction (bottom), the branched portion of the bifurcation will remain whole after irradiation and physically retract as an intact structure. The time lapse fluorescence images confirm this prediction.

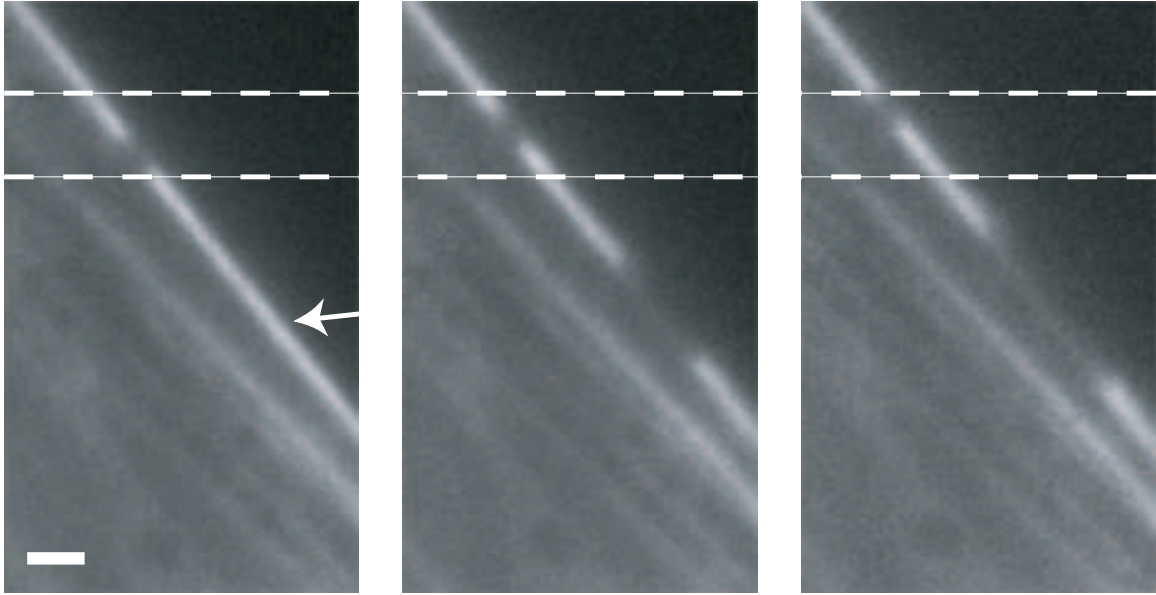


Figure 7.6: Stress retraction monitored by the motion of a photobleached spot. (Scale bar = $2\ \mu\text{m}$)

Additional evidence that femtosecond nanosurgery results in a physical retraction of the fiber, rather than wholesale disassembly came from an experiment where we combined laser photobleaching with nanosurgery. Photobleaching does not sever a stress fiber, instead it destroys the fluorescence in the structure, which in our case can be used as a marker to track the movement of the structure. We photobleached a spot along the fiber by using low laser power and longer irradiation time. We are sure that the fiber was not cut, because we did not observe the retraction we observe in the severed fibers. Then we focused the laser a few micrometers further down the same fiber and turned up the laser power to the nanosurgery regime. Figure 7.6 shows that as the fiber is cut both the severed ends and the photobleached marker move away from the cutting site. The dashed lines over the image serve as guides to track the motion of the marker. This result clearly demonstrates that the stress fiber physically retracts throughout its length when it is dissected; a disassembly would result in shortening of the severed ends without translation of the photobleached

zone.

7.3.2 Mechanical properties of stress fibers in living cells

Femtosecond nanosurgery allows us to visualize the dynamic retraction of a single stress fiber and determine its viscoelastic properties in its natural, physiological environment within the living cell. We can model the dynamics of the retracting fiber as that of a viscoelastic rope. The length of the gap between the severed ends grows at a rate described by a time constant and it asymptotically approaches the resting (unstressed) severed ends. Figure 7.7a is a plot of the distance a single end moves from the cutting cite at every time point. The solid line is a fit, based on the predicted retraction of a viscoleastic cable, which can be represented as a spring and a dashpot in parallel, in essence modeling the stress relaxation of the biopolymer, Figure 7.7b:

$$L = L_o(1 - e^{-t/\tau} + D_a) \quad (7.1)$$

In this model [105,106], L is the distance reacted (one-half of the distance between the two ends), L_o os the asymptotic value of that distance, t is the time after laser incision, τ is the characteristic time constant o the material equal to the ratio of the material damping coefficient to its Young's modulus, and D_a is the length of stress fiber vaporized and destroyed upon laser irradiation [100]. The damping coefficient arises from a combination of the intrinsic viscoelasticity of the stress fiber and that of the surrounding medium.

An important feature of this simple model is that it L_o and τ do not depend directly on the fiber width. Our experimental observation support this prediction, that there is no clear correlation between either these parameters on the fiber width for fibers between $0.2 \mu\text{m}$ and $0.8 \mu\text{m}$, Figure 7.7d and d. At widths greater than $0.8 \mu\text{m}$, τ increases significantly ($p < 0.001$), suggesting that the fiber width might affect the elasticity and/or

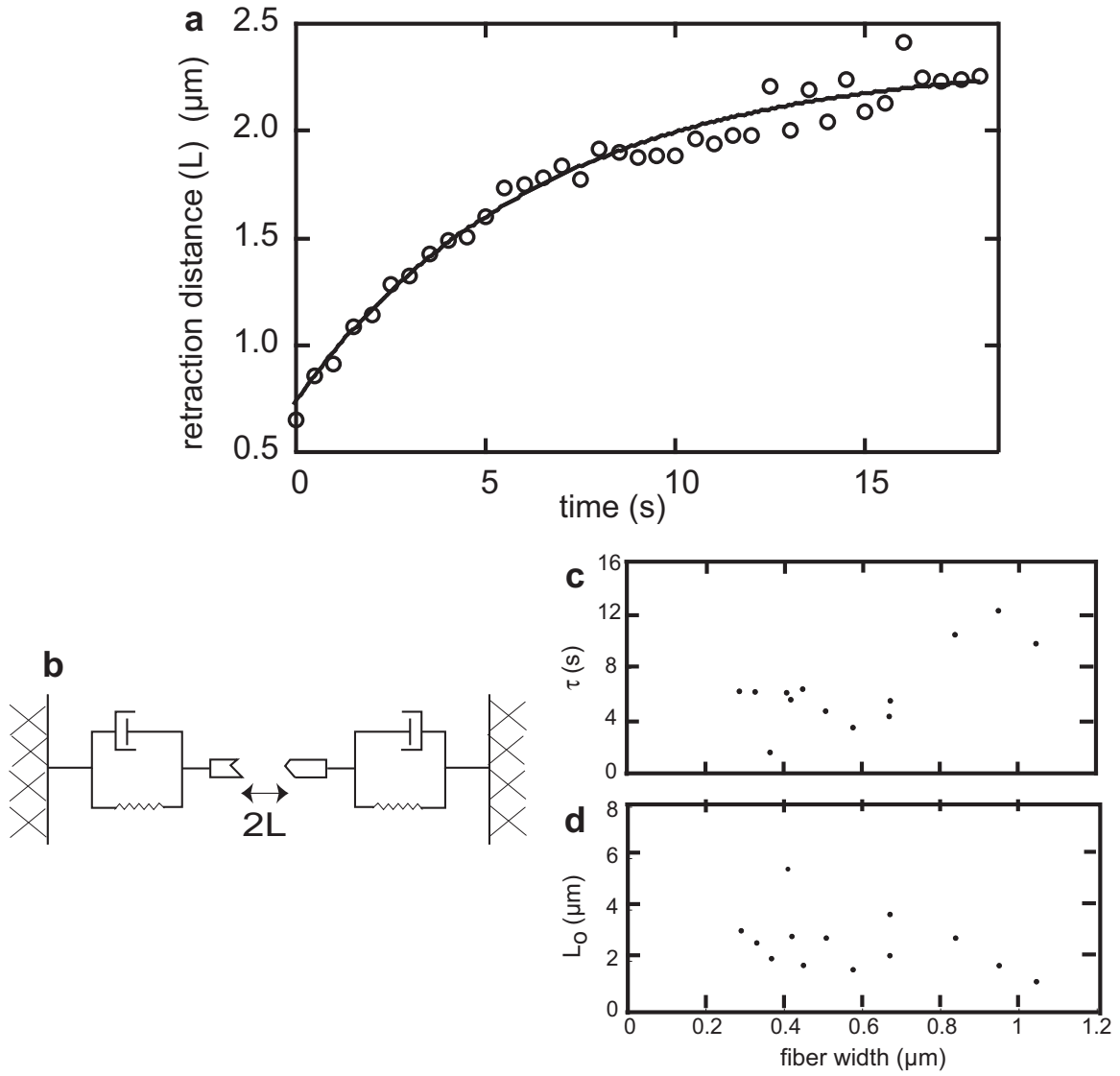


Figure 7.7: Modeling of stress fiber retraction. (a) Fiber retraction, defined as half the distance between the severed ends, (b) physical model for viscoelastic properties of the fiber, (c) dependence of τ and (d) L_o on fiber width. The data in (c) and (d) were obtained by severing a stress fiber in each of 13 cells.

viscosity.

Interestingly, material loss from the stress fiber could also conceivably follow first-order unbinding kinetics and therefore explain the observed retraction data. Indeed, even

though each stress fiber normally bears significant tensional loads and therefore functions as a static cable, the individual actin-based subunits contained within the intact filaments continuously turn over. To visualize this in our system, we conducted fluorescence recovery after photobleaching (FRAP) measurements on these stress fibers and found that the half-time for fluorescence recovery for actin was ≈ 5 min. This timescale of molecular turnover matches that found in previous FRAP studies of actin in stress fibers in fibroblasts [107]. Most importantly, it did not change significantly after the fiber was severed and tension was dissipated, showing that stress fiber tension does not significantly alter actin subunit binding kinetics under these experimental conditions. This finding, together with the branch retraction and photobleaching studies, make it exceedingly unlikely that the observed stress fiber retraction is due to actin depolymerization.

7.3.3 Tensional prestress in fiber bundles

Actin stress fibers can actively generate contractile forces through the action of myosin motors, however this functionality has never been demonstrated directly in non-muscles (actively contractile) cells. The contraction is triggered by the phosphorylation of myosin light chain (MLC) by the MLC kinase and the Rho-associated kinase, ROCK. In order to experimentally probe stress fiber contractility, we inhibited MLC phosphorylation, which is required for myosin motor activity, with two pharmacological agents that work by different mechanisms. The retraction dynamics for untreated cells and cells treated with the two different inhibitors are shown in Figure 7.8. First, we used the ROCK inhibitor Y27632 [108] at a dose of $10 \mu\text{m}$, that has been shown to optimally dissipate cytoskeletal tension and maximally inhibit a wide variety of tension-dependent behaviors in cultured cells, including endothelial cells [109–111]. As expected the inhibition of active tension resulted in a slower rate and shorter total distance of retraction in fibers severed in the treated cells, measured

over a period of 15 s. This result agrees with previous observations that stress fibers treated with Mg-ATP similarly contract with smaller amplitude and velocity in the presence of MLCK inhibitors in vitro [83]. However, Y27632 inhibits only one of many signaling pathways responsible for MLC phosphorylation and tension generation, therefore we observe some remaining tension in the stress fibers of the treated cells.

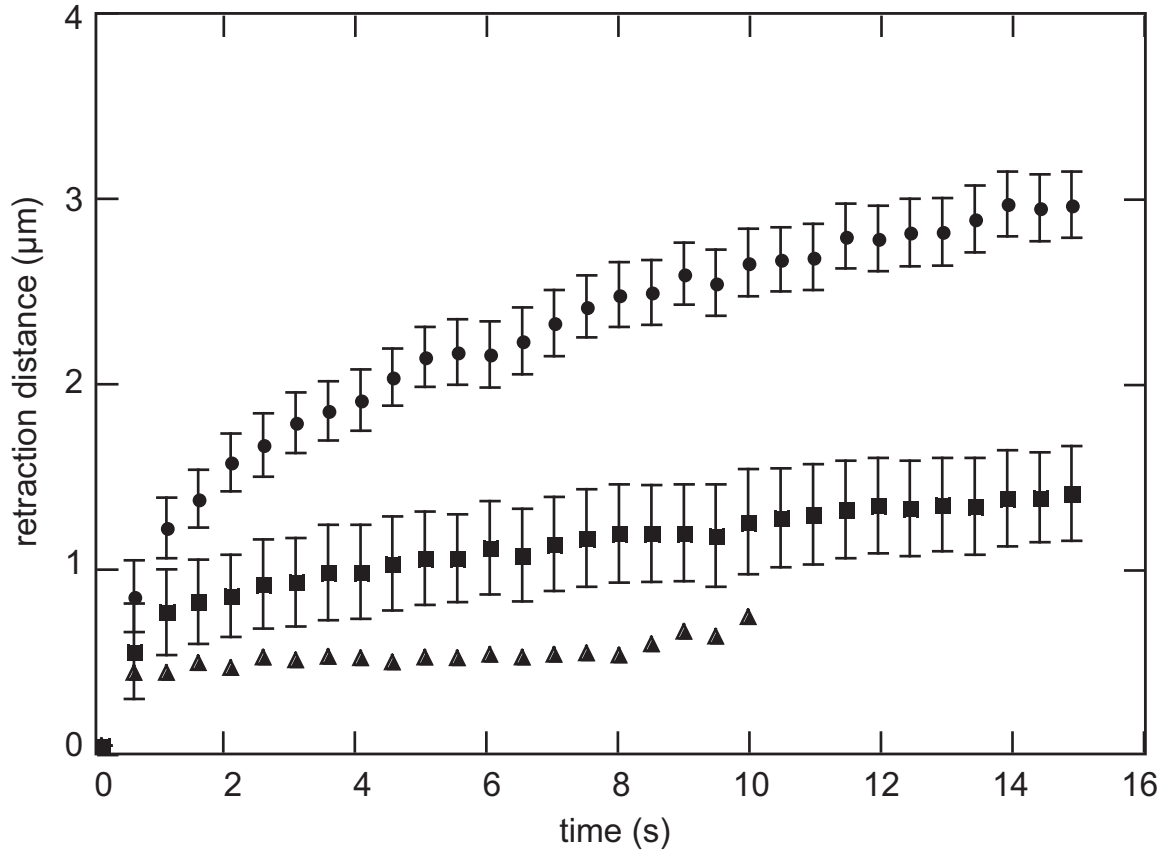


Figure 7.8: Contributions of active contraction versus passive prestress to stress fiber mechanics. Stress fiber bundles were incised in untreated control cells (squares, $N=13$), cells treated with the ROCK inhibitor Y27632 (10 mM) for 1 h (triangles, $N=19$), and cells treated with the MLCK inhibitor ML7 (67 mM) for 30 min (circles, $N=16$). Error bars represent mean \pm SE; solid lines are only visual guides. In all cases, one to two stress fibers were severed per cell in multiple cells. [19]

The second inhibitor that we treated the cells with, ML7, directly inhibits stress

fiber contraction [112]. After severing the stress fiber with the laser we were able to measure little, to no retractions. The value of the distance between the two severed ends was less than $0.5\ \mu\text{m}$, as shown in Figure 7.8, which is mostly accounted for by the section of fiber vaporized by the laser beam. Presumably, any additional retraction is due to a small amount of MLCK-independent motor activity or passive relaxation of the stretched stress fiber. Taken together, these data strongly suggest that stress fiber elasticity in untreated cells is primarily due to MLCK-dependent myosin contraction and the stress fibers are tensionally prestressed in a predominantly active fashion within living cells.

7.3.4 Contribution of single stress fiber to cell-substrate traction

When cells are adherent onto a surface the tension borne by the stress fibers is balanced by the traction exerted by the cell onto the substrate to establish a mechanical force balance. In the studies presented so far of cells attached to rigid glass substrate, the incision of a single stress fiber failed to produce any substrate deflection, cell shape change or rearrangement of the rest of the actin network. Even when several large, parallel stress fibers were severed the cell remained remarkably stable. Any transfer of force between the stress fiber and the substrate may be hidden by the rigidity of the substrate, which can bear forces much larger than those borne by a single cell. This is important because the ECM in living tissue is much more compliant than glass and in order to mimic the natural environment cells should be cultured on softer, flexible substrates [89,113,114]. To measure the mechanical contribution of a single stress fiber on the traction exerted by the cell on the substrate, we plated cultured cells on fibronectin-coated polyacrylamide gels containing 500 nm large fluorescent beads imbedded in the gel. Figure 7.9 shows a schematic of a cell plated on such a substrate. We performed traction force microscopy by tracing the motion of the beads [103,115,116] in response to the tension relaxation after severing a stress fiber

in the cell. We then calculated the force released by the cell and transferred to the substrate from the measured bead displacement and the known Young's modulus of the substrate (3.75 kPa) as described in [102, 103].

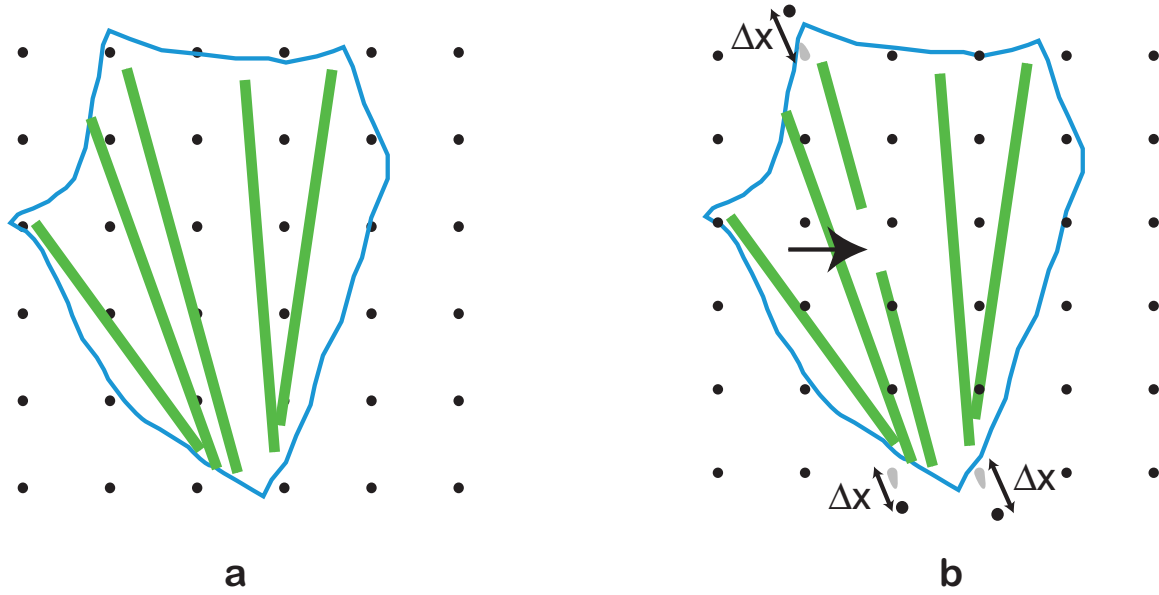


Figure 7.9: Schematic diagram of a cell plated on a flexible substrate with fluorescent beads embedded in it. As an actin filament is severed the tension relaxes and the beads in the substrate are deflected.

We took the preliminary data of for this experiment, showing that the disruption of a single stress fiber on a polyacrylamide gel leads to sufficient substrate deflection, which can be tracked and measured, on the custom built fluorescence microscope, described in Chapter 4. In order to visualize the stress fibers and bead independently, the stress fibers were expressing YFP-actin and the beads were labeled with rhodamine. This requires imaging in two different channels and also a translation in the z-direction, which allows to capture a sharp image of the beads in the substrate before cutting the stress fiber, then translating to the plane of the stress fibers to cut them, and then imaging the plane of the beads to measure the displacement after the fiber incision. This required not only very

precise z-translation, but also simultaneous imaging of two different fluorescent channels. With the custom built fluorescence microscope this required us to manually change the filter cube twice in the course of the experiment, prolonging the duration of the experiment, which lead to increase in the focus drift over time. We observed displacement of the beads after cutting a stress fiber. The beads were displaced in region where the stress fiber was anchored to the ECM through the focal adhesion, which often was many micrometers away from the cutting cite. The beads also were displaced in opposite direction at either end of the stress fiber, confirming the idea that the adherent cell generated tension that was borne by the stress fiber.

To improve on the image acquisition and be able to treat more cells consistently we performed the rest of the experiments on the commercial Zeiss confocal and multiphoton microscope at the Harvard Medical School. That allowed us to acquire real time multichannel imaging and finer z-resolution through the confocal microscope. A sample of the data and the analysis acquired with this system is presented in Figure 7.10 [19]. In part (A) is shown a confocal z-stach image of the the fluorescently labeled cell and the beads bellow it before and after the laser nanosurgery. Figure 7.10 B shows the displacement of the beads and (C) is the generated traction in response to the stiffness of the substrate. The maps of the substrate displacement and traction associated with a single stress fiber were computer from change in bead position before and after stress fiber incision.

Similar analysis of multiple cells revealed that laser ablation of a single stress fiber and associated disruption of the cellular force balance resulted in rapid, increase in the force transferred to the ECM that reached a plateau value of ≈ 179.5 Pa within 30-40 s, Figure 7.11. Because bead displacements were measured relative to the initial bead positions (i.e., when cells had already been allowed to spread and tensionally prestress the flexible ECM) and we do not know the strain distribution of the unstressed gel, we cannot determine the

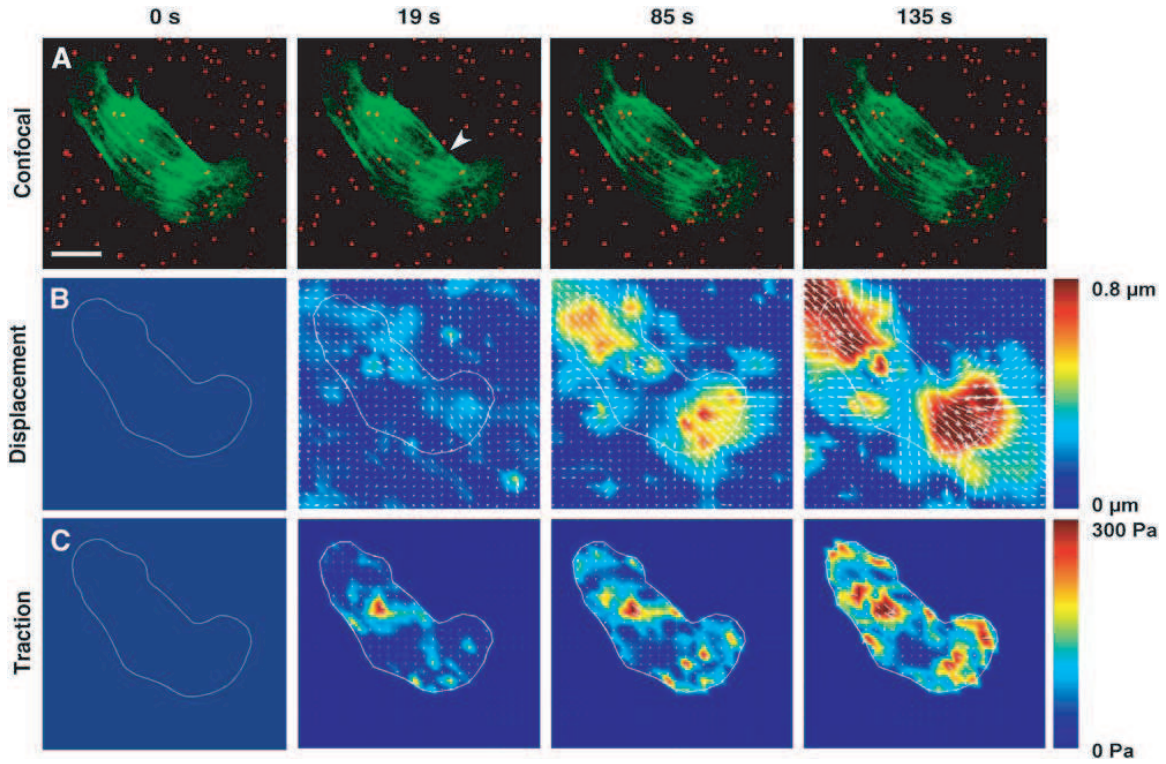


Figure 7.10: Contribution of a single stress fiber to cell traction forces and ECM displacement. (A) Confocal images of the actin stress fiber and the fluorescent beads (Arrowhead indicates the point of laser ablation; Bar = $20\ \mu\text{m}$). (B) Changes in bead displacement and ECM strain distribution. (C) Changes in cell traction as transferred to the ECM. [19]

total prestress borne by these cells. However, when we cultured endothelial cells on similar polyacrylamide gels and measured bead positions before and after the cells were chemically detached from their adhesions, the average whole-cell traction was determined to be $307 \pm 55\ \text{Pa}$, a value similar to that exhibited by the same cells in a past study [60]. Thus, the incision of one stress fiber dissipated a significant portion ($>50\%$) of the total prestress within these cells within 30 s after cutting, when attached to a flexible ECM substrate.

This shift of forces from the actin cytoskeleton to the flexible prestressed ECM also resulted in largescale structural rearrangements in the remaining actin cytoskeleton as well as global changes of cell shape. A comparison of fluorescence images of cells before and after

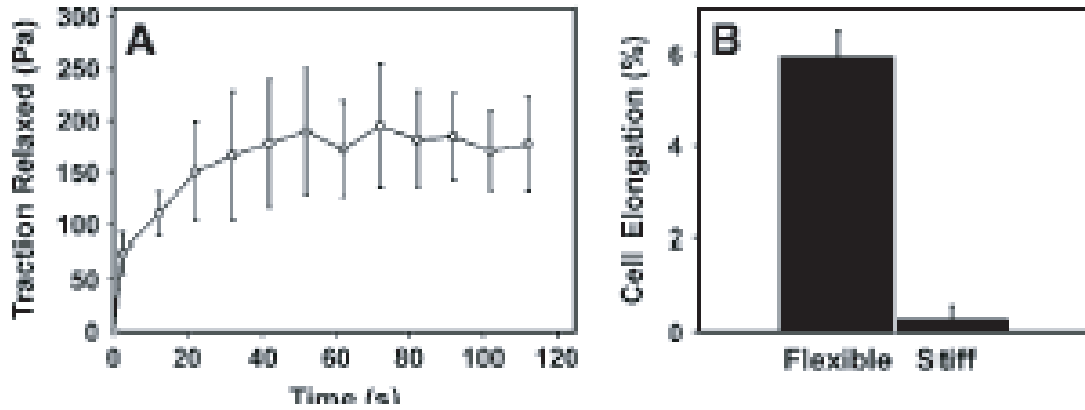


Figure 7.11: Effect of cutting a single stress fiber on force transfer to the ECM and associated changes in cell shape. (A) Graph showing changes of cell traction forces relaxed into the ECM substrate measured over time after laser ablation of a single stress fiber using traction force microscopy (N=5; data are presented as mean \pm SE). (B) Quantification of the effect of stress fiber incision on the global shape of cells adherent to flexible versus rigid ECM substrates [19].

laser ablation clearly demonstrates that although cutting a single stress fiber produced only local fiber retraction of that fiber at the point of laser cutting and no changes in cell form in cells on rigid dishes (Figures 7.11b and 7.12a), similar ablation of a stress fiber in cells on flexible substrates resulted in both this local effect and global rearrangements of multiple other stress fibers distributed throughout the whole length of the cell (Figure 7.12b). Again the largest outward displacements occurred along the main axis of the cut fiber (Figure 7.12b), and this corresponded to regions of the underlying ECM that exhibited the greatest lateral displacements (Figure 7.12c) and relaxation forces Figure 7.12d. Even when most stress fibers were oriented in parallel to the one cut by the laser (as shown in Figure 7.10, the remaining fibers located throughout the cytoplasm extended and thinned as the released tension was shifted from the cut fiber to these remaining cytoskeletal elements and their linked ECM adhesions. By measuring the maximum length of the cell at the focal plane of laser ablation and along the axis of the severed stress fiber, we were able to quantify

cell shape before and after stress fiber incision. This morphometric analysis revealed that the nanometer-sized incision of a single stress fiber resulted in nearly a 6% increase in cell length on flexible substrates, whereas there was no significant change in length in cells on rigid glass substrates, Figure 7.11b. Thus, alterations in the cellular force balance due to dissipation of tensile prestress within a single stress fiber located close to the basal surface of the cell resulted in structural rearrangements and changes in form throughout the entire cytoskeleton, as well as within its underlying ECM. These results confirm that the ECM is a physical extension of the cell and cytoskeleton, and that cell shape stability requires maintenance of isometric tension within the entire cytoskeleton, not just in stress fibers at the cell base [75].

7.4 Discussion

We used a femtosecond laser nanosurgery to sever individual stress fibers in living cells, quantified their retraction, probed biochemical contributions to their elasticity, and examined their contributions to the overall shape of cells cultured on rigid versus compliant ECM substrates. These data demonstrate that stress fiber bundles behave as viscoelastic cables, a concept that has been widely assumed but never directly experimentally demonstrated in living cells. Similar systems that utilized ultrashort lasers pulses have been previously used to sever microtubules [117], mitotic spindles [118, 119], mitochondria [12, 49], and chloroplasts [120] in living cells. In particular, stress fiber bundles have been irradiated and severed with picosecond lasers in the past [52, 53], but with insufficient spatial or temporal resolution to quantify retraction dynamics, or the transfer of strain to the ECM. By carefully tracking the retraction of severed stress fibers while manipulating intracellular tension and ECM compliance, we were able to characterize the mechanical properties of

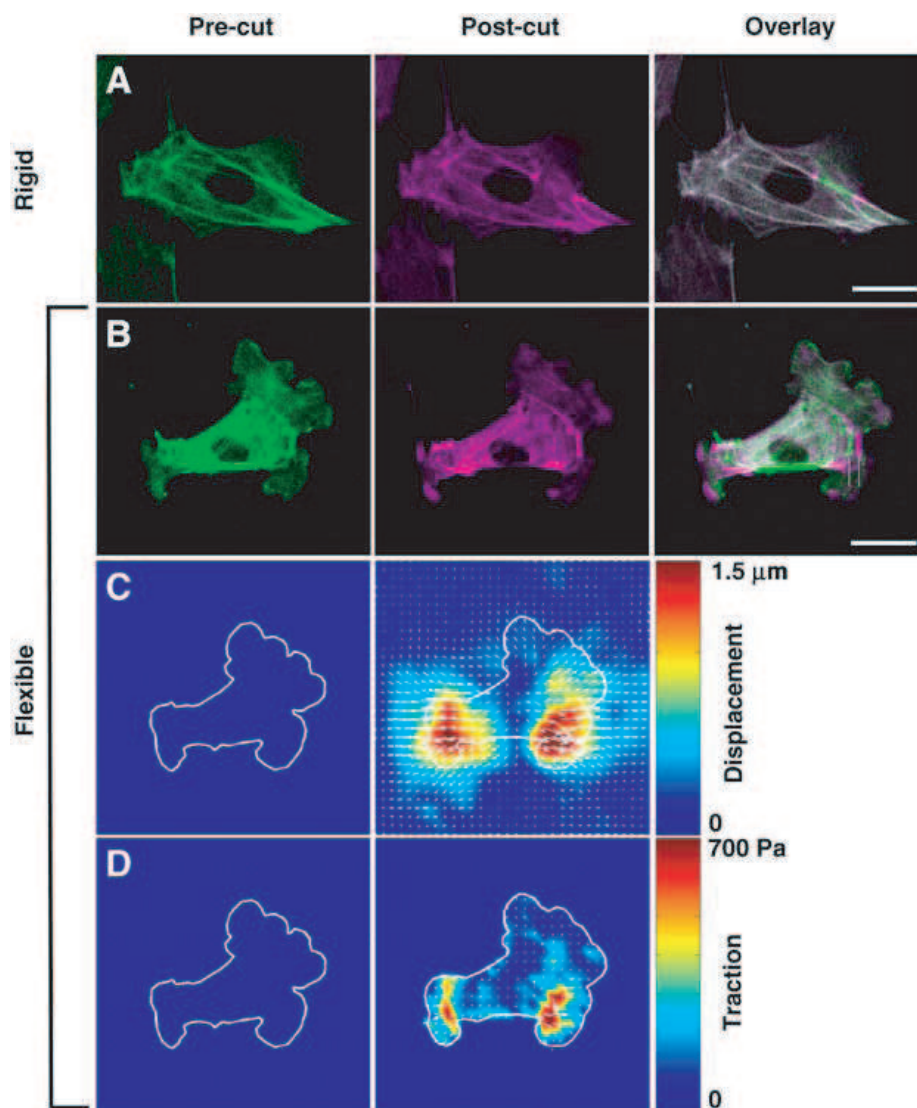


Figure 7.12: Caption [19]

individual stress fibers and define their contribution to the shape stability system of the entire cell with unprecedented precision.

The fact that we observed this behavior in living cells is critical, because previous in vitro work with single actin filaments [121–124], reconstituted actin gels [125], and isolated myofibrils [126, 127] has produced equivocal descriptions of stress fiber mechanics.

For example, stress fibers have been widely described as either tensile [128], elastic [129], or viscoelastic [130]. Our work represents the first unequivocal demonstration that stress fiber bundles retract viscoelastically within the complex living cytoplasm. These findings also confirm that individual stress fibers are tensed almost entirely by actomyosin motors, as evidenced by the complete abrogation of stress fiber retraction when MLCK is inhibited. The dose of Y27632 used in this study has been shown to profoundly (and optimally) alter cell shape and cytoskeletal morphology [109], whole cell prestress [111], cell migration speed [110], and focal adhesion size and turnover [131] in multiple cell types, including endothelial cells [131]. Thus, the reported here is probably not due to a failure of the cells to optimally respond to the treatment. Instead, the differential effects of Y27632 (ROCK inhibitor) and ML7 (MLCK inhibitor) on stress fiber retraction likely reflect the different mechanisms through which stress fiber myosin activity is regulated. MLCK facilitates myosin activity – and therefore stress fiber contractility – by phosphorylating MLC, whereas ROCK accomplishes this primarily by inhibiting MLC phosphatase, although it also may phosphorylate MLC directly [132–134]. The factors that determine the relative contributions of these two pathways to myosin activity are poorly understood, and it has recently been proposed that these pathways are spatially regulated as well (i.e., the contractility of fibers at different locations in the same cell may be under the influence of either MLCK or ROCK; [135, 136]. Rho has also recently been implicated in directing the orientation of stress fibers in response to ECM stretch [137]. Our finding that ML7 inhibits stress fiber retraction much more completely than Y27632 suggests that for the subset of stress fibers considered here, prestress is chiefly determined by MLCK, not ROCK. The myosin-dependence of stress fiber retraction implies that the prestress borne by these structures is due much more to active tension generation by myosin than to simple passive distortion (stretch) between points of attachment to the ECM (i.e., focal adhesions), at least in cells

cultured on rigid glass dishes. In other words, prestress is actively generated internally by actomyosin filament sliding within the stress fiber.

Recently, elasticity measurements have been reported for stress fibers isolated from smooth muscle cells [84]. Here, stress fibers shortened; 15% within 1 s of being mechanically dislodged from rigid ECM substrates, thereby leading to the conclusion that stress fibers in these cells are passively strained; 20% of their unstressed length. These measurements are complicated, however, because they were carried out after cell lysis, chemical digestion of the surrounding cytoskeleton, and mechanical disruption of focal adhesions. In a living cell, these supporting elements would all serve to brace a retracting stress fiber after incision, and our failure to observe substantial passive retraction in living cells reinforces the notion that stress fibers are intimately connected to surrounding structural networks, both inside and outside of the cell. Our findings therefore provide additional evidence for the need to carry out micromechanical analysis of cytoskeletal elements in the physical context of living cells.

Although stress fibers behave as viscoelastic cables for a large range of fiber widths, the thickest stress fibers deviate from this behavior and retract with greater effective drag. These larger fibers may either represent a distinct population of structures with unique load-bearing or contractile properties, or they may have more connections with the surrounding cytoskeleton due to their flat band-like geometry. The latter possibility is supported by electron microscopy studies which reveal that stress fiber bundles are physically connected to cortical and subcortical actin networks, intermediate filaments, and microtubules [138,139]. The larger the stress fiber, the greater the surface area presented to the surrounding cytoskeletal lattice, and hence the more extensive the lateral connections. Similarly, variations of stress fiber location (peripheral versus central) and connectivity (anchored at one end versus both ends) may also give rise to differences in measured elasticity. The experimental

approaches described here should help to clarify these regional variations in the future.

The finding that the retraction data are so well described by a viscoelastic cable model is intriguing given recent structural insights into the mechanics of stress fiber contraction. Specifically, when cells containing stress fibers labeled with GFP-tagged MLC and α -actinin were treated with contractile agonists, many stress fibers did not appear to contract uniformly along their lengths; instead, myosin activity preferentially concentrated at the stress fiber ends, causing the stress fibers to contract at their peripheries and stretch at their center [140]. This would predict either higher contractility or rigidity at the fiber ends compared to its center, and hence that there are significant local variations in its viscoelastic properties. However, we carried out all of our studies in the central region of the cell, far from the distal ends of stress fibers near where they insert into focal adhesions that contain a high density of actin-binding proteins. Thus, our data describe the mechanical behavior of the central portion of the stress fiber, which apparently behaves like a viscoelastic cable that is mechanically homogeneous along its length. Severing stress fibers tagged with internal structural labels at different distances from the focal adhesion along its length should help to clarify these more subtle mechanical responses in the future.

Compromise of a single submicrometer-wide stress fiber located close to the basal cell membrane produces large-scale architectural rearrangements throughout the entire cytoskeleton, changes in overall cell shape, and mechanical restructuring of the ECM when cells are cultured on flexible substrates. This is consistent with the finding that mechanical stresses can be transmitted from the cell apex to the basal membrane of the cell, as well as from the surface membrane to the nucleus, through linked integrins, microfilaments, microtubules, and intermediate filaments that collectively form a single cytoskeletal-integrin-ECM lattice [101, 141–143]. Our work also confirms that cell shape stability requires that this entire cytoskeletal lattice be maintained in a state of isometric tension that, in turn, results

from a balance between cytoskeletal tensional forces and the mechanical compliance of the ECM [75, 141, 144].

We do not observe large-scale changes in cell and cytoskeletal form when stress fibers are severed in cells adherent to a rigid ECM. Here, cellular remodeling is kept to a minimum, because the rigid ECM is stiff enough to bear the forces transferred from the cut stress fiber without distending or compromising the overall cellular force balance. The fact that actin bundles less than a micrometer away do not remodel or change their arrangement after irradiation, even on the time scale of minutes, effectively rules out any nonspecific, irradiation-induced change in cellular biochemistry (e.g., local release of calcium) or increase in temperature that might produce local cell contraction. In contrast, when cells are cultured on a more compliant ECM substrate that is already prestressed due to the contractile activity of the adherent cells, disruption of a single stress fiber results in large-scale retraction of the ECM, much like cutting part way through a rope in the midst of a game of tug-of-war would cause the opposing teams to pull away from each other. The retracting ECM pulls the cell adhesions and linked cytoskeleton apart and stretches the entire cell outward until a new force balance is established.

In mechanical terms, the compliance of the ECM controls the degree to which disruption of one stress fiber bundle will influence cell shape in at least two ways. First, a rigid substrate deforms less than a flexible substrate upon absorbing a given amount of traction. Thus, disruption of a stress fiber in a cell cultured on a rigid substrate is expected to produce a smaller change in the strain distribution (distortion) of the substrate compared to a flexible substrate. Cells also actively sense and adapt to the rigidity of the ECM [102, 113, 145], and greater ECM rigidity increases contractility [102], bolsters focal adhesion size and density [146], and permits greater cell spreading and migration speed [110], implying that focal adhesions in these cells are collectively capable of bearing greater loads.

The ECM rigidity-dependence of the stress fiber contributions to cell shape takes on particular physiological significance when one considers that in living tissues, cells adhere to compliant ECMs and fibrin gels (e.g., during wound healing) whose mechanical properties much more closely resemble a soft gel (Young's moduli; 11000 Pa) than a rigid glass surface [89,113,114]. Local changes in ECM compliance may therefore provide an important mechanism for effecting rapid changes in cell shape and cytoskeletal structure that may in turn provide a directional cue for migration. This notion is supported by the strong dependence of many cell behaviors on ECM rigidity [110,113,146], and the observation that cell migration may be guided purely by gradients in substrate stiffness, independent of type or density of ECM proteins [130]. This force balance manifests itself at the organ/ tissue level as well; local changes in cell growth patterns and tissue development can be influenced during embryogenesis by altering the level of cytoskeletal tension within the growing cells that, in turn, alters ECM structure [147]. Indeed, during the development of a wide variety of connective tissues, stress fibers increase in prominence during periods of cellular elongation, permitting an oriented deposition of ECM proteins that establishes a scaffold for the architecture of the mature tissue [148]. Moreover, in certain tumors, ECM rigidity directly regulates integrin clustering, Rho activity, focal adhesion morphology, stress fiber formation, and ultimately malignant transformation; this provides a subcellular explanation for the clinical correlation between high gross tumor stiffness and poor prognosis [114].

Taken together, these data confirm that isometric tension in the cytoskeleton governs cell shape stability, and that this cellular force balance results from both active actomyosin-based tension generation and passive contributions from the cells ECM adhesions, as predicted by the tensegrity model of cell mechanics [75]. Individual stress fibers located primarily at the cell base therefore stabilize the shape of the whole cell by generating contractile forces and exerting them on their ECM adhesions, and by balancing forces throughout the

cell and ECM so as to prestress the entire interconnected cytoskeleton. The use of the femtosecond laser nanosurgery together with traction force microscopy and photobleaching methods to probe the local viscoelastic properties of the cytoskeletal fibers offers a new tool for spatially-resolved mechanical mapping in living cells.

Chapter 8

Conclusion and Outlook

This dissertation offers a deeper understanding in the application of femtosecond laser pulses for subcellular nanosurgery. The number of commercially available, turn key femtosecond laser systems is growing and so is the number of research groups with access to these systems. In order to utilize the full potential that femtosecond lasers have to offer, we need a detailed understanding of the interaction mechanism of short laser pulses with biological materials. Here, we have unveiled some of the important differences in the laser parameters and their effect on subcellular disruption and raised new questions about the nonlinear interaction mechanism. In this final chapter, we summarize the key results of this thesis and offer some ideas for future investigation.

To carry out our experiments, we built a custom fluorescence microscope system which has an important advantage over standard commercial microscopes: it is easy to integrate a femtosecond laser beam in it. This allows us to disrupt and image a sample simultaneously. We also built a multiphoton microscope which has the same simultaneous imaging the disruption capability. The advantages of the multiphoton system is that it has deeper penetration depth, higher resolution (especially in the z -direction), and reduced

overall sample photobleaching. The limitation of our current system is in the number of fluorescent dyes that we can two-photon excite with the stationary wavelength of the laser. Newer, tunable lasers have since become available, which can overcome this limitation. Both of these home-built microscope systems are used for femtosecond laser subcellular disruption.

We found definitive proof of bulk ablation within single cells, by studying the femtosecond laser irradiated area under a transmission electron microscope. Because the interaction is highly nonlinear, it can be localized to an area smaller than the diffraction limited focal spot. At energies near threshold we determined that the disrupted area is as small as 250 nm in diameter. We also established that there is a small energy range, near threshold, where it is possible to induce bleaching of fluorescent dyes without material disruption. This is an important result, as one looks only at a fluorescence marker to determine material disruption. The 20% difference in photobleaching and disruption threshold for kHz laser repetition rate should help circumvent this issue.

We studied the effect of the laser repetition rate on the threshold and extent of subcellular disruption. Most initial research on subcellular disruption is done with kHz systems. MHz repetition rate lasers, however, are becoming prevalent in biology, as they are cheaper, easy to use, and readily available with a commercial multiphoton microscope. It is not possible to carry over the pulse energy threshold established for kHz pulse trains to MHz systems. The energy accumulation in the focal volume has to be accounted for and the threshold for disruption depends critically both on pulse energy and exposure duration. At low energies and short irradiation duration there is no disruption and at higher energies and longer irradiation there can be significant damage to the cell.

We used femtosecond laser nanosurgery to probe tension in actin stress fibers in living endothelial cells. By severing an individual stress fiber and visualizing its retraction

we showed that actin carries prestress in adherent, non-contractile cells. We confirmed that the retraction is due to mechanical tension and not fiber disassembly and depolymerization. By plating the cells on softer, more compliant substrates we measured the deflection of the substrate and extrapolated the force contribution of a stress filament on total amount of force exerted by the cell. We found this contribution to be surprisingly large.

Determining directly the exact elastic properties of the stress fiber and the amount of tension it bears is a hard task due to the many unknowns about the local environment. The stress fiber is a composite structure, many of individual actin protein strands bundled together through the binding of molecular motors. These fibers exist in a dense interconnected network which is intertwined with the rest of the cytoskeleton. Through some more experiments it might be possible to get more detailed information about the mechanical structure of the cell and the actin tension. We can also examine the actin tension in different cell types, for example some cancer cells have been known to overexpress actin.

One of the challenges in directly comparing the data from actin filaments in different cells, is that the cells have different number of stress fibers in a different geometrical distribution. It is possible to constrain cell shape to a fixed geometry, such as a square. Then the actin filaments have set lengths and quite uniform distribution. By varying the size of the cells and thus the length and thickness of the filament we should be able to see what the dependence of retraction is on these parameters.

In the tensegrity model of cell mechanics, the actin stress fibers and the microtubules have the opposing roles of tension and compression. While it is not possible to visualize local compression of microtubules, due to their fast polymerization, we might be able to see the link between these two networks. We can visualize both actin and microtubules by appropriately transfecting the cell. Then we can disrupt a single actin filament and measure both its retraction and the deformation in the local microtubule network that

it induced. Varying the tension in the actin by introducing drugs or altering the substrate stiffness, should produce a respective difference in the microtubule deflection.

Lastly, the ultimate goal would be to study cell mechanics in a more natural, three-dimensional environment. To this end, we suggest that cells are transfected with fluorescent labels and cultivated in a collagen gel. The stiffness of the collagen matrix is much closer to an *in vivo* situation than a glass slide. We can then measure the strength of the mechanical connection between the actin network and the collagen gel. We can both disrupt stress fibers and visualize resulting deformation of the collagen gel or disrupt the collagen and look for rearrangement in the actin. To this end, multiphoton microscopy will be necessary, as we can image the collagen through second-harmonic generation and the actin through two-photon imaging.

This is just a sample of the future research in cell mechanics possible through femtosecond laser nanosurgery. There are many more problems in cell biology which would benefit from the spatial specificity of this technique. Some of the possible upgrades that would increase the versatility of our system include the upgrade and expansion of the imaging portion of the system. It would be useful to be able to do two color imaging (for example YFP fluorescence and collagen second-harmonic) simultaneously. Rather than translating the sample to overlap the laser focus with a specific structure, it is possible to integrate scanning mirrors and move the laser beam to the desired area of the sample. This would also increase the processing speed and make multi target disruption possible.

On the physics side, more studies need to be done with high repetition rate lasers. Understanding the transition from chemical bond-breaking to heating and vaporization to plasma-induced ablation may prove to be crucial in minimizing cell damage. It may be possible to image the undesirable stress that femtosecond laser nanosurgery inflicts on the cell through changes in the calcium concentration and the reactive oxygen species

generation. Also, certain regimes might be preferable to other for different application. For example, permeability of the cell membrane has been shown for high repetition rates and actin ablation for both high and low repetition rates. The optimal conditions for these different applications might indeed be in the different regimes.

The study of the interaction of femtosecond laser pulses with biological material with undoubtedly continue in the future. Some basic question about the interaction mechanism are still left unresolved. The growing number of applications femtosecond lasers in biology will drive more research in this area.

References

- [1] K. Koenig, “Multiphoton microscopy in life sciences,” *Journal of Microscopy*, no. 200, pp. 83–104, 2000.
- [2] M. H. Niemz, *Laser-Tissue Interactions: Fundamentals and Applications*. Berlin, Heidelberg, New York: Springer-Verlag, 3rd ed., 1996.
- [3] C. B. Schaffer, A. Brodeur, and E. Mazur, “Laser-induced breakdown and damage in bulk transparent materials induced by tightly focused femtosecond laser pulses,” *Measurement Science and Technology*, vol. 12, no. 11, pp. 1784–1794, 2001.
- [4] E. N. Glezer, M. Milosavljevic, L. Huang, R. J. Finlay, T. H. Her, J. P. Callan, and E. Mazur, “Three-dimensional optical storage inside transparent materials,” *Optics Letters*, vol. 21, no. 24, pp. 2023–2025, 1996.
- [5] C. B. Schaffer, A. Brodeur, J. F. Garcia, and E. Mazur, “Micromachining bulk glass by use of femtosecond laser pulses with nanojoule energy,” *Optics Letters*, vol. 26, no. 2, pp. 93–95, 2001.
- [6] C. B. Schaffer, J. F. Garcia, and E. Mazur, “Bulk heating of transparent materials using a high-repetition-rate femtosecond laser,” *Applied Physics A-Materials Science and Processing*, vol. 76, no. 3, pp. 351–354, 2003.
- [7] W. R. Zipfel, R. M. Williams, and W. W. Webb, “Nonlinear magic: multiphoton microscopy in the biosciences,” *Nature Biotechnology*, vol. 21, no. 11, pp. 1368–1376, 2003.
- [8] W. R. Zipfel, R. M. Williams, R. Christie, A. Y. Nikitin, B. T. Hyman, and W. W. Webb, “Live tissue intrinsic emission microscopy using multiphoton-excited native fluorescence and second harmonic generation,” *Proceedings Of The National Academy Of Sciences Of The United States Of America*, vol. 100, no. 12, pp. 7075–7080, 2003.

- [9] A. Zoumi, A. Yeh, and B. J. Tromberg, "Imaging cells and extracellular matrix in vivo by using second-harmonic generation and two-photon excited fluorescence," *Proceedings Of The National Academy Of Sciences Of The United States Of America*, vol. 99, no. 17, pp. 11014–11019, 2002.
- [10] K. Koenig, I. Riemann, P. Fischer, and K. H. Halbhauer, "Intracellular nanosurgery with near infrared femtosecond laser pulses," *Cellular And Molecular Biology*, vol. 45, no. 2, pp. 195–201, 1999.
- [11] U. K. Tirlapur and K. Konig, "Cell biology - targeted transfection by femtosecond laser," *Nature*, vol. 418, no. 6895, pp. 290–291, 2002.
- [12] N. Shen, D. Datta, C. B. Schaffer, P. LeDuc, D. E. Ingber, and E. Mazur, "Ablation of cytoskeletal filaments and mitochondria in cells using a femtosecond laser nanoscissor," *Mechanics and Chemistry of Biosystems*, vol. 2, pp. 17–26, 2005.
- [13] S. H. Chung, D. A. Clark, C. V. Gabel, E. Mazur, and A. D. T. Samuel, "The role of the *afd* neuron in *c-elegans* thermotaxis analyzed using femtosecond laser ablation," *Bmc Neuroscience*, vol. 7, 2006. 30.
- [14] M. F. Yanik, H. Cinar, H. N. Cinar, A. D. Chisholm, Y. S. Jin, and A. Ben-Yakar, "Neurosurgery - functional regeneration after laser axotomy," *Nature*, vol. 432, no. 7019, pp. 822–822, 2004.
- [15] P. S. Tsai, B. Friedman, A. I. Ifarraguerri, B. D. Thompson, V. Lev-Ram, C. B. Schaffer, C. Xiong, R. Y. Tsien, J. A. Squier, and D. Kleinfeld, "All-optical histology using ultrashort laser pulses," *Neuron*, vol. 39, no. 1, pp. 27–41, 2003.
- [16] N. Nishimura, C. B. Schaffer, B. Friedman, P. S. Tsai, P. D. Lyden, and D. Kleinfeld, "Targeted insult to subsurface cortical blood vessels using ultrashort laser pulses: three models of stroke," *Nature Methods*, vol. 3, no. 2, pp. 99–108, 2006.
- [17] A. Heisterkamp, T. Ripken, T. Mamom, W. Drommer, H. Welling, W. Ertmer, and H. Lubatschowski, "Nonlinear side effects of fs pulses inside corneal tissue during photodisruption," *Applied Physics B-Lasers And Optics*, vol. 74, no. 4-5, pp. 419–425, 2002.
- [18] K. Snelson, "Double six," 1967.
- [19] S. Kumar, I. Z. Maxwell, A. Heisterkamp, T. R. Polte, T. P. Lele, M. Salanga, E. Mazur, and D. E. Ingber, "Viscoelastic retraction of single living stress fibers and its impact on cell shape, cytoskeletal organization, and extracellular

- matrix mechanics,” *Biophysical Journal*, vol. 90, no. 10, pp. 3762–3773, 2006.
- [20] R. Graaff, A. C. M. Dassel, M. H. Koelink, F. F. M. Demul, J. G. Aarnoudse, and W. G. Zijlstra, “Optical-properties of human dermis invitro and invivo,” *Applied Optics*, vol. 32, no. 4, pp. 435–447, 1993.
- [21] R. F. Lyons, R. P. Abergel, R. A. White, R. M. Dwyer, J. C. Castel, and J. Uitto, “Biostimulation of wound-healing invivo by a helium-neon laser,” *Annals Of Plastic Surgery*, vol. 18, no. 1, pp. 47–50, 1987.
- [22] R. W. Boyd, *Nonlinear Optics*. Academic Press, 2nd ed., 2003.
- [23] Bloembergen, N., “Laser-induced electric breakdown in solids,” *Ieee Journal Of Quantum Electronics*, vol. QE10, no. 3, pp. 375–386, 1974.
- [24] E. N. Glezer and E. Mazur, “Ultrafast-laser driven micro-explosions in transparent materials,” *Applied Physics Letters*, vol. 71, no. 7, pp. 882–884, 1997.
- [25] W. Watanabe, T. Toma, K. Yamada, J. Nishii, K. Hayashi, and K. Itoh, “Optical seizing and merging of voids in silica glass with infrared femtosecond laser pulses,” *Optics Letters*, vol. 25, no. 22, pp. 1669–1671, 2000.
- [26] A. Vogel, J. Noack, G. Huttman, and G. Paltauf, “Mechanisms of femtosecond laser nanosurgery of cells and tissues,” *Applied Physics B-Lasers And Optics*, vol. 81, no. 8, pp. 1015–1047, 2005.
- [27] J. G. Fujimoto, W. Z. Lin, E. P. Ippen, C. A. Puliafito, and R. F. Steinert, “Time-resolved studies of nd-yag laser-induced breakdown - plasma formation, acoustic-wave generation, and cavitation,” *Investigative Ophthalmology and Visual Science*, vol. 26, no. 12, pp. 1771–1777, 1985.
- [28] E. N. Glezer, C. B. Schaffer, N. Nishimura, and E. Mazur, “Minimally disruptive laser-induced breakdown in water,” *Optics Letters*, vol. 22, no. 23, pp. 1817–1819, 1997.
- [29] R. R. Gattass, L. R. Cerami, and E. Mazur, “Micromachining of bulk glass with bursts of femtosecond laser pulses at variable repetition rates,” *Optics Express*, vol. 14, no. 12, pp. 5279–5284, 2006.
- [30] S. M. Eaton, H. B. Zhang, and P. R. Herman, “Heat accumulation effects in femtosecond laser-written waveguides with variable repetition rate,” *Optics Express*, vol. 13, no. 12, pp. 4708–4716, 2005.
- [31] L. Shah, A. Arai, S. Eaton, and P. Herman, “Waveguide writing in fused silica

- with a femtosecond fiber laser at 522 nm and 1 mhz repetition rate,” *Optics Express*, vol. 13, no. 6, pp. 1999–2006, 2005.
- [32] W. Denk, J. H. Strickler, and W. W. Webb, “2-photon laser scanning fluorescence microscopy,” *Science*, vol. 248, no. 4951, pp. 73–76, 1990.
- [33] I. Freund and M. Deutsch, “2nd-harmonic microscopy of biological tissue,” *Optics Letters*, vol. 11, no. 2, pp. 94–96, 1986.
- [34] M. Goppert-Mayer, “Elementary file with two quantum fissures,” *Annalen Der Physik*, vol. 9, no. 3, pp. 273–294, 1931.
- [35] C. Xu and W. W. Webb, “Measurement of two-photon excitation cross sections of molecular fluorophores with data from 690 to 1050 nm,” *Journal Of The Optical Society Of America B-Optical Physics*, vol. 13, no. 3, pp. 481–491, 1996.
- [36] C. Xu, W. Zipfel, and W. W. Webb, “Three-photon excited fluorescence and applications in nonlinear laser scanning microscopy,” *Biophysical Journal*, vol. 70, no. 2, pp. WP297–WP297, 1996. Part 2.
- [37] G. A. Blab, P. H. M. Lommerse, L. Cognet, G. S. Harms, and T. Schmidt, “Two-photon excitation action cross-sections of the autofluorescent proteins,” *Chemical Physics Letters*, vol. 350, no. 1-2, pp. 71–77, 2001.
- [38] F. Bestvater, E. Spiess, G. Stobrawa, M. Hacker, T. Feurer, T. Porwol, U. Berchner-Pfannschmidt, C. Wotzlaw, and H. Acker, “Two-photon fluorescence absorption and emission spectra of dyes relevant for cell imaging,” *Journal Of Microscopy-Oxford*, vol. 208, pp. 108–115, 2002. Part 2.
- [39] Y. Barad, H. Eisenberg, M. Horowitz, and Y. Silberberg, “Nonlinear scanning laser microscopy by third harmonic generation,” *Applied Physics Letters*, vol. 70, no. 8, pp. 922–924, 1997.
- [40] D. Debarre, W. Supatto, A. M. Pena, A. Fabre, T. Tordjmann, L. Combettes, M. C. Schanne-Klein, and E. Beaurepaire, “Imaging lipid bodies in cells and tissues using third-harmonic generation microscopy,” *Nature Methods*, vol. 3, no. 1, pp. 47–53, 2006.
- [41] W. Supatto, D. Debarre, B. Moulia, E. Brouzes, J. L. Martin, E. Farge, and E. Beaurepaire, “In vivo modulation of morphogenetic movements in drosophila embryos with femtosecond laser pulses,” *Proceedings Of The National Academy Of Sciences Of The United States Of America*, vol. 102, no. 4, pp. 1047–1052, 2005.

- [42] R. Richards-Kortum and E. Sevick-Muraca, "Quantitative optical spectroscopy for tissue diagnosis," *Annual Review Of Physical Chemistry*, vol. 47, pp. 555–606, 1996.
- [43] G. H. Patterson and D. W. Piston, "Photobleaching in two-photon excitation microscopy," *Biophysical Journal*, vol. 78, no. 4, pp. 2159–2162, 2000.
- [44] H. Kawano, Y. Nabekawa, A. Suda, Y. Oishi, H. Mizuno, A. Miyawaki, and K. Midorikawa, "Attenuation of photobleaching in two-photon excitation fluorescence from green fluorescent protein with shaped excitation pulses," *Biochemical And Biophysical Research Communications*, vol. 311, no. 3, pp. 592–596, 2003.
- [45] J. M. Squirrell, D. L. Wokosin, J. G. White, and B. D. Bavister, "Long-term two-photon fluorescence imaging of mammalian embryos without compromising viability," *Nature Biotechnology*, vol. 17, no. 8, pp. 763–767, 1999.
- [46] U. K. Tirlapur, K. Konig, C. Peuckert, R. Krieg, and K. J. Halhuber, "Femtosecond near-infrared laser pulses elicit generation of reactive oxygen species in mammalian cells leading to apoptosis-like death," *Experimental Cell Research*, vol. 263, no. 1, pp. 88–97, 2001.
- [47] A. Hopt and E. Neher, "Highly nonlinear photodamage in two-photon fluorescence microscopy," *Biophysical Journal*, vol. 80, no. 4, pp. 2029–2036, 2001.
- [48] H. J. Koester, D. Baur, R. Uhl, and S. W. Hell, "Ca²⁺ fluorescence imaging with pico- and femtosecond two-photon excitation: Signal and photodamage," *Biophysical Journal*, vol. 77, no. 4, pp. 2226–2236, 1999.
- [49] W. Watanabe and N. Arakawa, "Femtosecond laser disruption of subcellular organelles in a living cell," *Optics Express*, vol. 12, no. 18, pp. 4203–4213, 2004.
- [50] B. J., A. Heisterkamp, N. A., E. W., and H. Lubatschowski, "Combined multiphoton imaging and cell surgery by femtosecond laser pulse," in *Deutschen Gesellschaft fr angewandte Optik Conference*, vol. 1614-8436, 2006.
- [51] M. W. Berns, J. Aist, J. Edwards, K. Strahs, J. Girton, P. McNeill, J. B. Ratner, M. Kitzes, M. Hammerwilson, L. H. Liaw, A. Siemens, M. Koonce, S. Peterson, S. Brenner, J. Burt, R. Walter, P. J. Bryant, D. Vandyk, J. Coulombe, T. Cahill, and G. S. Berns, "Laser micro-surgery in cell and developmental biology," *Science*, vol. 213, no. 4507, pp. 505–513, 1981.
- [52] M. P. Koonce, K. R. Strahs, and M. W. Berns, "Repair of laser-severed stress

- fibers in myocardial non-muscle cells,” *Experimental Cell Research*, vol. 141, no. 2, pp. 375–384, 1982. EXP CELL RES.
- [53] K. R. Strahs and M. W. Berns, “Laser microirradiation of stress fibers and intermediate filaments in non-muscle cells from cultured rat-heart,” *Experimental Cell Research*, vol. 119, no. 1, pp. 31–45, 1979. EXP CELL RES.
- [54] T. Brabec and F. Krausz, “Intense few-cycle laser fields: Frontiers of nonlinear optics,” *Reviews Of Modern Physics*, vol. 72, no. 2, pp. 545–591, 2000.
- [55] O. E. Martinez, “Design of high-power ultrashort pulse-amplifiers by expansion and recompression,” *Ieee Journal Of Quantum Electronics*, vol. 23, no. 8, pp. 1385–1387, 1987.
- [56] R. L. Fork, O. E. Martinez, and J. P. Gordon, “Negative dispersion using pairs of prisms,” *Optics Letters*, vol. 9, no. 5, pp. 150–152, 1984.
- [57] O. E. Martinez, J. P. Gordon, and R. L. Fork, “Negative group-velocity dispersion using refraction,” *Journal Of The Optical Society Of America A-Optics Image Science And Vision*, vol. 1, no. 10, pp. 1003–1006, 1984.
- [58] P. S. Tsai, N. Nishimura, E. J. Yoder, A. White, E. Dolnick, and D. Kleinfeld, “Principles, design and construction of a two photon scanning microscope for in vitro and in vivo studies,” in *In Methods for In Vivo Optical Imaging* (F. R., ed.), pp. 113–171, CRC Press, 2002.
- [59] C. S. Chen, M. Mrksich, S. Huang, G. M. Whitesides, and D. E. Ingber, “Geometric control of cell life and death,” *Science*, vol. 276, no. 5317, pp. 1425–1428, 1997.
- [60] Y. Numaguchi, S. Huang, T. R. Polte, G. S. Eichler, N. Wang, and D. E. Ingber, “Caldesmon-dependent switching between capillary endothelial cell growth and apoptosis through modulation of cell shape and contractility,” *Angiogenesis*, vol. 6, no. 1, pp. 55–64, 2003.
- [61] S. H. Hu, J. X. Chen, and N. Wang, “Cell spreading controls balance of prestress by microtubules and extracellular matrix,” *Frontiers In Bioscience*, vol. 9, pp. 2177–2182, 2004. Suppl. S.
- [62] F. J. Alenghat, S. M. Nauli, R. Kolb, J. Zhou, and D. E. Ingber, “Global cytoskeletal control of mechanotransduction in kidney epithelial cells,” *Experimental Cell Research*, vol. 301, no. 1, pp. 23–30, 2004.
- [63] J. Noack, D. X. Hammer, G. D. Noojin, B. A. Rockwell, and A. Vogel, “Influ-

- ence of pulse duration on mechanical effects after laser-induced breakdown in water,” *Journal Of Applied Physics*, vol. 83, no. 12, pp. 7488–7495, 1998.
- [64] V. Venugopalan, A. Guerra, K. Nahen, and A. Vogel, “Role of laser-induced plasma formation in pulsed cellular microsurgery and micromanipulation,” *Physical Review Letters*, vol. 88, no. 7, 2002. 078103.
- [65] D. Gusnard and R. H. Kirschner, “Cell and organelle shrinkage during preparation for scanning electron-microscopy - effects of fixation, dehydration and critical-point drying,” *Journal Of Microscopy-Oxford*, vol. 110, no. MAY, pp. 51–57, 1977.
- [66] U. Brunk, V. P. Collins, and E. Arro, “The fixation, dehydration, drying and coating of cultured-cells for sem,” *Journal Of Microscopy-Oxford*, vol. 123, no. AUG, pp. 121–131, 1981.
- [67] S. S. Mao, F. Quere, S. Guizard, X. Mao, R. E. Russo, G. Petite, and P. Martin, “Dynamics of femtosecond laser interactions with dielectrics,” *Applied Physics A-Materials Science and Processing*, vol. 79, no. 7, pp. 1695–1709, 2004.
- [68] K. K. Parker, A. L. Brock, C. Brangwynne, R. J. Mannix, N. Wang, E. Ostuni, N. A. Geisse, J. C. Adams, G. M. Whitesides, and D. E. Ingber, “Directional control of lamellipodia extension by constraining cell shape and orienting cell tractional forces,” *Faseb Journal*, vol. 16, no. 10, 2002.
- [69] R. Singhvi, A. Kumar, G. P. Lopez, G. N. Stephanopoulos, D. I. C. Wang, G. M. Whitesides, and D. E. Ingber, “Engineering cell-shape and function,” *Science*, vol. 264, no. 5159, pp. 696–698, 1994.
- [70] T. J. Dennerll, H. C. Joshi, V. L. Steel, R. E. Buxbaum, and S. R. Heidemann, “Tension and compression in the cytoskeleton of pc-12 neurites ii - quantitative measurements,” *Journal Of Cell Biology*, vol. 107, no. 2, pp. 665–674, 1988.
- [71] S. R. Heidemann and R. E. Buxbaum, “Tension as a regulator and integrator of axonal growth,” *Cell Motility And The Cytoskeleton*, vol. 17, no. 1, pp. 6–10, 1990.
- [72] S. R. Heidemann, S. Kaech, R. E. Buxbaum, and A. Matus, “Direct observations of the mechanical behaviors of the cytoskeleton in living fibroblasts,” *Journal Of Cell Biology*, vol. 145, no. 1, pp. 109–122, 1999.
- [73] A. J. Ridley, M. A. Schwartz, K. Burridge, R. A. Firtel, M. H. Ginsberg, G. Borisy, J. T. Parsons, and A. R. Horwitz, “Cell migration: Integrating signals from front to back,” *Science*, vol. 302, no. 5651, pp. 1704–1709, 2003.

- [74] J. H. Hoh and C. A. Schoenenberger, "Surface-morphology and mechanical-properties of mdck monolayers by atomic-force microscopy," *Journal Of Cell Science*, vol. 107, pp. 1105–1114, 1994. Part 5.
- [75] D. E. Ingber, "Tensegrity i. cell structure and hierarchical systems biology," *Journal Of Cell Science*, vol. 116, no. 7, pp. 1157–1173, 2003.
- [76] B. Fuller, "Tensegrity," *Portfolio Artnews Annual*, no. 4, pp. 112–127, 1961.
- [77] S. R. Heidemann and D. Wirtz, "Towards a regional approach to cell mechanics," *Trends In Cell Biology*, vol. 14, no. 4, pp. 160–166, 2004.
- [78] S. R. Heidemann, P. Lamoureaux, and R. E. Buxbaum, "Opposing views on tensegrity as a structural framework for understanding cell mechanics," *Journal Of Applied Physiology*, vol. 89, no. 4, pp. 1670–1674, 2000.
- [79] D. E. Ingber, S. R. Heidemann, P. Lamoureaux, and R. E. Buxbaum, "Opposing views on tensegrity as a structural framework for understanding cell mechanics," *Journal Of Applied Physiology*, vol. 89, no. 4, pp. 1663–1670, 2000.
- [80] K. D. Costa, W. J. Hucker, and F. C. P. Yin, "Buckling of actin stress fibers: A new wrinkle in the cytoskeletal tapestry," *Cell Motility And The Cytoskeleton*, vol. 52, no. 4, pp. 266–274, 2002. CELL MOTILITY CYTOSKEL.
- [81] M. S. Kolodney and R. B. Wysolmerski, "Isometric contraction by fibroblasts and endothelial-cells in tissue-culture - a quantitative study," *Journal Of Cell Biology*, vol. 117, no. 1, pp. 73–82, 1992. J CELL BIOL.
- [82] D. Riveline, E. Zamir, N. Q. Balaban, U. S. Schwarz, T. Ishizaki, S. Narumiya, Z. Kam, B. Geiger, and A. D. Bershadsky, "Focal contacts as mechanosensors: Externally applied local mechanical force induces growth of focal contacts by an mdia1-dependent and rock-independent mechanism," *Journal Of Cell Biology*, vol. 153, no. 6, pp. 1175–1185, 2001. J CELL BIOL.
- [83] K. Katoh, Y. Kano, M. Masuda, H. Onishi, and K. Fujiwara, "Isolation and contraction of the stress fiber," *Molecular Biology of the Cell*, vol. 9, no. 7, pp. 1919–1938, 1998. MOL BIOL CELL.
- [84] S. Deguchi, T. Ohashi, and M. Sato, "Tensile properties of single stress fibers isolated from vascular smooth muscle cells," *Journal of Biomechanics*, vol. In press, 2005.
- [85] S. Anderson, L. DiCesare, I. Tan, T. Leung, and N. SundarRaj, "Rho-mediated

- assembly of stress fibers is differentially regulated in corneal fibroblasts and myofibroblasts,” *Experimental Cell Research*, vol. 298, no. 2, pp. 574–583, 2004. EXP CELL RES.
- [86] B. H. Chen, J. T. C. Tzen, A. R. Bresnick, and H. C. Chen, “Roles of rho-associated kinase and myosin light chain kinase in morphological and migratory defects of focal adhesion kinase-null cells,” *Journal of Biological Chemistry*, vol. 277, no. 37, pp. 33857–33863, 2002. J BIOL CHEM.
- [87] K. Katoh, Y. Kano, M. Amano, K. Kaibuchi, and K. Fujiwara, “Stress fiber organization regulated by mlck and rho-kinase in cultured human fibroblasts,” *American Journal of Physiology-Cell Physiology*, vol. 280, no. 6, pp. C1669–C1679, 2001. AMER J PHYSIOL-CELL PHYSIOL.
- [88] J. Sinnett-Smith, J. A. Lunn, D. Leopoldt, and E. Rozengurt, “Y-27632, an inhibitor of rho-associated kinases, prevents tyrosine phosphorylation of focal adhesion kinase and paxillin induced by bombesin: Dissociation from tyrosine phosphorylation of p130(cas),” *Experimental Cell Research*, vol. 266, no. 2, pp. 292–302, 2001.
- [89] T. Yeung, P. C. Georges, L. A. Flanagan, B. Marg, M. Ortiz, M. Funaki, N. Zahir, W. Y. Ming, V. Weaver, and P. A. Janmey, “Effects of substrate stiffness on cell morphology, cytoskeletal structure, and adhesion,” *Cell Motility And The Cytoskeleton*, vol. 60, no. 1, pp. 24–34, 2005.
- [90] W. E. Gordon, “Immunofluorescent and ultrastructural studies of sarcomeric units in stress fibers of cultured non-muscle cells,” *Experimental Cell Research*, vol. 117, no. 2, pp. 253–260, 1978. EXP CELL RES.
- [91] J. W. Sanger, B. Mittal, and J. M. Sanger, “Analysis of myofibrillar structure and assembly using fluorescently labeled contractile proteins,” *Journal Of Cell Biology*, vol. 98, no. 3, pp. 825–833, 1984. J CELL BIOL.
- [92] S. L. Gupton, K. L. Anderson, T. P. Kole, R. S. Fischer, A. Ponti, S. E. Hitchcock-DeGregori, G. Danuser, V. M. Fowler, D. Wirtz, D. Hanein, and C. M. Waterman-Storer, “Cell migration without a lamellipodium: translation of actin dynamics into cell movement mediated by tropomyosin,” *Journal Of Cell Biology*, vol. 168, no. 4, pp. 619–631, 2005.
- [93] T. P. Stossel, “From signal to pseudopod - how cells control cytoplasmic actin assembly,” *Journal of Biological Chemistry*, vol. 264, no. 31, pp. 18261–18264, 1989.
- [94] J. A. Theriot and T. J. Mitchison, “Actin microfilament dynamics in locomot-

- ing cells,” *Nature*, vol. 352, no. 6331, pp. 126–131, 1991.
- [95] J. Kolega, J. W. Janson, and D. L. Taylor, “The role of solation-contraction coupling in regulating stress fiber dynamics in nonmuscle cells,” *Journal Of Cell Biology*, vol. 114, no. 5, pp. 993–1003, 1991.
- [96] R. Strohmeier and J. Bereiter-Hahn, “Control of cell-shape and locomotion by external calcium,” *Experimental Cell Research*, vol. 154, no. 2, pp. 412–420, 1984.
- [97] Y. Tseng, K. M. An, and D. Wirtz, “Microheterogeneity controls the rate of gelation of actin filament networks,” *Journal of Biological Chemistry*, vol. 277, no. 20, pp. 18143–18150, 2002.
- [98] J. Bereiter-Hahn, M. Luck, T. Miebach, H. Stelzer, and M. Voth, “Spreading of trypsinized cells - cytoskeletal dynamics and energy requirements,” *Journal Of Cell Science*, vol. 96, pp. 171–188, 1990.
- [99] D. J. Mooney, R. Langer, and D. E. Ingber, “Cytoskeletal filament assembly and the control of cell spreading and function by extracellular-matrix,” *Journal Of Cell Science*, vol. 108, pp. 2311–2320, 1995. Part 6.
- [100] A. Heisterkamp, I. Z. Maxwell, E. Mazur, J. M. Underwood, J. A. Nickerson, S. Kumar, and D. E. Ingber, “Pulse energy dependence of subcellular dissection by femtosecond laser pulses,” *Optics Express*, vol. 13, no. 10, pp. 3690–3696, 2005.
- [101] S. Hu, J. Chen, B. Fabry, Y. Numaguchi, A. Gouldstone, D. E. Ingber, J. J. Fredberg, J. P. Butler, and N. Wang, “Intracellular stress tomography reveals stress focusing and structural anisotropy in cytoskeleton of living cells,” *American Journal of Physiology-Cell Physiology*, vol. 285, no. 5, pp. 1082–1090, 2003.
- [102] T. R. Polte, G. S. Eichler, N. Wang, and D. E. Ingber, “Extracellular matrix controls myosin light chain phosphorylation and cell contractility through modulation of cell shape and cytoskeletal prestress,” *American Journal of Physiology-Cell Physiology*, vol. 286, no. 3, pp. C518–C528, 2004. AMER J PHYSIOL-CELL PHYSIOL.
- [103] J. P. Butler, I. M. Tolic-Norrelykke, B. Fabry, and J. J. Fredberg, “Traction fields, moments, and strain energy that cells exert on their surroundings,” *American Journal of Physiology-Cell Physiology*, vol. 282, no. 3, pp. C595–C605, 2002.

- [104] L. D. Landau and E. M. Lifshitz, *Theory of Elasticity*. Oxford: Pergammon, 3rd ed., 1986.
- [105] T. A. Osswald and G. Menges, *Materials science of polymers for engineers*. Munich: Hanser/Gardner, 1995.
- [106] P. Canadas, V. M. Laurent, C. Oddou, D. Isabey, and S. Wendling, "A cellular tensegrity model to analyse the structural viscoelasticity of the cytoskeleton," *Journal of Theoretical Biology*, vol. 218, no. 2, pp. 155–173, 2002. J THEOR BIOL.
- [107] S. Clement, H. B., V. Dugina, G. Gabbiani, and C. Chaponnier, "The n-terminal ac-eeed sequence plays a role in alpha-smooth-muscle actin incorporation into stress fibers," *Journal Of Cell Science*, vol. 118, no. 7, pp. 1395–1404, 2005.
- [108] S. Narumiya, T. Ishizaki, and M. Uehata, "Use and properties of rock-specific inhibitor y-27632," *Methods in Enzymology*, vol. 325, pp. 273–284, 2000.
- [109] A. Mammoto, S. Huang, K. Moore, P. Oh, and D. E. Ingber, "Role of rhoa, mdia, and rock in cell shape-dependent control of the skp2-p27(kip1) pathway and the g(1)/s transition," *Journal of Biological Chemistry*, vol. 279, no. 25, pp. 26323–26330, 2004. J BIOL CHEM.
- [110] S. R. Peyton and A. J. Putnam, "Extracellular matrix rigidity governs smooth muscle cell rigidity in a biphasic fashion," *Journal of Celullar Physiology*, vol. 204, no. 1, pp. 198–209, 2005. J CELL PHYSIOL.
- [111] Y. T. Shiu, S. Li, W. A. Marganski, S. Usami, M. A. Schwartz, Y. L. Wang, M. Dembo, and S. Chien, "Rho mediates the shear-enhancement of endothelial cell migration and traction force generation," *Biophysical Journal*, vol. 86, pp. 2558–2565, 2004.
- [112] J. Chen, B. Fabry, E. L. Schiffrin, and N. Wang, "Twisting integrin receptors increases endothelin-1 gene expression in endothelial cells," *American Journal of Physiology-Cell Physiology*, vol. 280, pp. C1475–C1484, 2001.
- [113] A. Engler, L. Bacakova, C. Newman, A. Hategan, M. Griffin, and D. Discher, "Substrate compliance versus ligand density in cell on gel responses," *Biophysical Journal*, vol. 86, no. 1 Pt 1, pp. 617–628, 2004.
- [114] M. J. Paszek, N. Zahir, K. R. Johnson, J. N. Lakins, G. I. Rozengberg, A. Gefen, C. A. Reinhart-KIng, S. S. Margulies, M. Dembo, D. Boettiger, D. A. Hammer, and V. M. Weaver, "Tensional homeostasis and the malignant

- phenotype,” *Cancer Cell*, vol. 8, pp. 241–254, 2005.
- [115] S. Munevar, Y. L. Wang, and M. Dembo, “Traction force microscopy of migrating normal and h-ras transformed 3t3 fibroblasts,” *Biophysical Journal*, vol. 80, no. 4, pp. 1744–1757, 2001. BIOPHYS J.
- [116] K. A. Beningo, M. Dembo, I. Kaverina, J. V. Small, and Y. L. Wang, “Nascent focal adhesions are responsible for the generation of strong propulsive forces in migrating fibroblasts,” *Journal Of Cell Biology*, vol. 153, no. 4, pp. 881–887, 2001. J CELL BIOL.
- [117] E. L. Botvinick, V. Venugopalan, J. V. Shah, L. H. Liaw, and M. W. Berns, “Controlled ablation of microtubules using a picosecond laser,” *Biophysical Journal*, vol. 87, no. 6, pp. 4203–4212, 2004. BIOPHYS J.
- [118] I. M. Tolic-Norrelykke, L. Sacconi, G. Thon, and F. S. Pavone, “Positioning and elongation of the fission yeast spindle by microtubule-based pushing,” *Current Biology*, vol. 14, no. 13, pp. 1181–1186, 2004.
- [119] A. Khodjakov, S. La Terra, and F. Chang, “Laser microsurgery in fission yeast: Role of the mitotic spindle midzone in anaphase b,” *Current Biology*, vol. 14, no. 15, pp. 1330–1340, 2004. CURR BIOL.
- [120] U. K. Tirlapur and K. Konig, “Femtosecond near-infrared laser pulses as a versatile non-invasive tool for intra-tissue nanoprocessing in plants without compromising viability,” *Plant Journal*, vol. 31, no. 3, pp. 365–374, 2002.
- [121] J. T. Finer, R. M. Simmons, and J. A. Spudich, “Single myosin molecule mechanics - piconewton forces and nanometer steps,” *Nature*, vol. 368, no. 6467, pp. 113–119, 1994. NATURE.
- [122] Y. Ishii, A. Ishijima, and T. Yanagida, “Single molecule nanomanipulation of biomolecules,” *Trends in Biotechnology*, vol. 19, no. 6, pp. 211–216, 2001.
- [123] H. Kojima, A. Ishijima, and T. Yanagida, “Direct measurement of stiffness of single actin-filaments with and without tropomyosin by in-vitro nanomanipulation,” *Proceedings of the National Academy of Sciences of the United States of America*, vol. 91, no. 26, pp. 12962–12966, 1994. PROC NAT ACAD SCI USA.
- [124] X. M. Liu and G. H. Pollack, “Mechanics of f-actin characterized with microfabricated cantilevers,” *Biophysical Journal*, vol. 83, no. 5, pp. 2705–2715, 2002. BIOPHYS J.

- [125] M. L. Gardel, J. H. Shin, F. C. MacKintosh, L. Mahadevan, P. Matsudaira, and D. A. Weitz, "Elastic behavior of cross-linked and bundled actin networks," *Science*, vol. 304, no. 5675, pp. 1301–1305, 2004. SCIENCE.
- [126] W. A. Linke and M. C. Leake, "Multiple sources of passive stress relaxation in muscle fibres," *Physics in Medicine and Biology*, vol. 49, no. 16, pp. 3613–3627, 2004. PHYS MED BIOL.
- [127] C. A. Opitz, M. Kulke, M. C. Leake, C. Neagoe, H. Hinssen, R. J. Hajjar, and W. A. Linke, "Damped elastic recoil of the titin spring in myofibrils of human myocardium," *Proceedings of the National Academy of Sciences of the United States of America*, vol. 100, no. 22, pp. 12688–12693, 2003. PROC NAT ACAD SCI USA.
- [128] P. Cortes, M. Mendez, B. L. Riser, C. J. Guerin, A. Rodriguez-Barbero, C. Hassett, and J. Yee, "F-actin fiber distribution in glomerular cells: Structural and functional implications," *Kidney International*, vol. 58, no. 6, pp. 2452–2461, 2000. KIDNEY INT.
- [129] R. L. Satcher and C. F. Dewey, "Theoretical estimates of mechanical properties of the endothelial cell cytoskeleton," *Biophysical Journal*, vol. 71, no. 1, pp. 109–118, 1996. BIOPHYS J.
- [130] C. M. Lo, H. B. Wang, M. Dembo, and Y. L. Wang, "Cell movement is guided by the rigidity of the substrate," *Biophysical Journal*, vol. 79, no. 1, pp. 144–152, 2000.
- [131] T. P. Lele, J. Pendse, S. Kumar, M. Salanga, J. Karavitis, and D. E. Ingber, "Mechanical forces alter zyxin unbinding kinetics within focal adhesions of living cells," *Journal of Cellular Physiology*, vol. In press, 2005.
- [132] Y. Maeda, K. Hirano, J. Nishimura, T. Sasaki, and H. Kanaide, "Rho-kinase inhibitor inhibits both myosin phosphorylation-dependent and -independent enhancement of myofilament Ca^{2+} sensitivity in the bovine middle cerebral artery," *British Journal of Pharmacology*, vol. 140, pp. 871–880, 2003.
- [133] H. Nobe, K. Nobe, F. Fazal, P. deLanerolle, and R. J. Paul, "Rho kinase mediates serum-induced contraction in fibroblast fibers independent of myosin lc20 phosphorylation," *American Journal of Physiology-Cell Physiology*, vol. 284, no. 3, pp. C599–C606, 2003.
- [134] Y. Kureishi, S. Kobayashi, M. Amano, K. Kimura, H. Kanaide, T. Nakano, K. Kaibuchi, and M. Ito, "Rho-associated kinase directly induces smooth muscle contraction through myosin light chain phosphorylation," *Journal of Bio-*

logical Chemistry, vol. 272, pp. 12257–12260, 1997.

- [135] S. M. Dudek and J. G. Garcia, “Cytoskeletal regulation of pulmonary vascular permeability,” *Journal Of Applied Physiology*, vol. 91, no. 4, pp. 1487–1500, 2001.
- [136] G. Totsukawa, Y. Yamakita, S. Yamashiro, D. J. Hartshorne, Y. Sasaki, and F. Matsumura, “Distinct roles of rock (rho-kinase) and mlck in spatial regulation of mlc phosphorylation for assembly of stress fibers and focal adhesions in 3t3 fibroblasts,” *Journal Of Cell Biology*, vol. 150, no. 4, pp. 797–806, 2000.
- [137] R. Kaunas, P. Nguyen, S. Usami, and S. Chien, “Cooperative effects of rho and mechanical stretch on stress fiber organization,” *Proceedings of the National Academy of Sciences of the United States of America*, vol. 102, no. 44, pp. 15895–15900, 2005.
- [138] L. F. Marek, R. O. Kelley, and B. D. Perdue, “Organization of the cytoskeleton in square fibroblasts,” *Cell Motility And The Cytoskeleton*, vol. 2, no. 2, pp. 115–130, 1982.
- [139] G. J. Seifert, D. Lawson, and G. Wiche, “Immunolocalization of the intermediate filament-associated protein plectin at focal contacts and actin stress fibers,” *European Journal of Cell Biology*, vol. 59, no. 1, pp. 138–147, 1992.
- [140] L. J. Peterson, Z. Rajfur, A. S. Maddox, C. D. Freel, Y. Chen, M. Edlund, C. Otey, and K. Burridge, “Simultaneous stretching and contraction of stress fibers in vivo,” *Molecular Biology of the Cell*, vol. 15, pp. 3497–3508, 2004.
- [141] N. Wang, K. Naruse, D. Stamenovic, J. J. Fredberg, S. M. Mijailovich, I. M. Tolic-Norrelykke, T. Polte, R. Mannix, and D. E. Ingber, “Mechanical behavior in living cells consistent with the tensegrity model,” *Proceedings of the National Academy of Sciences of the United States of America*, vol. 98, no. 14, pp. 7765–7770, 2001.
- [142] A. J. Maniotis, C. S. Chen, and D. E. Ingber, “Demonstration of mechanical connections between integrins cytoskeletal filaments, and nucleoplasm that stabilize nuclear structure,” *Proceedings of the National Academy of Sciences of the United States of America*, vol. 94, no. 3, pp. 849–854, 1997.
- [143] B. P. Helmke, A. B. Rosen, and P. F. Davies, “Mapping mechanical strain of an endogenous cytoskeletal network in living endothelial cells,” *Biophysical Journal*, vol. 84, pp. 2691–2699, 2003.
- [144] N. Wang, I. M. Tolic-Norrelykke, J. X. Chen, S. M. Mijailovich, J. P. But-

- ler, J. J. Fredberg, and D. Stamenovic, "Cell prestress. i. stiffness and prestress are closely associated in adherent contractile cells," *American Journal of Physiology-Cell Physiology*, vol. 282, no. 3, pp. C606–C616, 2002. AMER J PHYSIOL-CELL PHYSIOL.
- [145] D. Choquet, D. P. Felsenfeld, and M. P. Sheetz, "Extracellular matrix rigidity causes strengthening of integrin-cytoskeleton linkages," *Cell*, vol. 88, no. 1, pp. 39–48, 1997.
- [146] R. J. Pelham and Y. L. Wang, "Cell locomotion and focal adhesions are regulated by substrate flexibility," *Proceedings of the National Academy of Sciences of the United States of America*, vol. 94, no. 25, pp. 13661–13665, 1997.
- [147] K. A. Moore, T. Polte, S. Huang, B. Shi, E. Alsberg, M. E. Sunday, and D. E. Ingber, "Control of basement membrane remodeling and epithelial branching morphogenesis in embryonic lung by rho and cytoskeletal tension," *Developmental Dynamics*, vol. 232, no. 2, pp. 268–281, 2005.
- [148] A. Hayes, M. Benjamin, and J. Ralphs, "Role of actin stress fibres in the development of the intervertebral disc: Cytoskeletal control of extracellular matrix assembly," *Developmental Dynamics*, vol. 215, no. 3, pp. 179–189, 1999.